EFFECT OF LOCALIZED STATES ON THE PHOTOCURRENT IN AMORPHOUS SILICON ALLOYS

A THESIS SUBMITTED TO
THE GRADUATE SCHOOL OF NATURAL AND APPLIED SCIENCES
OF
MIDDLE EAST TECHNICAL UNIVERSITY

BY

MEHMET BAHADIR BEBEK

IN PARTIAL FULFILLMENT OF THE REQUIREMENTS
FOR
THE DEGREE OF MASTER OF SCIENCE
IN
PHYSICS

DECEMBER 2009

Approval of the Thesis:

EFFECT OF LOCALIZED STATES ON THE PHOTOCURRENT IN AMORPHOUS SILICON ALLOYS

Submitted by **MEHMET BAHADIR BEBEK** in partial fulfillment of the requirements for the degree of **Master of Science in Physics Department, Middle East Technical University** by,

Prof. Dr. Canan Özgen _____
Dean, Graduate School of **Natural and Applied Sciences**

Prof. Dr. Sinan Bilikmen _____
Head of Department, **Physics**

Assoc. Prof. Dr. İsmail Atılgan _____
Supervisor, **Physics Dept., METU**

Examining Committee Members:

Prof. Dr. Bayram Katırcıoğlu _____
Physics Dept., METU

Assoc. Prof. Dr. İsmail Atılgan _____
Physics Dept., METU

Assoc. Prof. Dr. Akif Esendemir _____
Physics Dept., METU

Assoc. Prof. Dr. Enver Bulur _____
Physics Dept., METU

Assoc. Prof. Dr. Barış Akaoğlu _____
Natural and Applied Sciences, Gazi University

Date: 09.12.2009

I hereby declare that all information in this document has beeen obtained and presented in accordance with acedemic rules and ethical conduct. I also declare that, as required by these rules and conduct, I have fully cited and referenced all material and results that are not original to this work.

Name, Last name : Mehmet Bahadır Bebek

Signature :

ABSTRACT

EFFECT OF LOCALIZED STATES ON THE PHOTOCURRENT IN AMORPHOUS SILICON ALLOYS

Bebek, Mehmet Bahadır
M.S. Department of Physics
Supervisor: Assoc. Prof. Dr. İsmail Atılgan

December 2009, 86 pages

Amorphous Silicon alloy thin films were deposited by plasma enhanced chemical vapor deposition technique. In order to make optoelectronic measurements, diode structures were fabricated by depositing transparent metal electrodes. Theoretical background of localized density of states in the mobility gap and photocurrent mechanisms has been revisited. In light of this, time of flight technique, using transient photocurrent, was utilized to determine mobility in extended states and characteristic energy of tail states in the film. The actual density of states (DOS) in the mobility gap of the deposited films was determined by using absorption coefficients obtained via constant photocurrent measurements. Finally, adverse effects of small Oxygen incorporation on mobility and DOS were observed.

Keywords: a-Si:H thin films, PECVD, TOF, CPM, DOS

ÖZ

AMORF SİLİSYUM ALAŞIMLARINDAKİ YEREL DURUMLARIN FOTO AKIMA ETKİSİ

Bebek, Mehmet Bahadır
Yüksek Lisans, Fizik Bölümü
Tez Yöneticisi: Doç. Dr. İsmail Atılgan

Aralık 2009, 86 sayfa

Amorf silisyum alaşımı ince filimler plazma yardımcılı kimyasal buhar biriktirme yöntemiyle büyütüldü. Optoelektronik ölçümlerin yapılabilmesi için, saydam metal elektrot biriktirilerek diyot yapılar üretildi. Yasak enerji aralığındaki yerel durum yoğunlukları ve fotoakım mekanizmaları inceleyen kuramsal altyapı çalışıldı. Bu bilgiler ışığında, sönümlü fotoakım kullanan uçuş süresi ölçüm tekniği, filmlerdeki bant eteklerinin karakteristik enerjilerinin ve yaygın durumlardaki taşıyıcı hareketliliğinin elde edilmesi için kullanıldı. Filmlerdeki gerçek yerel durum yoğunlukları, sabit foto-akım ölçümü vasıtasıyla elde edilen optik soğurma katsayısı kullanılarak belirlendi. Son olarak, yapıya az miktarda Oksijen atomu karışmasının taşıyıcı hareketliliğine ve yerel durum yoğunluğuna olumsuz etkisi gözlenmiştir.

Anahtar Kelimeler: a-Si:H ince film, PECVD, TOF, CPM, DOS

ACKNOWLEDGEMENTS

I would like to thank to Prof. Dr. Bayram Katırcıoğlu for instructive discussions, suggestions and comments and sharing his knowledge, experience.

I would like to express my thanks to Assoc. Prof. Dr. İsmail Atılgan for his cooperation, support and helpful criticism during whole this work.

I am thankful to Mustafa Anutgan for his help during Uv-Vis Transmission spectroscopy analyses.

I am thankful to my colleagues and the staff in Atılım University Physics Group for their encouragement.

I am also thankful to my family and Gülten Karaoğlan for their support, encouragement and their understanding throughout this work.

TABLE OF CONTENTS

ABSTRACT iv

ÖZ v

ACKNOWLEDGEMENT vi

TABLE OF CONTENTS vii

LIST OF TABLES x

LIST OF FGURES xi

CHAPTERS

1. INTRODUCTION 1

2. ELECTRONIC STRUCTURE OF a-Si:H 3

2.1 Localized Density of States (DOS) Distribution: 3

2.1.1 Tail DOS from Band Edges: 4

2.2 Deep States-Defect Pool Model in a-Si:H Thin Films: 10

2.2.1 Role of Hydrogen in defect creation 11

2.2.2 Analysis of Deep States Distrubutions 13

3. ELECTRONIC TRANSPORT 20

3.1 Introduction 20

3.2 Electronic Conduction Throughout Amorphous Semiconductors: 21

3.2.1 Extended State Conduction: 21

3.2.2 Localized State Conduction by Nearest Neighbor Hopping: 22

3.2.3 Localized State Conduction by Variable Range Hopping: 25

4. TIME OF FLIGHT PRINCIPLES AND TECHNIQUES 26

4.1 General Principles: 26
4.2 The Charge Transport Mechanism: 28
4.3 Transient Trap Limited Transport Theory 32
4.3.1 Mono-energetic Trap Distribution 32
4.3.1.1 Low Fields 35
4.3.1.2 High Fields 36
4.4 Experimental Setup for TOF: 37
5. CONSTANT PHOTOCURRENT METHOD (CPM) 45
5.1 Theory of Carrier Generation 45
5.2 Principles of Constant Photocurrent Method (CPM) 51
5.3 Optoelectronic Measurement System 52
5.4 The Software of CPM 56
6. FABRICATION OF THE SAMPLE AND MEASUREMENTS 59
6.1 Cleaning 59
6.2 Metallization 60
6.3 Deposition of a-Si:H Film 62
6.3.1 Dissociation 62
6.3.2 Adsorbtion 63
6.3.3 Film Growth Process 65
6.4 UV-Vis and Infrared Spectroscopies 67
6.5 The Sample 70
6.6 TOF Measurements 70
6.7 Determination of Absorption Coefficient by CPM Measurements 74

6.8 Determination of N(E) from Absorption Spectra 75

7. CONCLUSION 79

REFERENCES 81

APPENDIX 85

LIST OF TABLES

Tables

6.1 Deposition parameters for a-Si:H and a-SiO_x:H films…….. 67
6.2 Optical Constants, E_G is the Tauc gap, n is the refractive index at 632 nm and L is the thickness, obtained for a-Si:H and a-SiO_x:H films……..... 68
6.3 Transit times and mobility measurements obtained from the TOF experiments for a-Si:H (a) and a-SiO_x:H (b)……. 73
6.4 Parameters obtained by fitting equation 6.10 to α; E_0 is the Urbach energy for valence band tail states……..... 76

LIST OF FIGURES

Figures

2.1 Illustration of the wavefunctions of (a) crystal extended, (b) amorphous extended and (c) amorphous localized states [11]..……. 3
2.2 A simplified model of potential fluctuations due to distorted bond lengths and bond angles..…….. 5
2.3 A typical potential well...…… 5
2.4 A typical DOS distribution in amorphous semiconductors…….. 8
2.5 Bonding orbital diagrams for a-Si:H……..... 9
2.6 Illustration of WB_s conversion to DB_s (change from a bonding state E_{vt} in the valance band tail to non-bonding state E_D around the mid-gap)…..... 11
2.7 Schematic model for the weak bond-dangling bond conversion……. 11
2.8 The eventual hydrogen involved (or mediated) equilibrium or equilibration. Note that in the first picture, two defects are formed, one originated from the isolated (SiH) bond, the second (SiHDSi) originated from the singly hydrogenated (SiSi) bond (i.e., SiH + $(SiSi)_{WB}$ ↔ DB + SiHDSi). However, for the second case, SiSi bonds can have only zero or two H atoms which means that the correlation energy (the extra energy cost of putting a second hydrogen atom in the bond compared to the single hydrogen case) for H occupancy is negative 2SiH + $(SiSi)_{WB}$ ↔ 2(DB) + (SiHHSi)). ……..... 12
2.9 Schematic illustration of H diffusion through the network. Note that the mobile H inserts into a SiSi bond at remote site to give a second DB……. 13
2.10 Density of each charge component within the gap at T=200 °C (a) and 40 °C (b), respectively……... 18
2.11 Density of states splits into +/0 and 0/- distributions for (a) n type a-Si:H ; (b) for intrinsic a-Si:H. and (c) for p type a-Si:H……. 19
4.1 A simplified experimental diagram of TOF technique…… 26
4.2 Modification of the electric field across the sample due to the presence of injected carriers……. 28
4.3 Small signal ac equivalent of TOF experiment setup…….. 29
4.4 (a) I-mode signal. (b) V-mode signal. Solid lines represent trap free media where τ_c is comparable with t_T and the dashed lines represent signals for a sample with single discrete trapping level where $\tau_{c >> } t_T$ 32
4.5 Schematic illustration of TOF experimental set up…….. 38
4.6 The delay times of the input signal from channel “B” of the Tektronix PG-5110 signal generator, the laser optical output and the optosync output of the laser when the trigger input of the VSL-337 air-cooled nitrogen laser is activated……. 39
4.7 Flowchart of the program used for measurement setup……... 41
4.8 Typical voltage transients as measured by the oscilloscope……. 42

4.9 Typical (a) voltage (semi log graph) and (b) current (log-log graph) transients. The current transients in (b) are obtained by division of voltage to corresponding terminator resistance…… 43
4.10 The final form of photocurrent transient…….. 44
5.1 Schematic representations of possible thermal transitions for positively correlated dangling bonds. Dots (•) and open circles (o) represents electrons and holes respectively……... 47
5.2 Schematic representations of possible thermal transitions for positively correlated dangling bonds. Dots (•) and open circles (o) represents electrons and holes respectively……... 48
5.3 Schematic representation of the thermal (U_i) and optical (G_i) transitions between the tail states and the extended bands…… 50
5.4 Optoelectronic measurement system of CPM…….. 54
5.5 Polarization dependence of reflected light……... 55
5.6 Correction curve of beam splitter……. 55
5.7 Flow chart of CPM measurements……... 58
6.1 The schematic view of ITO system…….. 61
6.2 PECVD System…… 66
6.3 Transmission spectra of the films (absorption spectra given in the inset)… 68
6.4 IR spectra of the films. Spectrum of a-Si:H is shifted for clarity……. 69
6.5 Structure of samples made on glass and Si substrates…….. 70
6.6 Typical current transients (a) for stationary (dc) and pulsed (ac) TOF experiments and qualitative electric field distributions in the sample (b)… 71
6.7 Photocurrent transients under 6V ac bias and typical representation of the determination of transit times for a-Si:H (a), a-SiO_x:H (b)…….. 72
6.8 Localized states below conduction band obtained from TOF measurements…… 74
6.9 CPM measurements for a) a-Si:H b) a-SiO_x:H…… 75
6.10 Absorption coefficient obtained from CPM measurements for a-Si:H and a-SiOx:H films; α obtained by transmission (+), by CPM (squares) and by equation (6.10) after fitting (solid line)…… **77**
6.11 Density of states distributions obtained from the CPM measurements for a-Si:H and a-SiOx:H films…… 78
A-1 TOF Measurements under pulsed bias for a-Si:H (a) and a-S$\dot{I}O_x$:H (b) 85
A-2 TOF Measurements under DC bias for a-Si:H (a) and a-S$\dot{I}O_x$:H (b) 86

CHAPTER 1

INTRODUCTION

In today's world, information systems are built by rather two complementary constituents [1]; electronic processors (microelectronics) and input/output devices (large area electronics). Although the first group of devices is continuously developing with unbelievable miniaturization on the crystalline silicon chip, the second class has to stay large as a necessity of man/machine interface such as document scanners, electronic displays, printers etc. The crystalline silicon could not satisfy the requirements of these large area opto-electronic devices due to both its poor optical properties and limited dimensions. The solutions developed on the semiconductors other than the crystalline silicon have created mismatching problems with the existing silicon based microelectronic technologies.

Hydrogenated amorphous silicon (a-Si:H) seems to be a solution to the large area problem of crystalline silicon because it can be deposited at low temperatures (<300°) by the glow discharge method at reasonable cost as large area thin films on low cost substrate (such as glass and ordinary rude organic materials) [2].

Drawbacks of crystalline silicon (c-Si), (namely poor optical properties and limited geometrical area or too high cost of material), are tried to be solved nowadays by a-Si:H films.

Amorphous silicon, whose huge amount, of dangling bond states around midgap energy region (10^{20} $cm^{-1}eV^{-1}$) are reduced to minute amount (10^{15} $cm^{-1}eV^{-1}$) by the hydrogen compensation process, becomes able to be selectively doped both n and p types leading to a large number of practically useful devices such as p-n, p-i-n, Schottky diodes etc. [3].

Besides, the control of the electrical conductivity over 10 orders of magnitude [4] due to its dopability, the field effect allows the sheet conductance of a-Si:H layer to be switched over 6 orders of magnitude [5]. As a result, the

development of thin film transistors for addressing circuits on large area electronics is facilitated by the fact that the gate dielectric layer (mostly a-SiN_x:H film), the channel layer of a-Si:H film and the ohmic source and drain n^+-contact layers can all be deposited in the same plasma reactor (PECVD) [6].

In addition to the above outlined electronic behavior of a-Si:H material, its optical properties are substantially improved compared with the ones of crystalline silicon. Contrary to the optical weakness of crystalline silicon (c-Si), the optical gap of a-Si:H is widened up to the visible region 1.75 eV) leading to the photoconductivity spectrum, shifted to shorter light wavelength compared with crystalline silicon. In other words, the a-Si:H spectrum coincides better with the sensitivity range of human eye (the alloying ability of a-Si:H with Ge, Sn, C, N and O creates a flexibility of adjusting the optical gap from IR to UV). Moreover, the optical absorption of a-Si:H in the visible range is greater by about a factor of 20 than in the case of crystalline silicon [7, 8]. (This increase in optical absorption is a consequence of the irrelevance of the selection rules for optical transitions in amorphous semiconductors (non-conservation of the quasimomentum-k)) [9]. Thus, a thin film of only 1μm thickness absorbs most of the visible light, facilitating the fabrication of high efficiency photosensors.

Consequently amorphous silicon and its alloys are building stones of today's large area optoelectronics in relevant market [1, 10].

CHAPTER 2

ELECTRONIC STRUCTURE OF a-Si:H

2.1 Localized Density of States (DOS) Distribution:

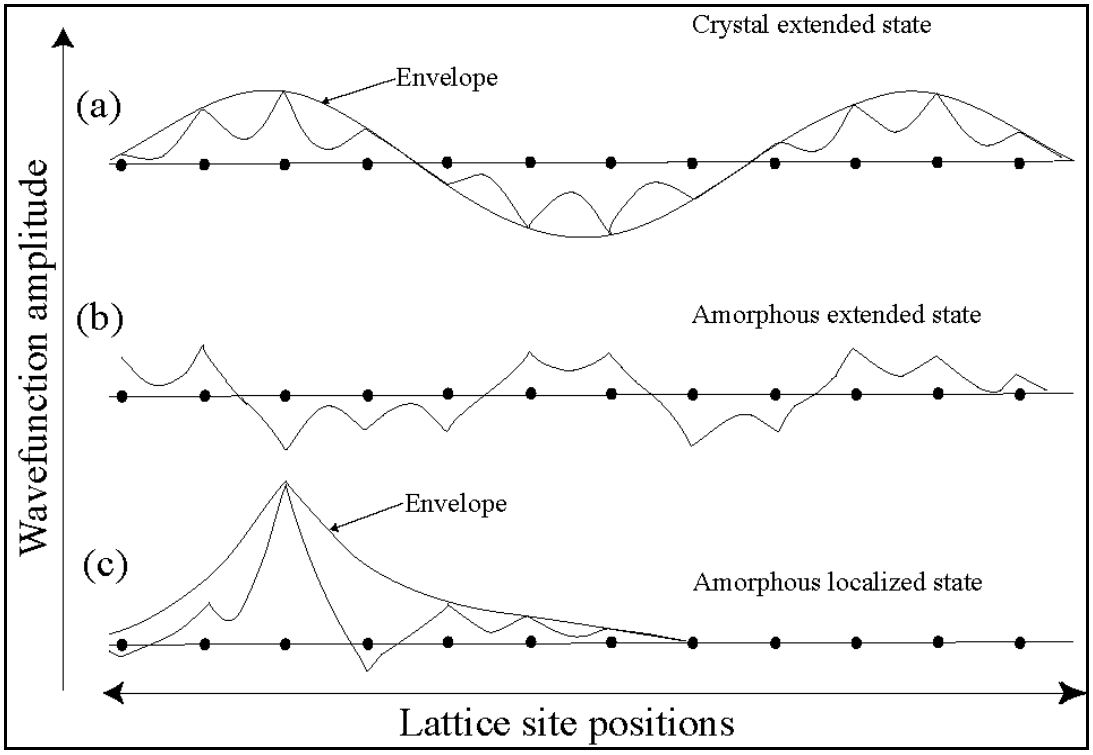

Figure 2.1: Illustration of the wavefunctions of (a) crystal extended, (b) amorphous extended and (c) amorphous localized states [11].

It is not conceivable to treat the electrical transport of an amorphous material without the distribution(s) of density of states (DOS) in mind, which are closely related to its structure. The so-called amorphous structure is based on 3 features: long range disorder, more or less short range order and coordination defects. Consequently the presence of short range order avoids a complete amorphization of the material, i.e., the majority of the states within a band possesses extended wave functions although, their phase coherence lengths are relatively very short (even reduced to interatomic distance at the limit) [12].

In the presence of long-range order (translational symmetry) electron can move unrestrictedly throughout the whole system (Bloch type state wave function $\psi(r) = U_k(r)e^{ikr}$ where $U_k(r)$: amplitude modulated with the lattice periodicity and 'k': wavevector or quasimomentum defining the state). There is a constant phase relation between the wavefunction at different lattice sites as shown in Figure 2.1-a. But, in real crystal, due to phonon scattering phenomena a finite mean free path or coherence length 'L' is established. However, in amorphous structure, there are always distortions of the ideal order causing scattering of electrons and the wavefunction loses its phase coherence over a distance of one or two inter-atomic distances as shown in Figure 2.1-b. A stronger disorder confines the wavefunction to a small volume of material and causes electron localization as shown in Figure 2.1-c.

2.1.1 Tail DOS from Band Edges:

Within this last frame, the quasimomentum k does not remain a state defining 'good quantum number'. But short range order, in the sense of chemical bonding, exists with both more or less distorted bond lengths and bond angles.

Beyond a limit, the above mentioned distortion around a site at the average position R leads to a local trapping potential V(R-r), which in turn localizes one of the band energy level E (In this respect, the total number of states remaining conserved, the DOS band width may broadened more or less on either side depending on the strength of local perturbations). The overall amount of V, reflecting the strength of local distortion, is related to the defect formation energy such that larger defect formation energy decreases the thermodynamical existence probability of this defect. Taking into account the independence and randomness of each local potential, the probability of occurrence of a local potential V is reasonably expected to be a one sided Gaussian relation as [13-18]:

$$P(V) = \frac{1}{\sqrt{2\pi\sigma^2}} \exp(-\frac{V^2}{2\sigma^2}) \qquad (2.1)$$

Where P(V) gives the probability of occurrence of a local potential (V) and σ is the standard deviation from the mean value. In this respect, σ may be taken as a degree of average distortion or disorder parameter. In the above expression (2.1), the extended state band edge is taken as reference level so zero.

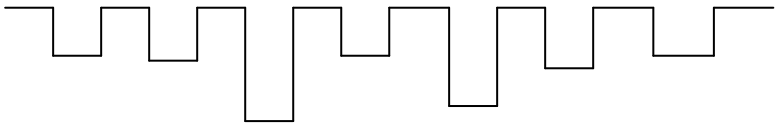

Figure 2.2: A simplified model of potential fluctuations due to distorted bond lengths and bond angles.

The effective extensions of each local potential should remain within about the interatomic distance, at least the core effect of the distortion might be expected to be very narrow. In this respect, the effective mass and the dielectric constant of the medium could not be used for these atomic ranges. Although a spherical symmetry of the local distortion being not irrefutable, here for a first insight, a spherical square well may be assumed (Figure 2.3):

$$V(r-R) = -U \quad for \quad r-R < a \quad with \quad U > 0$$
$$V(r-R) = 0 \qquad for \quad r-R > a \tag{2.2}$$

Where 'U' denotes the well depth, 'a' is the well radius.

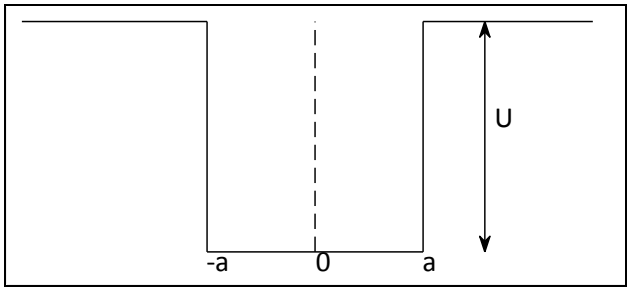

Figure 2.3: A typical potential well.

The solution of the Schrodinger equation leads to [19]:

$$a\cot(\alpha a) = -\beta \tag{2.3}$$

Where $\alpha = \sqrt{\frac{2m}{\hbar^2}(U - |E|)}$; $\beta = \sqrt{\frac{2m}{\hbar^2}}$; the decaying wave function outside the well being exp(-βr) /r and |E|=-E being the binding energy measured from the band edge. The Heisenberg uncertainty relation (ΔrΔp =h) in the potential well defines the minimum kinetical (deduced from the minimum momentum):

$$V_0 = \frac{\pi^2 \hbar^2}{8ma^2} \tag{2.4}$$

Consequently, any potential well shallower than V_0 is not trapping potential. The numerical or graphical solutions of the equation (2.3) carries out that [19, 20]:

For $0<U<V_0$, there is no bound state

For $V_0<U<9V_0$, there is one bound state

For $9V_0<U< 25V_0$, there is two bound states (E, E')

For $(2n-1)^2V_0<U< (2n+1)^2V_0$, there are n bound states (E, E'…, E (n+1))

Realistically, the eventual excited states could not be kept as true binding states, as a result, only fundamental state (one bound state) may be reasonably considered here.

The numerical solution approximately points out three main regions for curves $U(E)^2$ vs. E [14,20]:

a) 1st region: Shallow binding energy for $\frac{|E|}{V_0} < 0.1$.

$$U^2 \approx V_0^2 \left[1 + (8/\pi)\sqrt{\frac{|E|}{V_0}} \right] \tag{2.5}$$

b) 2nd region: Intermediate binding energy for $0.1 < \frac{|E|}{V_0} < 1$.

$$U^2 \approx 4/(\tau)^2 V_0^2 |E| + \text{constant} \tag{2.6}$$

c) 3rd region: Deep binding energy for $1 < \frac{|\mathrm{E}|}{\mathrm{V}_0}\mathrm{eV}$.

$$|\mathrm{E}| = U - V_0 \approx U \tag{2.7}$$

The localized density of tail states N(E) can be obtained, taking into account the spin factor '2', by using the relation (2.1):

$$N(E)dE = 2N_L P(U)dU \tag{2.8}$$

Where N_L is the total number of local trapping potential sites per unit volume and $P(U)dU$ is the probability that U is between U, U+dU. Using the relations (2.4), (2.5), (2.6) and (2.7), one can approximate the expression of N(E) as follows:

$$N(E) \propto \exp[-(|E| / E_z)^z] \tag{2.9}$$

Where z =1/2 and $E_{1/2} = [(\tau)^2\sigma^4] / 2(2V_0)^3$; z =1 and $E_1 = [(\tau)^2\sigma^2] / 2V_0$; z =2 and $E_2 = \sigma\sqrt{2}$ for shallow, intermediate and deep cases respectively.

The shallow case, corresponding to the first region located near the mobility edge, may be considered as a discussable transition region between extended and localized states.

As for the deep case, the value of the DOS along the third region is too low, since these states require considerably deeper and then less probable potential wells. Moreover, these states are practically omitted in presence of dangling bonds (DB) states of relatively higher density, located along the same region.

Approximately, the DOS of localized tail states may be admitted to be reduced to the ones supplied by the second region for the intermediate binding energy where z=1 in the relation (2.9):

$$N(E) \propto \exp[-|E| / \text{constant}] \tag{2.10}$$

Apart from tail states, deep sates may arise from coordination defects, the so-called dangling bonds (DB), leading to a distribution of relatively high density of deep states, located around the midgap (Figure 2.5). As the surrounding of each atomic site might be different in this randomly coordinated amorphous network, the

density of energy levels associated with these DBs, exhibits Gauss-like distribution. Taking into account the amphoteric nature of DBs (positive, neutral and negative charge states), a second Gaussian distribution (shifted along the energy axis due to the positive correlation energy of doubly occupied sites) might exist (Figure 2.4)

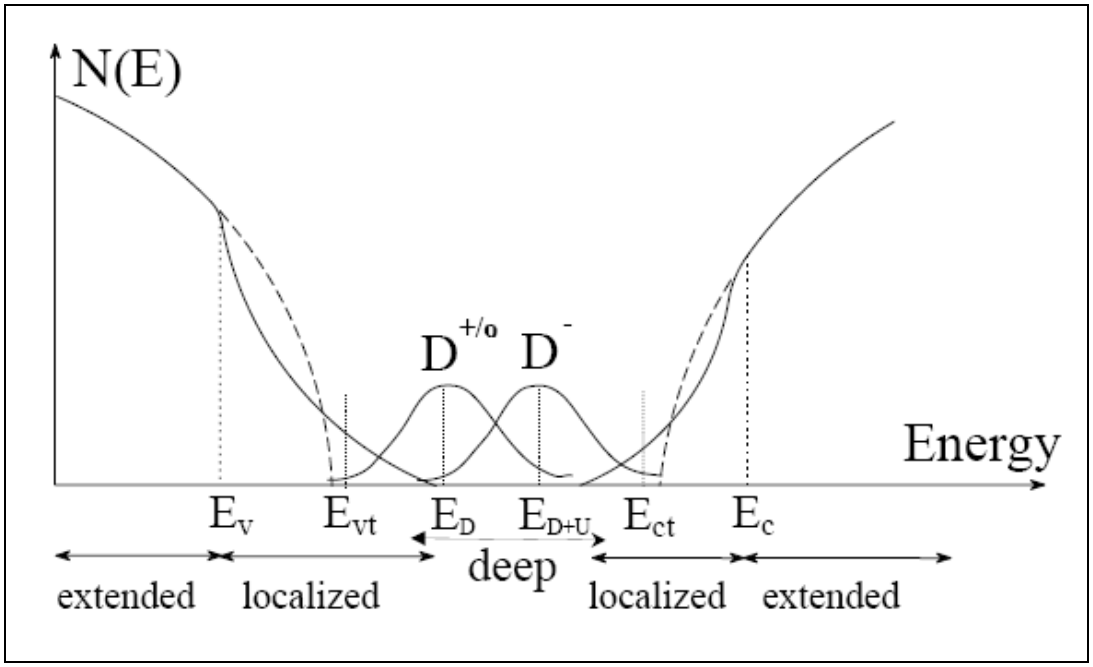

Figure 2.4: Typical DOS distribution in amorphous semiconductors.

In order to have a functional optoelectronic material, these localized states must be reduced by hydrogenation which saturates these bonds. Secondly, it increases the band gap of the material because, hydrogen is more electronegative than silicon and Si-H bonding states are respectively deep in the a-Si valence band (Figure 2.5-c)

Although hydrogenation is unavoidable for device quality a-Si:H thin films, the hydrogen atom itself seems behind the instable behaviors of devices under various stresses such as illumination, dc voltage application, etc…In this respect, the most sophisticated models describing the defect creation is the defect pool model.

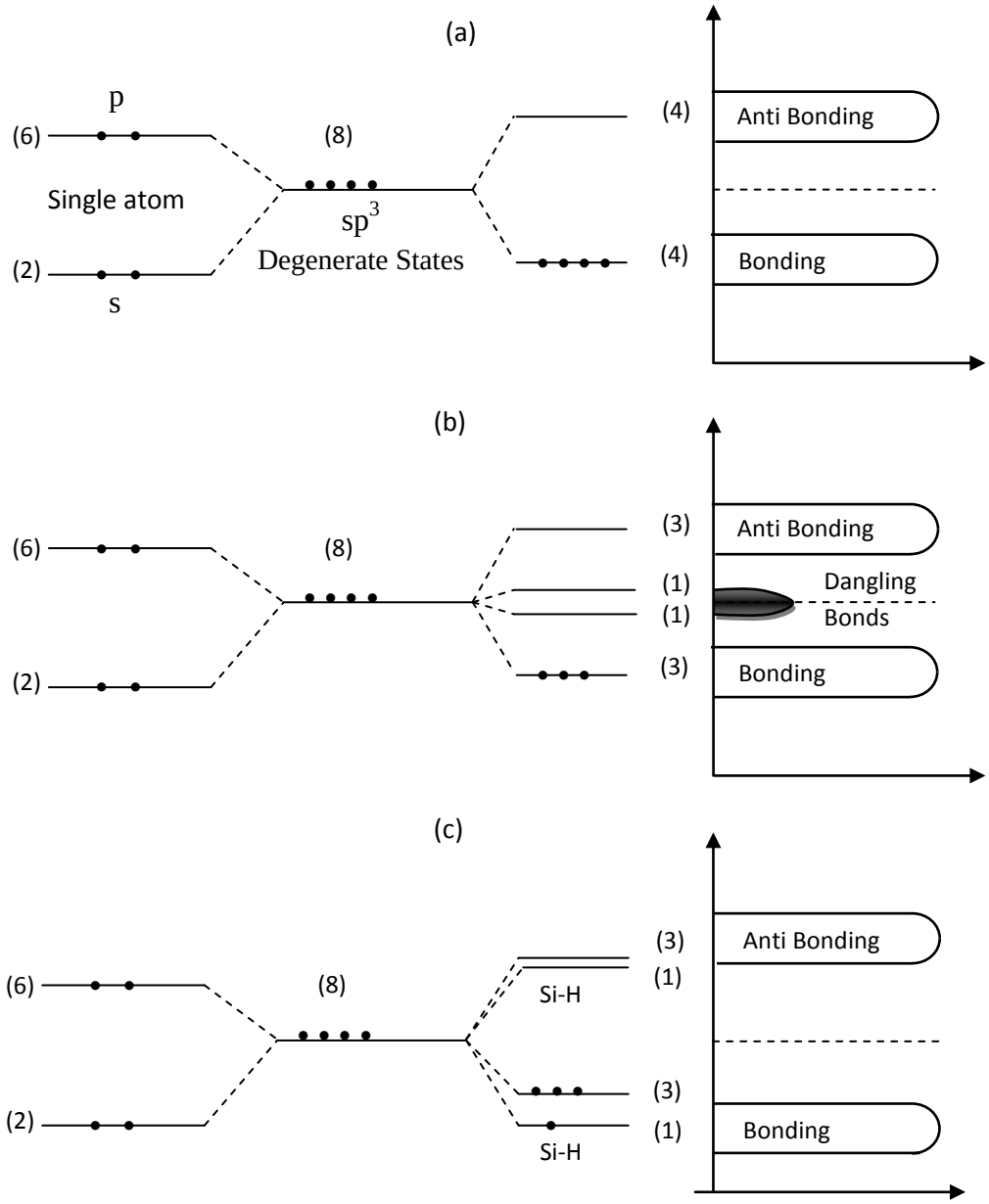

Figure 2.5 Bonding orbital diagrams for a-Si:H

2.2 Deep States-Defect Pool Model in a-Si:H Thin Films:

The defect creation and annihilation, mediated by the hydrogen migration under external stresses (such as dc electric field, illumination etc…) leads to the instabilities. The local bonding environments of hydrogen atom within these hydrogenated amorphous silicon alloys and its eventual displacement under the mentioned external stresses has been largely debated. The well established model is the defect pool model, first proposed by Smith and Wagner [21] and later developed by Powell et all [22]. Let us remind the main points of this model. First, as discussed in the previous section (the density of localized energy level E_{vt} of weak bonds (WBs) or tail states $g(E_{vt})$ is exponentially decaying as a function of E_{vt} from the edge of extended states E_v ($\equiv 0$ as reference) deep inside the energy gap($= N_{v0} \exp \frac{E_v - E_{vt}}{E_{v0}}$ with E_{v0} being disorder parameter, depending on the material and its growth conditions) as shown in figure 2.6.

There is a thermodynamical equilibrium between the existing WB density d(WB) of average energy E_{vt} (between E_{vt} and $E_{vt}+dE_{vt}$) and dangling bond (DB) density d(DB) of average energy E_D (between E_D and E_D+dE_D): $d(DB)_{eq} = d(WB)_{eq} \exp -\frac{U_F}{kT}$ with U_F formation energy. The sum of d(WB) and d(DB) is equal to a large pool of total WB density which would potentially be converted to the DB density of energy E_D:

$$d(WB)_{eq} + d(DB)_{eq} = g(E_{vt})P(E_D)dE_{vt} \tag{2.11}$$

where $P(E_D) = \frac{1}{\sqrt{2\pi\sigma^2}} \exp\left[-\frac{(E_D - E_{DM})^2}{2\sigma^2} \right] \equiv$ fraction of potentially available WBs (defect pool) for DB creation at the average energy E_D with E_{DM} = most probable DB energy, $\sigma =$ pool width (which is a characteristic measure of the actual disorder together with E_{v0} of the tail state distribution). Note that in the above relation (2.11), WBs corresponding to each infinitesimal interval dE_{vt}, have been considered as different chemical species; all the WBs from energy E_v to ∞ should be integrated [23-25].

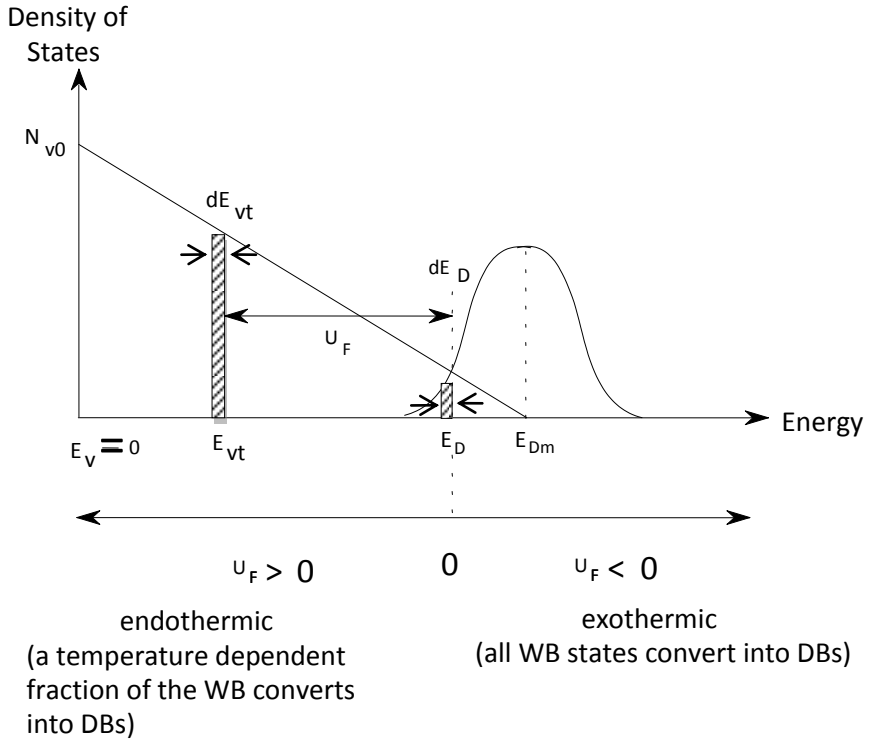

Figure 2.6: Illustration of WB_s conversion to DB_s (change from a bonding state E_{vt} in the valance band tail to non-bonding state E_D around the mid-gap).

2.2.1 Role of Hydrogen in defect creation

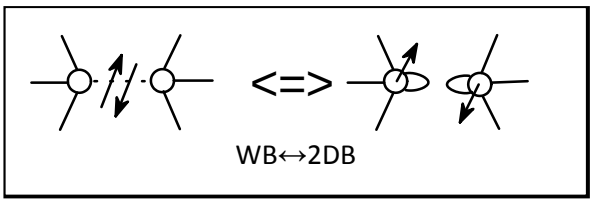

Figure 2.7. Schematic model for the weak bond-dangling bond conversion.

The chemical equilibration process due to the interconversion of the WBs and DBs contains an inconsistency since a configuration where two DBs (with spin-up and spin down) at the same site contradict the ESR experiment which points out an isolated neutral DB(with an active single spin). As this pair could not move away from each other at relatively low temperature, a mobile species, probably interstitial hydrogen atom, might intervene in the microscopic process [26,27] as illustrated schematically through the chemical reaction diagram below:

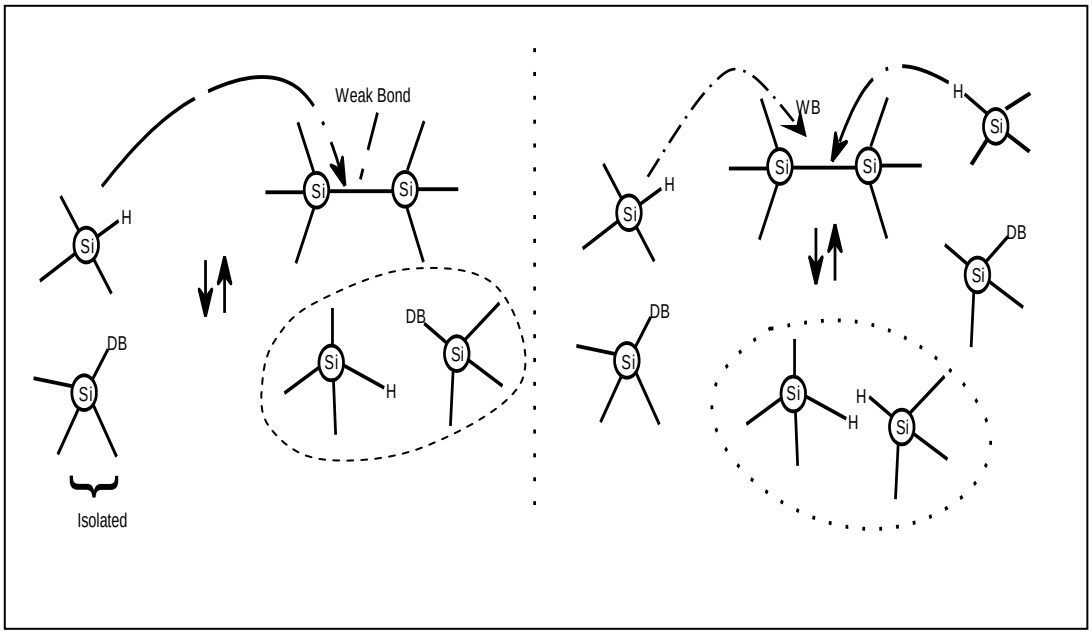

Figure 2.8: The eventual hydrogen involved (or mediated) equilibrium or equilibration. Note that in the first picture, two defects are formed, one originated from the isolated (SiH) bond, the second (SiHDSi) originated from the singly hydrogenated (SiSi) bond (i.e., $SiH + (SiSi)_{WB} \leftrightarrow DB + SiHDSi$). However, for the second case, SiSi bonds can have only zero or two H atoms which means that the correlation energy (the extra energy cost of putting a second hydrogen atom in the bond compared to the single hydrogen case) for H occupancy is negative ($2SiH + (SiSi)_{WB} \leftrightarrow 2(DB) + (SiHHSi)$).

$$SiH + (SiSi)_{WB} \leftrightarrow DB + SiHDSi \qquad (2.12\text{-a})$$

$$2SiH + (SiSi)_{WB} \leftrightarrow 2(DB) + (SiHHSi) \qquad (2.12\text{-b})$$

In the reactions above, the hydrogen atom is strongly bound to Si (binding energy of Si-H is about 3.4eV). This bound hydrogen might be released from this site to mobile (or interstitial) site through multiple excitations along “localized” states between SiH site and mobile site. As a result, interstitial hydrogen (H_I) and interstitial hydrogen site (I) should be introduced as species involving in the following equilibrium or equilibration chemical reaction:

$$SiH + (I - H_I) \leftrightarrow DB + H_I \qquad (2.13\text{-a})$$

$$(SiHDSi)+(I-H_I)\leftrightarrow SiSi+H_I \quad (2.13\text{-b})$$

$$(SiHHSi)+(I-H_I)\leftrightarrow(SiHDSi)+H_I \quad (2.13\text{-c})$$

According to reaction 2.13-a, which forms the DB defect on the isolated SiH site should not be energetically favorable since the energy considerations of the dangling bond defects require that the SiHDSi type DB concentration, by far, exceeds that of the isolated type DB concentration, so isolated DB's are omitted. Consequently, the equation 2.13-b and c become the main reactions of equilibrium and equilibration: this microscopic model involves the release of a mobile interstitial hydrogen atom (H_I), from a SiHHSi complex in the valence band tail to create one DB (SiHDSi) (depicted in the figure 2.9).

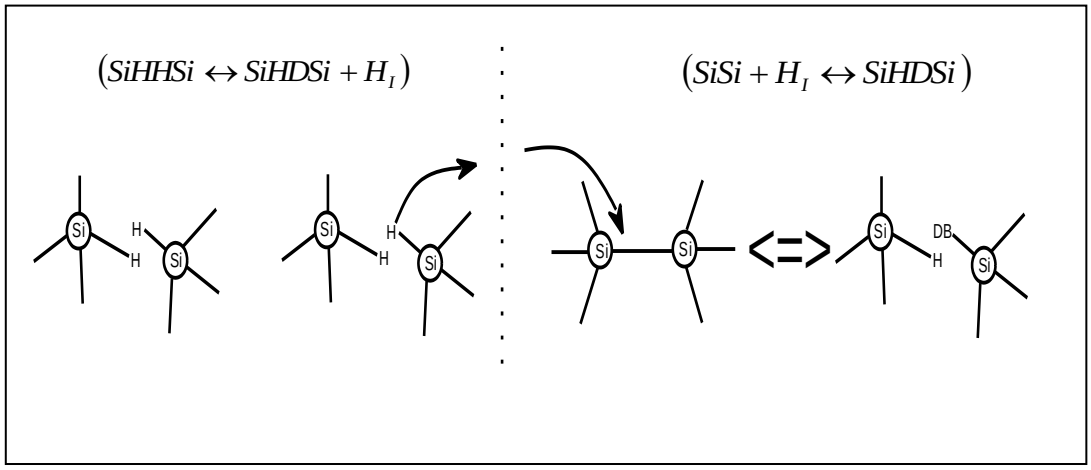

Figure 2.9: Schematic illustration of H diffusion through the network. Note that the mobile H inserts into a SiSi bond at remote site to give a second DB.

2.2.2 Analysis of Deep states Distributions:

The addition of the above two successive reactions give an overall reaction:

$$(SiHHSi)+(SiSi)\leftrightarrow 2(SiHDSi) \quad (2.14)$$

a) For $U_H<0$ case: For negative correlation energy of H atom (the extra energy cost of putting a second hydrogen atom in the bond compared to the single hydrogen case): taking into account the energy distribution of both WBs and DBs, the above expression (2.14) represents the superposition of very large number of

reactions. In this respect, for most SiSi bonds, the hydrogen correlation energy is negative ($U_H<0$), and then the reaction (2.14) would be from right to left side only. In other words, although both the breaking of a weak bond (rather than normal one) is favorable for inserting a single H atom into a SiSi bond (→SiHDSi) and a strain energy (E_{vt}-E_v) should be supplied for inserting double H atom into SiSi bond(→SiHHSi), experiments have shown that the doubly occupied sites (SiHHSi) are dominant (about95% of hydrogen might be stored in that form). i.e., there should be equilibrium between SiHHSi sites and normal SiSi sites [26] (since H concentration seems independent of the energy E_{vt} of weak bond (WB). Let us apply the law of mass action for the equations (2.13-b) and (2.13-c) which relates the concentration of SiHHSi sites to the normal SiSi sites:

$$\frac{[SiSi]\ [H_I]^2}{[SiHHSi]\ [I-H_I]^2} = \exp\left[-\frac{\Delta E_-}{kT}\right] \qquad (2.15)$$

Where $\Delta E = 2E_{H_I} + 2E_{vt} - 4E_{SiH} - (E_{vt} - E_v)$, here $E_{vt} - E_v$ = strain energy

$=2E_{H_I} + 2E_v - 4E_{SiH}$ = which is independent of E_{vt}

And,

E_v = Electron energy in the valence band mobility edge (electron energy in a normal SiSi site).

E_{H_I} = Electron energy in a mobile (interstitial) neutral hydrogen atom.

E_{SiH} = Electron energy in a-Si:H bond

In the relation (2.15) let us, first assume that [I-H] ≈ [I] and second consider the total concentration N of normal valence electron = 2[SiSi], N = $2x10^{23}cm^{-3}$; [H] = the total concentration of hydrogen atoms in a-Si:H films ≅ 2[SiHHSi] = $5x10^{21}cm^{-3}$ if a-Si:H films contain 10 at % H for example. Consequently, in the relation (2.15),

$$[SiSi]/\ [SiHHSi] = N/[H] \qquad (2.15\text{-}1)$$

In light of above approximations,(2.15) simplifies as:

$$\frac{[H_I]}{[I]} = \left(\frac{H}{N}\right)^{1/2} \exp\left[-\frac{\Delta E}{2kT}\right] \qquad (2.15\text{-}2)$$

b) For $U_H>0$ case: In the valence band tail ,along the weak bonds, U_H might progressively become positive ($U_H>0$) and then singly H occupied SiSi sites are favored leading to SiHDSi type DB defect sites, as a result the reaction (2.14) would be from left to right. In other words, as the isolated DBs, originated from isolated SiH sites are neglected, for the evaluation of DB density, SiHDSi sites should be exclusively considered. After applying the law of mass action to the relation (2.13-b), the following relation is obtained:

$$\frac{\delta[SiSi]_{eq}[Hi]}{\delta[SiHDSi][I-Hi]} \approx \frac{\delta[SiSi]_{eq}[Hi]}{\delta[SiHDSi][I]} = \exp\left[-\frac{\Delta E_+}{kT}\right] \qquad (2.16)$$

Where $\Delta E = E_{Hi} + 2E_{vt} - 2E_{SiH} - E_D'$

E_D = Electron transition energy from top of valence band to the unoccupied DB.

$E_D' = E_D + TS$ with $S = k\ln\left[\frac{f^0(E_D)}{2}\right]$ = electron entropy at the DB state since there are two alternatives (spin up and spin down), $f_0(E_D)/2$ being the occupancy probabilities for each case (here may be defined as the defect chemical potential). Using(2.15-1), (2.16) becomes

$$\frac{\delta[SiSi]_{eq}}{\delta[SiHD]} = \left(\frac{N}{H}\right)^{1/2} \exp\left[\frac{E_v + E_D' - 2E_{vt}}{kT}\right] \qquad (2.16\text{-}1)$$

Where, as defined by the relation (2.11), $\delta[SiSi]_{eq}$ = equilibrium concentration of weak bonds (WB) between E_{vt} and $E_{vt}+dE_{vt}$, $\delta[SiHDSi] \equiv dD(E_D,E_{vt})dE_D$ = concentration of dangling bonds (DB) between E_D and E_D+dE_D.

$\delta[SiSi]_{eq} = \delta[SiSi]_{total} - \delta[SiHDSi]$ with $\delta[SiSi]_{total}$ is the density of all the WB states between E_{vt} and $E_{vt}+dE_{vt}$ which would form (potentially) DB defects between E_D and E_D+dE_D and represented by equation (2.11). In the light of this information, using the relations (2.11) and (2.16-1) the elemental DB density $dD(E_D, E_{vt})$ can be expressed as:

$$dD(E_D,E_{vt}) = \frac{g(E_{vt})P(E_D)dE_{vt}}{1+(N/H)^{1/2}\exp\left[\dfrac{E_v + E_D{}' - 2E_{vt}}{kT}\right]} \tag{2.17-1}$$

$$dD = \frac{g(E_{vt})P(E_D)dE_{vt}}{1+\exp\left[\dfrac{E_v + E_D{}' - 2E_{vt} + 1/2\ln\left[N/H\right]}{kT}\right]} \quad \text{with} \quad E_D{}' = E_D + kT\ln\left[\frac{f^0(E_D)}{2}\right] \tag{2.17-2}$$

Defining a new parameter $\left(2\xi \equiv E_v + E_D + kT\ln\left[f^0(E_D)/2\right] + kT\ln\left[N/H\right]\right)$ and integrating from E_v to ∞ (i.e., along the whole valence band tail):

$$D(E_D) = \int_{E_v}^{\infty} dD(E_D,E_{vt}) = \int_{E_v}^{\infty} \frac{g(E_D)P(E_D)dE_{vt}}{1+\exp\left[2(\xi - E_{vt})/kT\right]} = \underbrace{\int_{E_v}^{\xi}}_{\substack{\xi > E_{vt} \\ I_1}} + \underbrace{\int_{\xi}^{\infty}}_{\substack{\xi < E_{vt} \\ I_2}} = I_1 + I_2 \tag{2.17-3}$$

with

$$I_1 \approx \int_{E_v}^{\xi} N_{v0}\exp\left[\frac{E_v - E_{vt}}{E_{v0}}\right]\frac{1}{\sqrt{2\pi\sigma^2}}\exp\left[-\frac{(E_D - E_{DM})^2}{2\sigma^2}\right]\exp\left[-\frac{2(\xi - E_{vt})}{kT}\right]dE_{vt} \tag{2.17-4}$$

(A Boltzmann fraction of WB are converted)

$$I_2 \approx \int_{\xi}^{\infty} N_{v0}\exp\left[\frac{E_v - E_{vt}}{E_{v0}}\right]\frac{1}{\sqrt{2\pi\sigma^2}}\left[-\frac{(E_D - E_{DM})^2}{2\sigma^2}\right]dE_{vt} \tag{2.17-5}$$

(All the WB are converted)

Performing integration and taking $E_v \equiv 0$ yields the famous defect pool distribution:

$$D(E_D) = \left[\frac{2}{f^0(E_D)}\right]^{\frac{kT}{2E_{v0}}} P\left(E_D + \frac{\sigma^2}{2E_{v0}}\right)\gamma \tag{2.18-1}$$

with

$$\gamma \equiv \frac{2N_{v0}E_{v0}^2}{2E_{v0} - kT}\left[\frac{H}{N}\right]^{\frac{kT}{4E_{v0}}}\exp\left[-\frac{\left(E_{DM} - \dfrac{\sigma^2}{4E_{v0}}\right)}{2E_{v0}}\right] \tag{2.18-2}$$

The above expression (2.18-1) gives the density of DB states (DOS) at equilibrium (this equilibrium is among WBs, DBs, electronic free carriers and the mobile interstitial hydrogen with each other).

In the frame of the above analysis a) the role of hydrogen and b) the amphoteric nature of the DB states should be kept in mind:

a) Although the hydrogen is not necessary for the "end result", first it provides a microscopic mechanism during the defect creation/equilibration process and second it provides an extra entropy for decreasing defect formation energy (since there are several orders more hydrogen sites than DB defects, i.e., a DB defect at energy E_D gains an extra entropy from those hydrogen sites that would also form a DB defect at the same energy E_D)

b) As during the film growth at the temperature interval of 200-300 ˚C, the amphoteric nature of a neutral DB (i.e., it can release its electron or capture an extra one) leads to three different defect distributions (negatively charged one, located below Fermi level E_F, neutral one around E_F, and positively charged one above E_F) [26, 27] (See figure 2.10). The effect of these various charge states is twofold also in the calculation of defect chemical potential: first the average energy $<E_D>$ of the electron on the DB defect should be considered. In other words, the mean energy $\langle E_D \rangle$ of the electrons in the DB states may be expresses as follows:

$$\langle E_D \rangle = E_F f^+(E_D) + E_D f^0(E_D) + (2E_D - E_F + U) f^-(E_D) \qquad (2.19)$$

with f^+, f^0 and f^- are the probabilities of the DB defect in each charge state [28];

$$(f^+)^{-1} = 1 + 2\exp[(E_F - E)/kT] + 2\exp[(2E_D - 2E + U)/kT] \qquad (2.20\text{-}1)$$

$$f^0 / f^+ = 2\exp[(E_F - E)/kT] \qquad (2.20\text{-}2)$$

$$f^- / f^+ = \exp[(2E_D - 2E - U)/kT] \qquad (2.20.3)$$

with $f^+ + f^- + f^0 = 1$.

Second, the extra entropy, S_e $\left(=-k\left[f^+\ln f^+ + 2f^0/2\ln f^0/2 + f^-\ln f^-\right]\right)$, gained by different possibilities of charge states should be taken into account [29]. Consequently, the chemical potential of DB defect at E_D becomes [26]:

$$E_D' \equiv \mu_D(E_D) = \langle E_D \rangle - TS_e \tag{2.21}$$

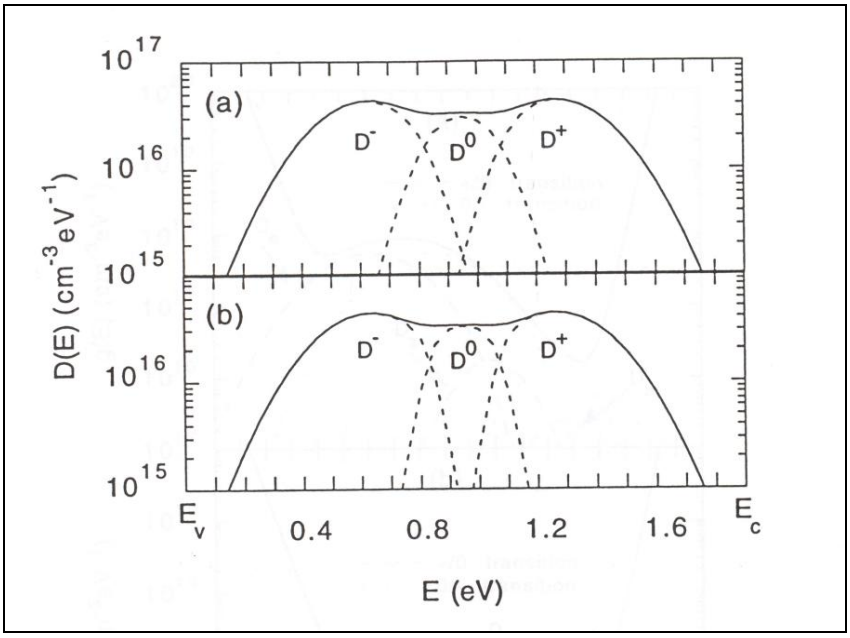

Figure 2.10 Density of each charge component within the gap at T=200 °C (a) and 40 °C (b), respectively.

At the growth temperature, there is an immediate equilibrium among WBs, DBs, electronic free carriers and interstitial hydrogen with each other. At room temperature, the above situation is almost frozen-in with three different defect distributions within the gap (Figure 2.10), i.e., D(E) could not be changed by applied voltage, but it may be composed of three components of different charge states :positive (+), neutral (0) and negative (-) following the relative position of E_F. These distributions, built at growth temperature, are represented by D_h, D_z and D_e respectively. Each one can be changed from positive to neutral, from neutral to negative by changing E_F or by making electronic transition from valence to these localized states. Keeping in mind the shift in energy of negatively charged DB distribution due to the positive correlation energy of its pair of electrons; the above

cited three different distributions (D_e, D_h and D_z) become six different distributions ($D_e^{+/0}, D_e^{0/-}, D_z^{+/0}, D_z^{0/-}, D_h^{+/0}, D_h^{0/-}$) covering the whole energy gap [26] as shown in figure 2.11:

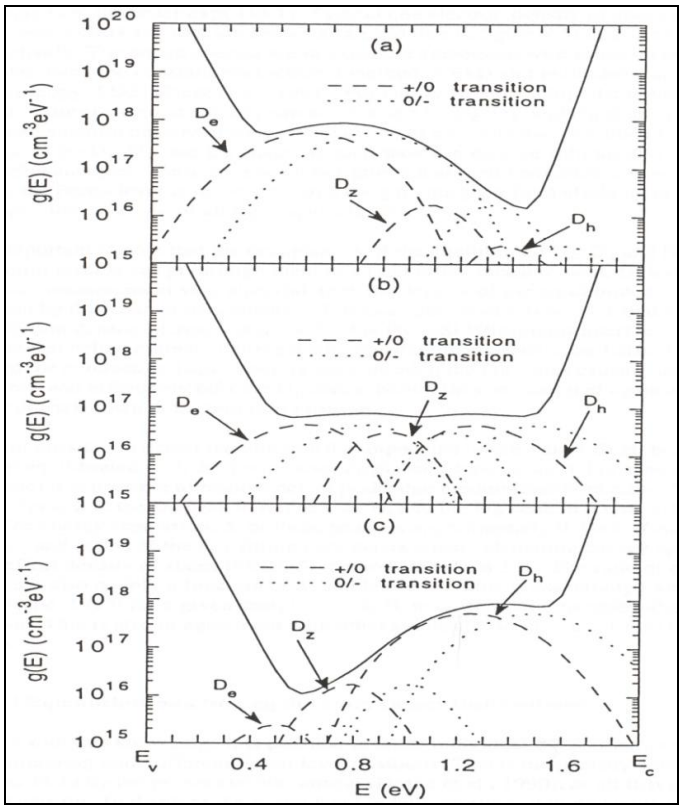

Figure 2.11 Density of states splits into +/0 and 0/- distributions for (a) n type a-Si:H ; (b) for intrinsic a-Si:H. and (c) for p type a-Si:H.

CHAPTER 3

ELECTRONIC TRANSPORT

3.1 Introduction:

For the electrical transport, first of all, the previously outlined distributions of localized electronic states should be in mind. Moreover, the intentional electrical conductivity modulation by foreign atom doping, although feasible, seems very complex process.

In amorphous material, there is no rigidly defined site (on the contrary of crystalline case) such that an impurity atom can adapt itself to local environment to optimize its own bonding following the N/8-N rule [30]. This rule suggests that the conventional dopants for the crystal Si (phosphorus for n-type, boron for p-type) should be 3-fold coordinated in amorphous medium and therefore they are mainly inactive as electronic dopants; in other words, actually the doping is not forbidden but severely limited. That is as a partial deviation from N/8-N, a small fraction of dopant concentration might have 4-fold coordination leading to a doping site. This tetrahedral sp^3 configuration whose formation energy is too high, might be energetically slightly favored only in presence of a charge compensating deep state capturing the anti-bonding electron of the donor or transferring electron to the bonding acceptor. This does not mean that this dopant-defect pair is necessarily on adjacent sites; they may be very distant from each other, but they may interact with the charge carrier distribution (Fermi sea) whose energy is defined by the Fermi energy E_F .This carrier exchange with the Fermi sea modifies the relative potion of E_F within the pseudo-gap, by the way the doping effect is resulted. The above outline mechanism carries out the complexity of the doping mechanism without mentioning the indispensible effect of hydrogenation which transforms the mediocre non-dopable amorphous material into a relatively dopable one enormously reducing (over 10^5 times) the dangling bond based deep states [11]. It is

reasonable that the eventual doping mechanism(s) is expected to be much more complex in the alloys of Si such as a-SiO_x:H

In crystalline semiconductors, extended states are the only place that the electronic transport occurs. The charge carriers in the extended states treated as free particles as in the metal since the wavefunctions of extended states overlap coherently. When an external field F is applied an additional directional motion will be superimposed upon the thermal motion of the carriers, leading to a current density J. J is proportional to F, the constant of proportionality being σ:

$$J = \sigma F \quad \text{with} \quad \sigma = qn\mu \quad \text{and} \quad \mu = \frac{q}{m^*}\tau \tag{3.1}$$

Where q is the elementary charge, n is the carrier concentration, μ is the mobility of the carriers m* is the effective mass that involves the effect of crystal periodic potential and τ is the mean collision time of the carriers.

3.2 Electronic Conduction Throughout Amorphous Semiconductors:

In light of the previous DOS analyses, at least two different electrical conduction mechanisms exist in amorphous structure:

a) Extended state conduction where mobility $\mu \neq 0$

b) Localized state conduction where mobility $\mu = 0$

3.2.1 Extended State Conduction:

Under the electric field F, a current density J appears: J=σF. With

$$\sigma = \int N(E)q\mu(E)[1 - f(E,T)]f(E,T)dE \approx \int N(E)q\mu(E)f(E,T)dE \tag{3.2}$$

Where $f(e,T)$ is the Fermi function. Both transport due to the electrons above E_F and holes below E_F contributed to above integral. But if the conductivity takes place far from the fermi energy by single type of carrier(since degenerate doping seems not possible for amorphous semiconductors), non-degenerate statistics may be

applied and Boltzmann distribution function can be used to describe the occupancy of states, then the above equation converts into:

$$\sigma = \int N(E)e\mu(E)\exp\left[\frac{(E-E_F)}{kT}\right]dE \equiv \frac{1}{kT}\int \sigma(E)\exp\left[\frac{(E-E_F)}{kT}\right]dE \qquad (3.3)$$

with $\sigma(E) \equiv N(E)e\mu(E)kT$ .In section (2-1), the shallow tail states, located near mobility edge, are considered as a transition region between extended and localized states. In this respect, two cases may be envisaged [6]: $\sigma(E)$ increases either monotonically with E around the mobility edge E_c or abruptly at E_c. Practically the last case is considered and assuming N(E) ≈ constant = $N(E_c)$, it leads to:

$$\sigma = \sigma_{\min}\exp[\frac{-(E_c-E_F)}{kT}] \text{ with } \sigma_{\min} = N(E_c)e\mu_0 kT, \mu_0 = \text{mobility at } E_c \qquad (3.4)$$

3.2.2 Localized State Conduction by Nearest Neighbor Hopping:

Although there is no macroscopic conduction throughout localized states at T=0 K, at higher temperature, quantum mechanical tunneling transitions between localized states, might lead to conduction. For discussing more precisely, the transition rate by tunneling from the occupied localized level E_i to the empty one E_j is given by [47]:

$$r_{ij} = \nu_0 e^{-2\alpha R_{ij}} e^{-\frac{[E_j-E_i]}{kT}} \quad \text{if } E_i < E_j \text{ (upward transition)} \qquad (3.5\text{-a})$$

$$r_{ij} = \nu_0 e^{-2\alpha R_{ij}} \quad \text{if } E_i > E_j \text{ (downward transition)} \qquad (3.5\text{-b})$$

where ν_0 = attempt-to-escape (or phonon) frequency, R_{ij} = distance between the relevant localized sites, α^{-1} = characteristic localization length of the wave function envelope around the trap sites as $e^{-\alpha x}$. Here α may be taken as weakly trap energy E dependent [31]

$$\alpha = \frac{\sqrt{m(E_0-E)}}{\hbar} \qquad (3.6)$$

With E_0 = band edge and m = electron mass. The transfer probability P_{ij} from E_i to E_j:

$$P_{ij} = f(E_i)[1 - f(E_i)]r_{ij} \tag{3.7}$$

At steady state, $P_{ij}=P_{ji}$, reflecting a balance between any pair of localized levels above E_F. This symmetry may be disturbed by the applied field F, leading to a net flux of carriers by favoring one direction where an electron increases its local energy by qFR_{ij} as a result of hopping against F over a distance R_{ij}. In this respect, the consideration of downward transition (equation 3.5-b) is enough for calculating the total field induced charge flux [32].

Within this frame, the charge transport is achieved in two steps; first a carrier is thermally excited to an empty energy level E from an occupied state (near E_F), then it hops downward to nearest neighbors of energy $E' \le E < E_m$ and of average concentration.

$$\overline{N} = \int_{E_F}^{E} N(E')[1 - f(E')]dE' \approx \int_{E_F}^{E} N(E')dE' \tag{3.7-1}$$

a) for Gauss distributed DB states of density $N(E') = \frac{N_T}{\sqrt{2\pi}\sigma_s}\exp[-\frac{(E'-E_{DM})^2}{2\sigma_s^2}]$ with N_T = total deep(DB) trap density, σ_s=standard deviation:

$$\overline{N} \cong \frac{N_T}{\sqrt{\pi}}\ erfc\left[\frac{E_m - E}{\sqrt{2}\sigma_s}\right]. \tag{3.7-2}$$

b) For exponentially distributed tail states of density (E') = $D_0\exp[-(E_C-E')/E_0]$:

$$\overline{N} \cong E_0\ D_0\exp[-(E_C-E')/E_0] \tag{3.7-3}$$

The expression (3.7-1) supplies $R(E) = \left[\frac{4\tau}{3}\overline{N}\right]^{-1/3}$. The differential current density per unit energy interval around the energy E may be expressed as:

$$\left(\frac{\Delta J}{\Delta E}\right)_E = qR\frac{dr}{dE}\Delta n \text{ with } \Delta n = N(E)\,f(E)qRF \tag{3.8}$$

From $\left(\frac{\Delta J}{\Delta E}\right)_F = \left(\frac{\Delta \sigma}{\Delta E}\right)_E F$, the differential conductivity may be defined as:

$$\left(\frac{\Delta \sigma}{\Delta E}\right)_E = q^2 R^2 N(E) f(E) \left(\frac{dr}{dE}\right)_E \tag{3.9}$$

Where the differential transition rate $\frac{dr}{dE}$ may be expressed as below by using the relation (3.5-b) and (3.6)

$$\left(\frac{dr}{dE}\right)_E = r \ln\left(\frac{r}{\nu_0}\right)\left[\frac{4\sqrt{4\pi}}{9} R^3(E) N(E) - \frac{m}{\hbar^2 \alpha^2}\right] \quad \text{if} \quad \alpha = \alpha(E) \tag{3.10}$$

$$\left(\frac{dr}{dE}\right)_E = r \ln\left(\frac{r}{\nu_0}\right)\frac{4\sqrt{4\pi}}{9} R^3(E) N(E) \quad \text{if} \quad \alpha = \text{constant} \tag{3.11}$$

At relatively high temperature (around room temperature) within an amorphous material where the density of localized states is not exceptionally low, the contribution to the carrier transport of the tail states might be dominant compared to the one in the band of extended states (beyond the conventional mobility edge).The Fermi level E_F may be pinned by a high density of DB defects, deep in the gap. The thermal excitation of carriers towards higher energies increases the hopping probabilities of them since the exponentially increased density of tail localized states are accessible for hopping. In this respect, more or less, any energy level may contribute to the conductivity. However, both exponentially decreasing density of excited carriers and exponentially increasing DOS along the energy axis, a maximum contribution occurs within an energy interval ΔE around an average level E_T. In other words, apparent activation energy E_A may be defined as follows:

$$E_A \equiv E_T - E_F \tag{3.12}$$

Of course, E_A depends both on the degree of disorder (through DOS distribution along the tail region) and slightly on temperature (through thermal excitation). The overall conductivity, obtained from the integration of the relation (3.9) along the tail states, might lead to Arrhenius type thermally activated conductivity, similar to relation (3.4) of the extended state conductivity but with smaller activation energy:

$$\sigma = \sigma_0 \exp[\frac{-(E_A - E_F)}{kT} \tag{3.13}$$

3.2.3 Localized State Conduction by Variable Range Hopping:

As temperature decreases, the number and the energy of phonons decreases and then the more energetic phonon-assisted hopping will progressively become less favorable. As a result, carriers will tend to hop to larger distances in order to find sites which lie energetically closer than the nearest neighbor; this mechanism is the so-called variable range hopping. In order to find the most favorable hopping distance the exponent of $\exp\left[-2\alpha - \frac{E_{ij}}{kT}\right]$ should be minimized. For this purpose, let us express E_{ij} as a function of R .The number of states with energy difference E_{ij} within a distance R from a particular site is given by: $\frac{4\pi R^3}{3} N(E_F) E_{ij}$ where $N(E_F)$ = density of states per unit energy per unit volume. The electron can leave its site only if the number of accessible sites is at least one. Taking this into account, one gets for the average energy spacing between states near E_F level: $E_{ij} = \frac{3}{4\pi N(E_F) R^3}$. Inserting into the above transition rate equation: $P_{ij} = \omega_0 \exp\left[-2\alpha_L R - \frac{3}{4\pi N(E_F) kTR^3}\right]$. Minimizing the exponent term with respect to R, the maximum hopping distance can be evaluated: $R_m = \left[\frac{9}{8\pi\alpha N(E_F) kT}\right]^{1/4}$. Then, the transition rate would be: $P_{ij} = \omega_0 \exp\left[-\frac{A}{T^{1/4}}\right]$ with $A = 2\left[\frac{32\alpha^3}{9\pi k N(E_F)}\right]$. Finally, conduction expression turns into:

$$\sigma = \frac{q^2 R_m^2 \omega_0 N(E_F)}{6kT} \exp\left[-\frac{A}{T^{1/4}}\right] = \sigma_0(T) \exp\left[-\frac{A}{T^{1/4}}\right] \tag{3.14}$$

CHAPTER 4

TIME OF FLIGHT PRINCIPLES AND TECHNIQUES

One of the most important experiments concerning the transport and trapping mechanisms of amorphous semiconductors is the time of flight (TOF) photoconductivity technique. It is a method of charge transport analyses in low mobility solids. TOF photoconductivity measurements yield direct results of the carrier mobility and deep trapping time [34-36]. Thus the results imply the nature of the electronic transport in these materials which is very difficult to obtain by theoretically because of the non-periodic atomic structures of amorphous materials.

4.1 General Principles:

A thin film of highly resistive material with thickness L is placed between two electrodes and a voltage source is applied across the electrodes creating a uniform electric field. A laser pulse of strongly absorbed radiation is used for injecting charge carrier near the surface of sample. An oscilloscope is used to detect the current in the external circuit. Basic illustration of the TOF experimental set up shown in the figure 4-1. Rectifying electrodes should be used for avoiding charge injection in the bulk of the sample from the electrodes.

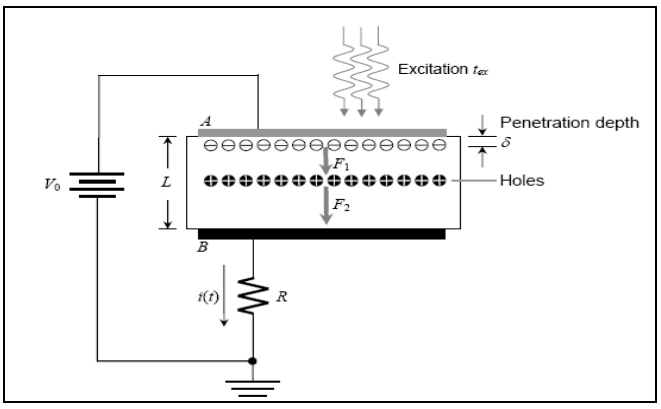

Figure 4.1: A simplified experimental diagram of TOF technique

After the voltage is applied across the electrodes, a laser pulse is allowed to be absorbed inside a very narrow region near to the surface of the specimen within about 80-100 nm depth where electron- hole pairs are created. Depending on the direction of the applied uniform electric field, one of the charge carriers (electrons or holes) is collected by the electrode where the incident laser radiation is absorbed. Other carriers drift across the sample by the applied electric field. While the carriers drift across the sample they induce a current through the external circuit. When the carriers reach the other electrode the current in the external circuit drops to zero. By reversing bias conditions the other charge carriers can also be examined without changing the experimental set up.

Some important requirements should be satisfied before commencing the TOF experiment.

1. Absorption depth of the incident radiation must be considerably less than the sample thickness ($\delta<L$) otherwise the transient sheet of charge carriers can not exist inside sample. Moreover the absorption depth δ should not be too small for avoiding the possibility of the generated carriers to be trapped by surface defects.

2. Transit time t_T of flight of the carriers should be smaller than the dielectric relaxation time τ_{rel} of the specimen ($t_T \ll \tau_{rel}$) that is the time required for excess charge carriers in the material to reach thermal equilibrium through the relaxation and recombination processes(since the photo-generated charge carriers should not recombine with carriers of opposite charge before they transfer through the sample. The only allowed mechanism to decrease the number of carriers is trapping).

3. Small signal conditions should be sustained during the experiment.

4. Duration of excitation (t_{ex}) should be smaller than t_T ($t_{ex} \ll t_T$).

4.2 The Charge Transport Mechanism:

The applied uniform electric field is perturbed due to the existence of sheet of mobile charge carriers. Thus the electric field behind (F_1) and in front (F_2) of the charge sheet can be found using simple electrostatic considerations (see figure 4.2):

$$F_1 = \frac{V_0}{L} - \frac{qp_0 w}{\varepsilon}\left(1 - \frac{x'}{L}\right); \qquad F_2 = \frac{V_0}{L} + \frac{qp_0 w}{\varepsilon}\frac{x'}{L} \tag{4-1}$$

Where p_0 = concentration of holes in the sheet , w = its width and ε = dielectric constant of the sample.

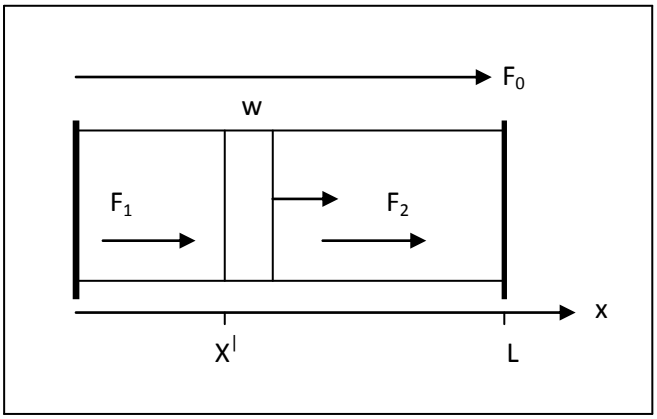

Figure 4.2: Modification of the electric field across the sample due to the presence of injected carriers.

If the amount of charge $p_0 wA$ in the sheet (with A = the illuminated cross sectional area) is kept sufficiently small such that $qp_0 w/\varepsilon \ll V_0/L$, the electric field in the sample becomes approximately uniform:

$$F_1 \cong F_2 \cong F_0 = V_0/L \tag{4.2}$$

Thus the number of charge carriers generated in a TOF experiment is also a critical quantity to satisfy equation (4-2) and it is known as small-signal condition and means the electric field inside the sample can be considered as uniform, and that the charge sheet has a constant drift velocity [37].

To obtain the photo current induced by the transit charge carriers the Shockley-Ramo theorem [38] can be used. Any optically generated elementary charge q experiences a force qF_0 due to the applied electric field F_0. Then these carriers drift by this force to the negative electrode within the transit time t_T by the constant drift velocity v_d:

$$v_d = \mu F_0 = \mu V_0/L \tag{4.3}$$

The induced photocurrent persists for the duration of transit time t_T and drop down to zero when the carriers reach the negative or collection electrode.

To obtain the amount of induced photocurrent work-energy theorem can be used. An energy $dW = V_0 i_{ph}(t)dt$ supplied by the battery to move the charge q by a distance dx by achieving a work $dW = q\frac{V_0}{L}dx$; this leads to the photocurrent $i_{ph}(t)$ in the external circuit:

$$i_{ph}(t) = \begin{cases} \frac{qv_d(t)}{L} = \frac{qp_0 wA}{t_T} & for \quad 0 < t < t_T \\ 0 & for \quad t > t_T \end{cases} \tag{4.4}$$

The small signal ac equivalent circuit of the system is given in figure 4.3 where the capacitance C_s the stray capacitance. The photocurrent i(t) produces a voltage drop v(t) across the impedance depicted in Fig.4.3.The relation between i(t) and v(t) may be simplified for two extreme cases: a) I-mode for $RC_s << t_T$, b) V-mode for $RC_s >> t_T$ [39, 40].

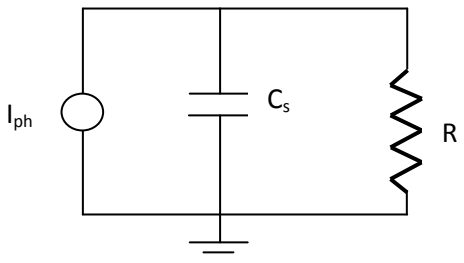

Figure 4.3: Small signal ac equivalent of TOF experiment setup.

a) I-mode:

$$v(t) = Ri_{ph}(t) \qquad \text{for} \qquad RC_s << t_T \tag{4.5}$$

From this expression it is obvious to see that the magnitude of the observed signal related to the photocurrent signal directly. An ideal I-mode signal reaches abruptly a constant value when the optical generation of carriers occurs, and it falls down to zero very sharply when the carriers reach the collecting electrode.

b) V-mode: alternatively, the V-mode signal is given as [39, 40]:

$$v(t) = \left\{ \begin{array}{ll} \dfrac{1}{C_s}\dfrac{ep_0 wA}{t_t}t & 0 < t < t_T \\ \dfrac{1}{C_s} ep_0 wA & t > t_T \end{array} \right\} \quad for\ RC_s >> t_T \tag{4.6-a}$$

The V-mode signal may be approximately obtained by integrating the equation (4.5), given for I-mode signal:

$$v(t) \approx \frac{1}{C_s}\int_0^\infty i(t)dt \tag{4.6-b}$$

Thus during the transport of the photo-generated charges inside the sample the signal increases linearly with time. After the charges reach opposite electrode, the signal v(t) keeps a constant value depending on the total injected charge. Thus the V-mode signal is generally preferred to measure the number of total injected charge, this is why it is called also as *charge transient signal.*

As for the I-mode technique, it is preferred for calculating the transit time of the carriers and then the carrier mobility.

The discussion of carrier motion inside the specimen does not include so far the high density of localized states distributed in the amorphous material as previously discussed. Thus the assumption of constant density of mobile charge carriers during the motion is not valid. Instead the time dependence of the carrier density inside the specimen should be taken into account for the amorphous materials. During the motion, the carriers drifting across the sample may be captured by these traps and then they are prevented from contributing to the

transport for a certain period of time. Thus the number of mobile charge carriers decreases as the charge sheet travels across the sample, leading to the decay of the photocurrent signal.

To find the modifications for both I-mode and V-mode signals, it is suitable to assume a set of localized states at discrete energy levels with mean capture and release time τ_c and τ_r respectively. The mean capture (or mean trapping) time τ_c is the average duration a charge carrier is free to move without being trapped, while the mean release time τ_r is the mean time that the charge carrier stays at rest within the trap. However, if the transit time t_T of the carriers is significantly lower than the mean release time τ_r so the number of charge carriers that return back to the transport band after they have captured by localized states is negligible. Then ,the number of charge carriers decreases exponentially as the optical charge sheet drifts across the sample; in turn, this event affects the induced photocurrent. Thus the expression given in the equation (4.4) is modified to an exponential form as follows [41]:

$$i_{ph}(t) = \frac{ep_0 wA}{t_T} \exp\left(-\frac{t}{\tau_c}\right) \tag{4.7}$$

Then by using (4.5) the I-mode signal can be written as:

$$v(t) = \begin{cases} R\dfrac{ep_0 wA}{t_T} \exp\left(-\dfrac{t}{\tau_c}\right) & 0 < t < t_T \\ 0 & t > t_T \end{cases} \tag{4.8}$$

Either integrating (4.8) or using (4.6-a) the V-mode signal can be obtained as [39,42]:

$$v(t) = \begin{cases} \dfrac{ep_0 wA\tau_c}{C_s t_T}\left(1-\exp\left(-\dfrac{t}{\tau_c}\right)\right) & 0 < t < t_T \\ \dfrac{ep_0 wA\tau_c}{C_s t_T}\left(1-\exp\left(-\dfrac{t_T}{\tau_c}\right)\right) & t > t_T \end{cases} \tag{4.9}$$

The effect of trapping, described so far is depicted in figure 4.4 below for both I-mode and V-mode signals.

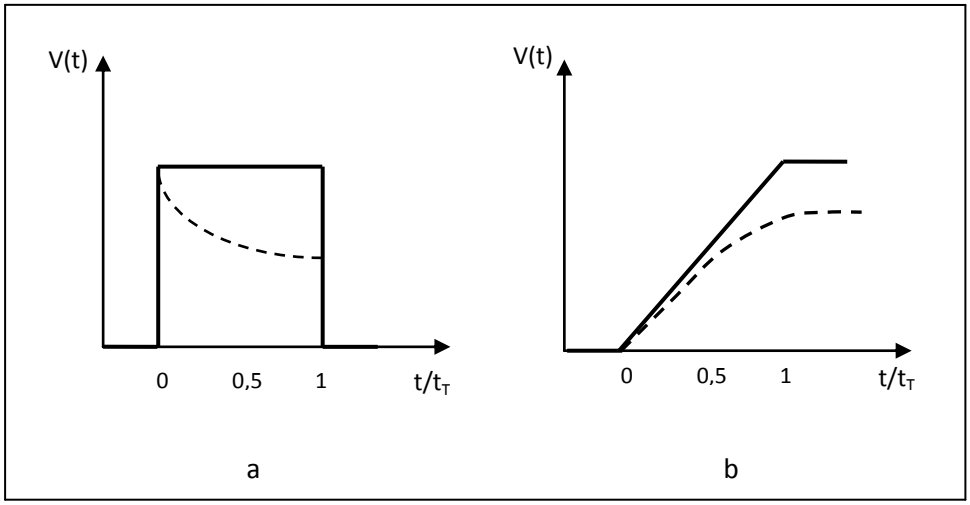

Figure 4.4: (a) I-mode signal. (b) V-mode signal. Solid lines represent trap free media where τ_c is comparable with t_T, and the dashed lines represent signals for a sample with single discrete trapping level where $\tau_c >> t_T$.

4.3 Transient Trap Limited Transport Theory:

The high concentration of localized states within the mobility gap which are defined as trapping centers for free carriers, have considerable effect on transport mechanism. The effect of the localized states will be analyzed for mono-energetic trap distribution for simplicity.

4.3.1 Mono-energetic Trap Distribution:

Considering exclusively the hole transport, the continuity equation supplies the rate of change in the concentration of holes that is present in the slice of thickness dx between the vertical planes at the positions x and x+dx :

$$\frac{\partial p(x,t)}{\partial t} = -\frac{1}{e}\frac{\partial j(x,t)}{\partial x} - \frac{\partial p_t(x,t)}{\partial t} \qquad (4.10)$$

Here $p(x,t)$ is the concentration of free holes within the slice at the time t, j(x,t)/q is the hole flux in the sample, $p_t(x,t)$ is the concentration of trapped holes by the localized centers within the given slice.

Current density, $j(x,t)$, consists of the addition of two different mechanisms: drift current and diffusion current. The drift current density for holes originated from the motion of holes due to the applied electric field and defined as:

$$j_c(x,t) = q\mu_{0p}\, p(x,t)F(x,t) \tag{4.11}$$

The diffusion current density is resulted from the spatial difference in the concentration of free holes and given by:

$$j_d(x,t) = -qD_p \frac{\partial p(x,t)}{\partial x} \tag{4.12}$$

Here D_p is the hole diffusion coefficient. Then equation (4.10) can be written as:

$$\frac{\partial p(x,t)}{\partial t} = -\mu_{0p}F(x,t)\frac{\partial p(x,t)}{\partial x} - \mu_{0P}\, p(x,t)\frac{\partial F(x,t)}{\partial x} + D_p \frac{\partial^2 p(x,t)}{\partial x^2} - \frac{\partial p_t(x,t)}{\partial t} \tag{4.13-a}$$

The equation (4.13-a) is known as the one dimensional continuity equation for holes and a similar expression can be obtained for electrons. Then the one dimensional continuity equation for electrons can be written as:

$$\frac{\partial n(x,t)}{\partial t} = \mu_{0n}F(x,t)\frac{\partial n(x,t)}{\partial x}\, \mu_{0n}n(x,t)\frac{\partial F(x,t)}{\partial x} + D_n \frac{\partial^2 n(x,t)}{\partial x^2} - \frac{\partial n_t(x,t)}{\partial t} \tag{4.13-b}$$

$\frac{\partial p_t(x,t)}{\partial t}$ and $\frac{\partial n_t(x,t)}{\partial t}$ may be considered as the net trapping rates for holes and electrons respectively. They can be evaluated by taking the difference in the instantaneous capture and reemission rates of traps for corresponding charge carrier, e.g., for holes:

$$\frac{\partial p_t(x,t)}{\partial t} = \frac{p(x,t)}{\tau_c} - \frac{p_t(x,t)}{\tau_r} \tag{4.14}$$

where τ_c and τ_r are capture and release times for holes.

Some assumptions are required to simplify the above continuity equation. If small signal conditions are satisfied, the electric field, $F(x,t)$, may be assumed uniform inside the sample at any time and the term, $\frac{\partial F(x,t)}{\partial x}$, in the (4.13-a) can be ignored. For further simplification one can assume that the diffusion current is negligible.

The continuity equation (4.13-a) and the rate equation (4.14) can be solved for hole transport considering the following boundary conditions:

- At the time t=0 the distribution of generated holes by the incident radiation pulse can be approximated by a delta function with $N_0 \equiv p_0 wA$ [39,40]:

$$p(x,0) = N_0 \delta(x,0) \tag{4.15}$$

- The initial concentration of the occupied localized states is assumed to be zero:

$$p_t(x,0) = 0 \qquad for \qquad x > 0 \tag{4.16}$$

- The generated holes drift inside the sample until they reach the collection electrode. Thus beyond the sample length the concentration of holes is taken as zero:

$$p(x,t) = 0 \qquad for \qquad x > L \tag{4.17}$$

- Similarly the concentration of trapped holes is considered as zero outside the sample.

An expression for the free hole charge density can be evaluated by using Laplace transform techniques [39, 40] as:

$$p(x,t) = \frac{N_0}{\mu_0 F}\exp\left(-\frac{z}{\tau_c}\right)\delta(t-z) + \frac{N_0}{\mu_0 F}\exp\left(-\frac{z}{\tau_c}-\frac{(t-z)}{\tau_r}\right)\frac{\xi}{2}\frac{I_1(\xi)}{(t-z)}U(t-z) \tag{4.18}$$

Here $z = x/\mu_0 F$, $I_1(\xi)$ =first order hyperbolic Bessel function, $U(x)$ =unit step function, and $\xi = \frac{2\sqrt{\tau_c z(t-z)/\tau_r}}{\tau_c}$. This solution consists of the sum of two

parts. The first part, in which the delta function, $\delta(x)$, is involved, indicates the density of charge carriers remaining in the injected hole packet as it drifts across the sample without suffering any delay due to the trapping. From the first part it is obvious to see that the concentration of charge carriers decreases as $\exp(-\frac{z}{\tau_c})$ throughout the sample.

The second part of the solution is associated with the carriers undergoing at least one capture/release cycle during the charge sheet transfer across the sample and then these carriers lag behind the original charge packet. In other words, these carriers suffering capture/release events reach the opposite electrode at a time longer then the transit time t_T of the original charge packet. The contribution of these charge carriers to the induced photocurrent will be later than the transit time t_T as the transient current. The transient current can be evaluated for two limiting cases: low field and high field.

4.3.1.1 Low Fields:

The main assumptions for low field condition is that the transit time of the carriers are much more larger than their capture time; moreover the release time of trapped carriers is comparable to the transit time, i.e. $\tau_c << L/\mu_0 F \approx \tau_r$ .Since the release time and transit time are comparable, one can assume that the time derivative of the free carrier density may be taken as zero (over the time interval approximately equal to the transit time) in the equation (4.13-a) and (4.14). Using the rate equation (2.14) for holes and applying the principle of charge conservation, one can able to write the number of free charge carriers in terms of the total injected charge, $N_0 \equiv p_0 wA$, as follows [41]:

$$N = N_0 \frac{\tau_c}{\tau_c + \tau_r} \tag{4.19}$$

Thus the photocurrent for the I-mode transient signal can be written by substituting (4.19) in (4.4) as:

$$i_{ph} = \frac{qN_0\mu_0 F}{L}\left(\frac{\tau_c}{\tau_c+\tau_r}\right) \quad = \quad \frac{qN_0\mu}{L}F \quad \text{for} \quad \tau_c < t < \frac{\tau_c+\tau_r}{\tau_c}\frac{L}{\mu_0 F} \qquad (4.20)$$

Where

$$\mu \equiv \mu_0 \frac{\tau_c}{\tau_c+\tau_r} \qquad (4.21)$$

In the above equation (2.34) the transit time, $\frac{L}{\mu_0 F}$ obtained for trap-free I-mode transient signal, increased by a factor of $\frac{\tau_c+\tau_r}{\tau_c}$. Besides, the effective mobility of the carriers is reduced due to successive trapping events. This type of motion is called as trap-controlled transport and the term $\frac{\tau_c+\tau_r}{\tau_c}$ is known as trap-controlled transport factor.

4.3.1.2 High Fields:

As it is mentioned before the transit time of the carriers related to the applied electric field as $\frac{L}{\mu_0 F}$. This expression points out that the transit time t_T of the charge carriers may become small enough such that $L/\mu_o F << \tau_c$. It is convenient to analyze the photocurrent signal in two different time regimes [41].

During the first period where $0 < t < \frac{L}{\mu_0 F}$, the current expressions can be written as:

$$i_{ph}(t) = \frac{qN_0}{t_T}\left[\frac{\tau_c}{\tau_c+\tau_r} + \frac{\tau_r}{\tau_c+\tau_r}\exp\left(-\frac{\tau_c+\tau_r}{\tau_c\tau_r}t_T\right)\right] \qquad (4.22)$$

If the release of the captured carriers can be neglected by letting $\tau_r \to \infty$, the equation (4.22) can be reduced to the equation (4.7) which is the photocurrent for the case of deep trapping.

During the second period where $t > \frac{L}{\mu_0 F}$, the current expressions can be written as:

$$i_{ph}(t) = \frac{qN_0}{2}\frac{t_T}{\tau_c \tau_r}\exp\left(-\frac{t}{\tau_r}\right) \tag{4.23}$$

The last equation is derived for the times above the transit time $t_T = \frac{L}{\mu_0 F}$. Here, the detected photocurrent results from the delayed carriers that have been captured by traps and then released back to the transport band and are drifted to the collection electrode.

As a result, for the high field case, the last two equations carry out that the detected photocurrent will decay exponentially as the charge packet crosses the sample with different rate in each period such that a step change occurs at $t = L/\mu_0 F$ .In other words, at $t = L/\mu_0 F$, the majority of the carriers reaches the collection electrode without undergoing any trapping and releasing events; and beyond transit time , a relatively slow decay to zero occurs in the photocurrent since the trapped carriers are released back into the transport band and drifted to the collection electrode.

4.4 Experimental Setup for TOF:

A simple demonstration of the time of TOF experimental set up is shown in the figure 4.5. The main components of the system consist of a Nitrogen laser (VSL-337), a signal generator (Tektronix programmable signal generator, Model: PG-5110) and a digital oscilloscope (Hewlett Packard Digitizing Oscilloscope, Model: 54512B).

The laser is used to illuminate the sample by very short light pulses, a pulse generator to apply voltage bias on the sample and trigger the laser, an oscilloscope to observe photocurrent pulse transient in time. The laser produces 200 mJ light pulses of 337 nm at frequencies in between 0 and 60 Hz. The full width at half maximum of the pulses is 4 ns, which is much shorter than the transit time of charge

carriers in the sample so that the condition of obtaining relatively thin sheet of charges is fulfilled.

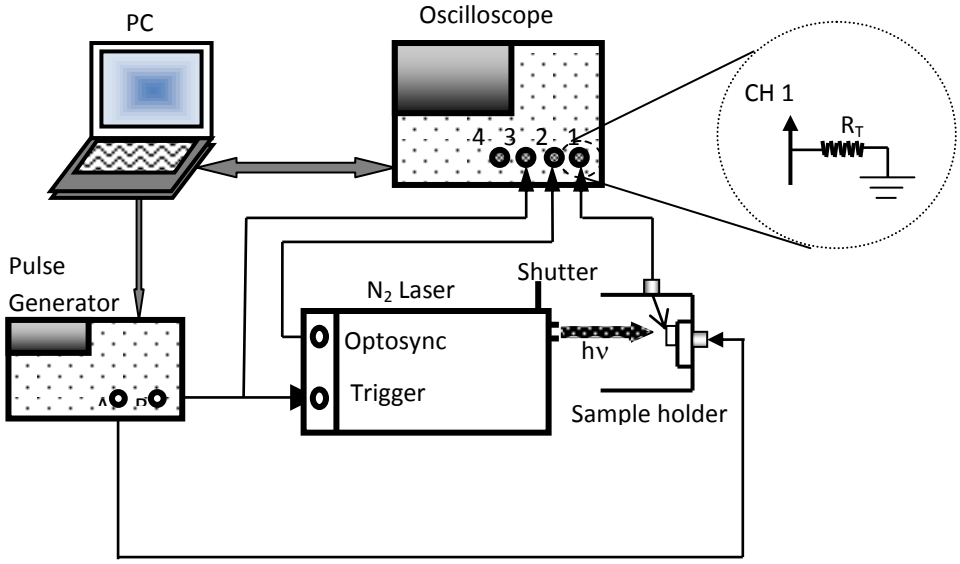

Figure 4.5: Schematic illustration of TOF experimental set up

The laser pulses can be triggered by an external voltage (Transistor Logic voltage is at 5 V when it is high state, and at 0 V when low state) with a delay time less than 10 ns. Additionally, an optosync output is supplied to produce 5 V pulses triggered by a photodiode placed inside the laser in order to synchronize other instruments for transient optoelectronic applications. The TTL signal for triggering purpose and bias voltage are supplied by a computer controlled pulse generator, which has two outputs with sharp pulse edges down to 6 ns. The two outputs A and B generate voltage pulses whose delay time, pulse width, edge slopes and voltages are independently controlled at common frequency. Therefore, the outputs A and B are used to apply voltage to the sample and to the trigger input of the laser, respectively. The pulses used in the setup, and resultant transient signal are measured and monitored by the four cannel digital oscilloscope which can measure time interval down to 2 ps (pico seconds). The inputs of the scope have a capacitance of 7 pF, causing time constant of 350 ps for 50 Ω input, typically.

In the experimental procedure, a predetermined pulse or DC voltage is applied to the sample from the channel "A" of the signal generator, shown in the

figure 4.6. Then, the other electrode of the sample is connected to “channel 1” of the oscilloscope to monitor and transfer transient photocurrent signal to pc. Another 5 ms voltage pulse of 5 V (TTL signal) with a small delay time 1 to 10 μs with respect to the signal from channel “A” is generated by the channel “B” and applied to both laser-trigger-input and “channel 3” of the oscilloscope. The laser trigger input enables to activate the laser pulse within a delay time of about 50 ns. This drawback is removed by the laser optosync-output, connected to the channel 2 of the oscilloscope to activate the instrument simultaneously with laser. Whereas less then 50 ns delay is observed between the optosync signal and the optical output signal of the laser.

Timing diagram of the signals used in this setup is given in figure 4.6. When the pulse generator is triggered, Sample is immediately biased by the signal generated at the output A, shown in the figure 4.6. After a short delay about 500 ns, A TTL pulse generated at the output B is applied to the trigger input of the laser, the signal 2 in the figure 4.6. Then, the laser produces a light flash within 50 ns delay time, and a 5 V TTL signal at the optosync output, signals 3 and 4 in the figure 4.6, respectively. Finally, a photocurrent transient signal is produced across the sample, signal 5 in figure 4.6. The resultant signals are monitored by the oscilloscope and recorded to a PC with the suitable software via IEEE488 protocol.

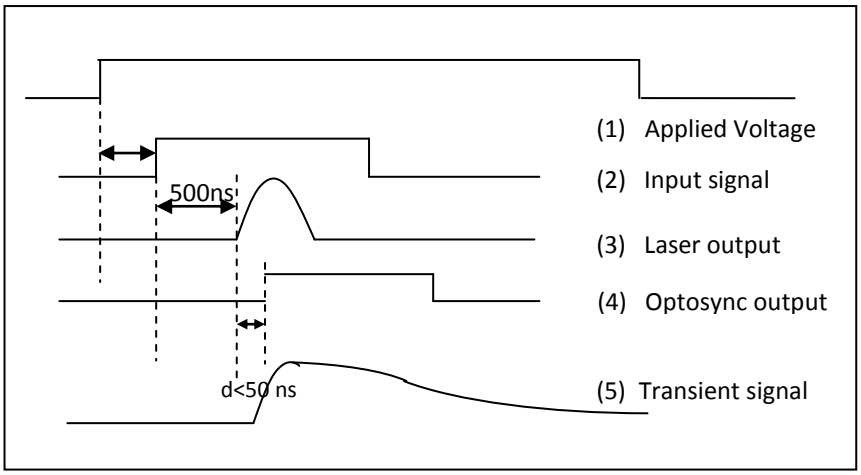

Figure 4.6: The delay times of the input signal from channel “B” of the Tektronix PG-5110 signal generator, the laser optical output and the optosync output of the laser when the trigger input of the VSL-337 air-cooled nitrogen laser is activated.

The experiment is held under computer control by a program using Labview programming language via IEEE protocol between the computer and instruments. The flowchart of the program is given in figure 4.7. The program initially puts the scope and signal generator is ready for measurement and waits for user response to trigger the signal generator. In this step, a suitable terminator resistance should be connected to the input of the channel 1 of the oscilloscope in order to change time constant of the circuit; since input of the scope has capacitance and stray capacitance of cables, the gain resistance of the input amplifier is limited especially for fast transients. This limits the resolution of the measurement enormously, even at the times longer than around 100 times the time constant the signal is completely lost within background noise. Therefore, higher value of resistance is necessary for longer transients in order to increase gain of the preamplifier. After placing the suitable terminator resistance, the measurement starts by pressing "M" key. When the "M" is pressed, "A" channel of signal generator immediately sends the adjusted signal to the sample, signal 1 in figure 4.6. After a while, depending on the delay time of the channel "B", it sends a TTL pulse to both the trigger input of the laser and "channel 3" of the oscilloscope, signal 2 in figure 4.6. Thus laser is triggered by an external signal and the optical output of the laser (λ=337 nm and pulse width = 10 ns) is incident to the sample with 500ns delay, see figure 4.6. The oscilloscope can be triggered either from "channel 2" or "channel 3", shown in figure 4.5. Former receives signal from optosync output of the laser and latter receives directly from "B" channel of signal generator. Considering the greater delay between the trigger activation and the pulse generation (500ns) relative to the delay between optosync signal and the optical output signal of the laser (50 ns), "channel 2" of oscilloscope is determined as trigger source. The resulted transient photocurrent signal of the sample is collected by "channel 1" as a voltage transient on the terminator resistance, shown in figure 4.5. This signal is digitized by the oscilloscope and transferred to the PC. If the displayed signal is not appropriate, the program has a choice to go back to the trigger step to measure the transient again, depicted in figure 4.7. Otherwise, the voltage data is converted to current by dividing the resistance and saved to a file. In order to change the time span of the transient, the program goes back to the second step, as shown in the flowchart,

figure 4.7. To obtain a background signal, closing the shutter of the laser and repeating the same procedure is adequate and resulted signal is saved as background for that time interval. As a result, the difference between the transient signal and the background signal yields the transient photocurrent. After measuring all transients, the program is stopped. Further analyses of transient data are accomplished by software like Matlab or Excel.

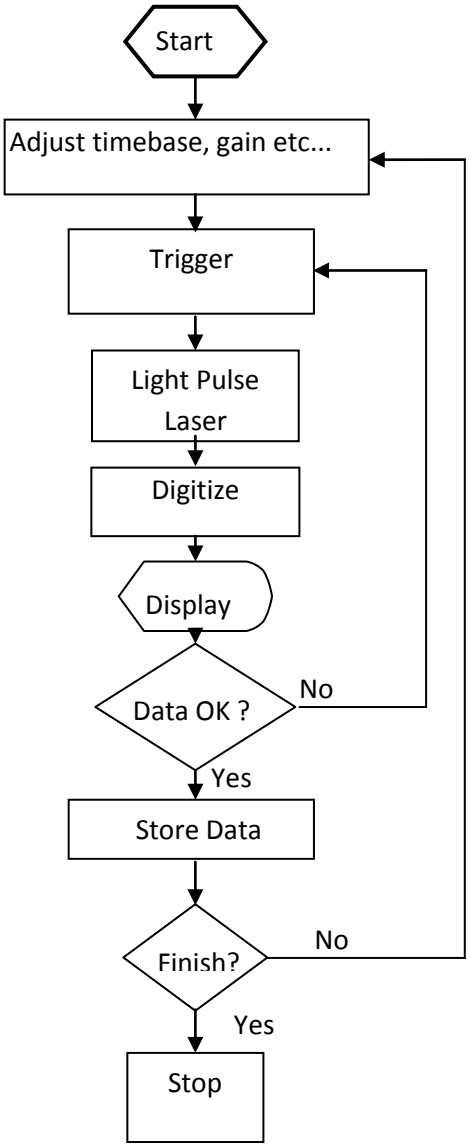

Figure 4.7: Flowchart of the program used for measurement setup.

The measured voltage signals and current signals are shown in figures 4.8 and 4.9, respectively. It is clearly seen that when the time constant of the measurement circuit is low, the signal has very low sensitivity and drops to the noise level without giving information about hopping currents inside tail states due to the lower gain of the preamplifier. Increasing the gain of preamplifier increases the time constant of the circuit and hence it gives valuable information for longer time intervals. Therefore, a single photocurrent transient signal can be composed of different transients obtained by different time constants, shown in figure 4.10.

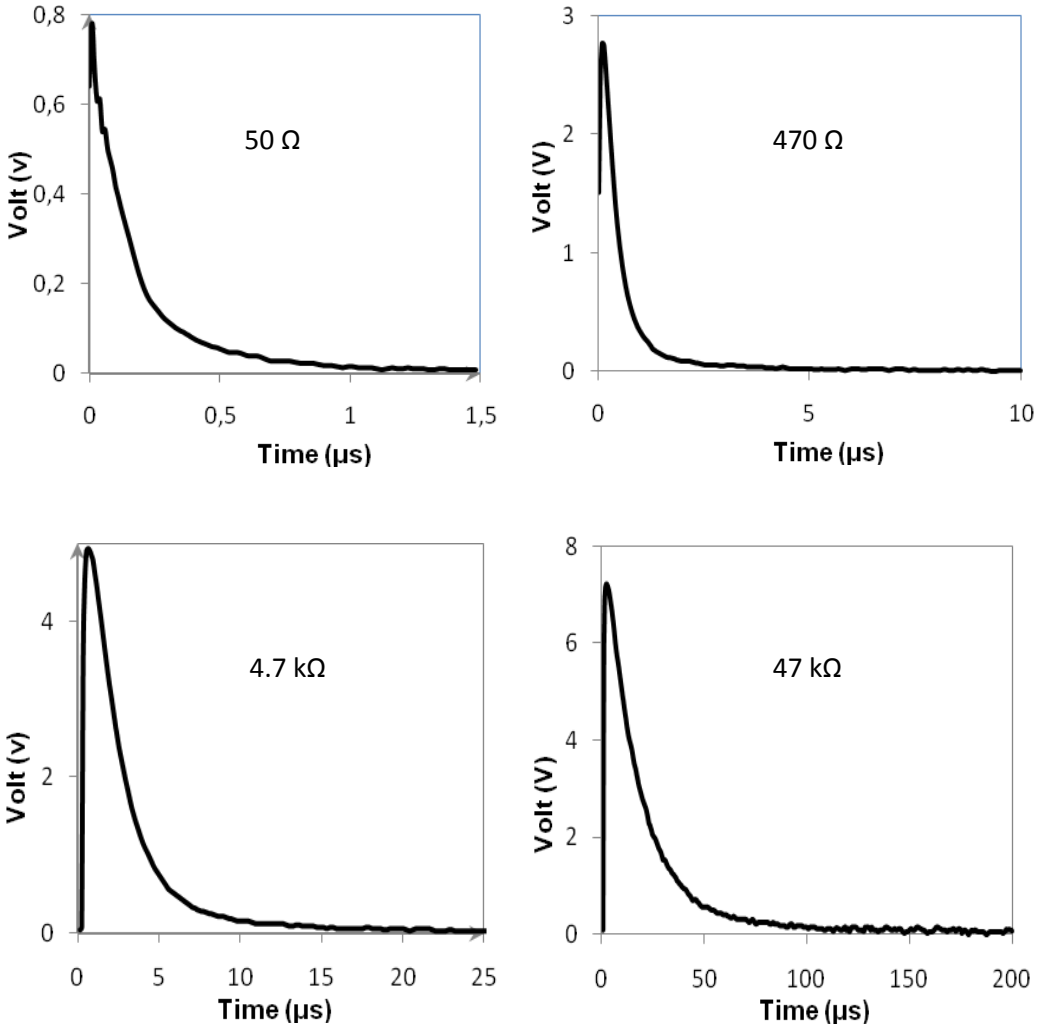

Figure 4.8: Typical voltage transients as measured by the oscilloscope.

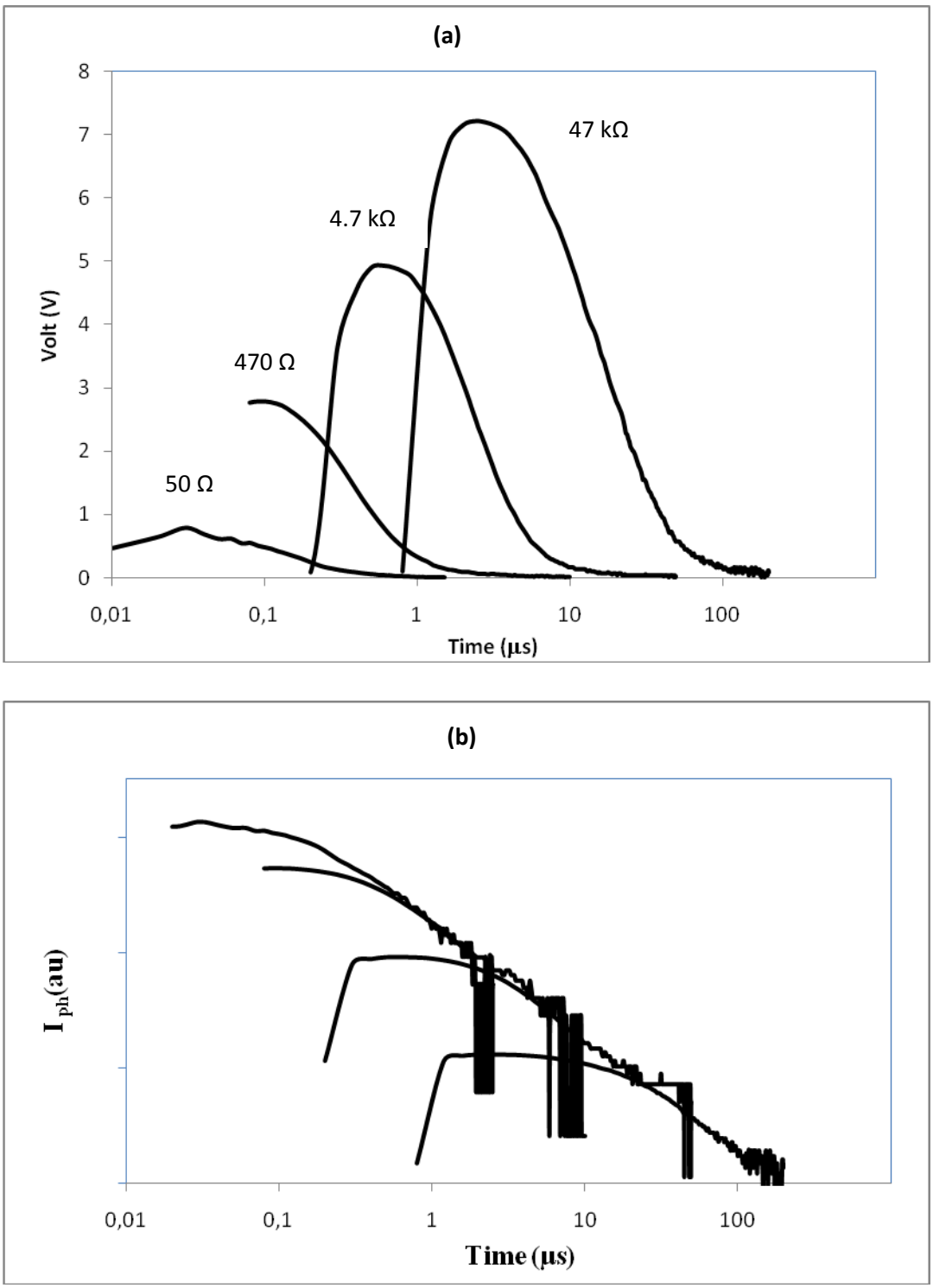

Figure 4.9: Typical (a) voltage (semi log graph) and (b) current (log-log graph) transients. The current transients in (b) are obtained by division of voltage to corresponding terminator resistance.

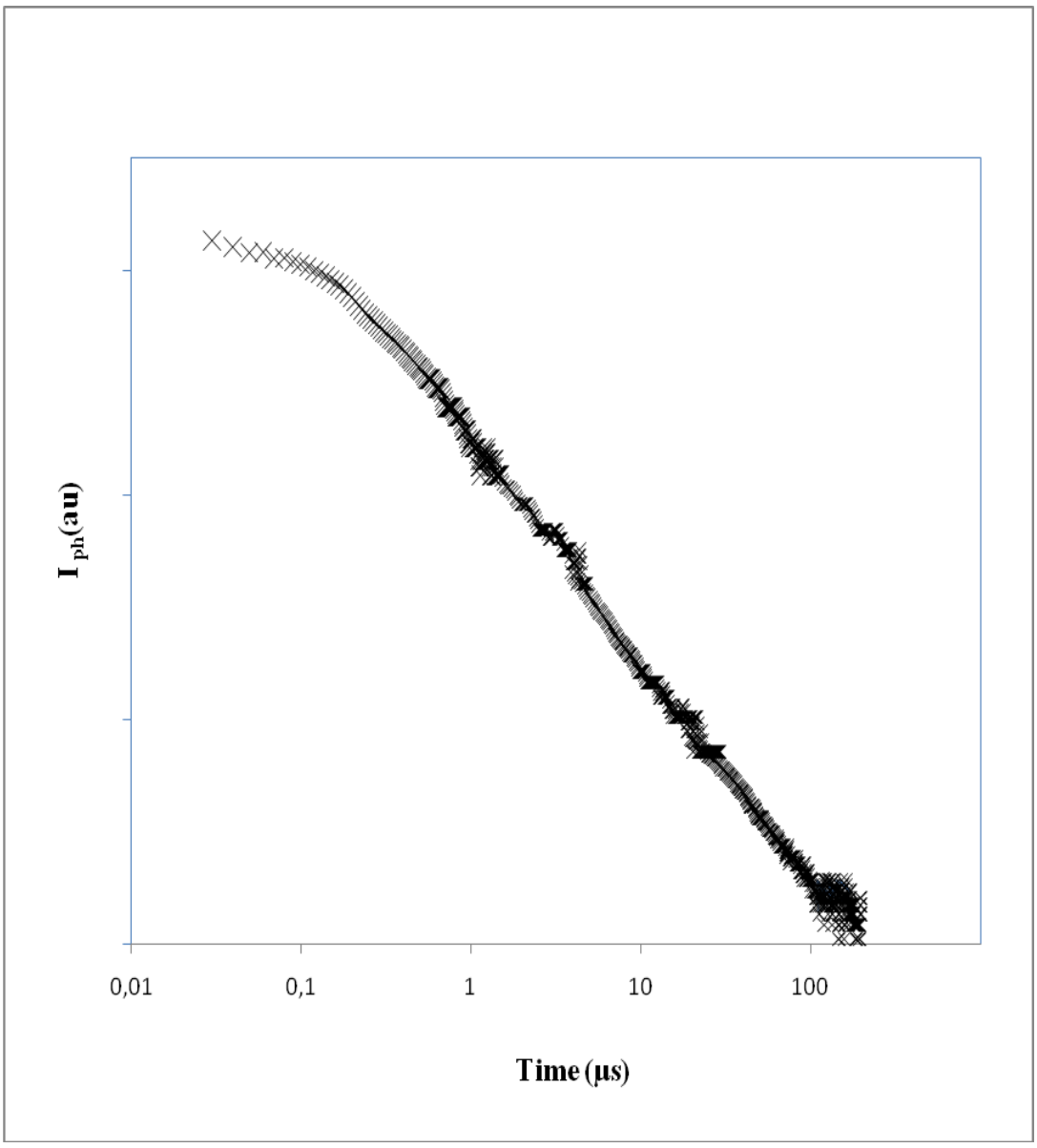

Figure 4.10: The final form of photocurrent transient.

CHAPTER 5

CONSTANT PHOTOCURRENT METHOD (CPM)

5.1 Theory of Carrier Generation:

Generation of free electrons and holes in conduction and valance bands can be obtained by optical ways as we have discussed in TOF technique. The generation rates of the free carriers depend on the parameters cited below.

- The number of incident photon (Photon flux).
- Reflection at the semiconductor surface.
- The distance of the trapped carriers from the surface of the sample.
- And the quantum efficiency of incident light.

Then the generation rate can be written as [43]

$$G = \phi(h\nu)d^{-1}n(h\nu)[1-R(h\nu)]\{1-\exp(-\alpha(h\nu)d)\} \tag{5.1}$$

Where d is the thickness of the sample, R is the reflectance at the film surface and n is the quantum efficiency. In the low absorption regime, the dependency of n and R on photon energy is negligible. Then, for αd << 1 the above equation can be expressed as:

$$G = n(1-R)\alpha(h\nu)\phi(h\nu) \tag{5.2}$$

The generation rate has two parts; electron generation and hole generation. However for Intrinsic and n doped samples it is usually accepted as the electron generation is dominant ($G \approx G_n$).

Under steady state conditions the continuity equations for electrons tells that the generation rate is equal to the recombination rate.

$$G = R_n = \frac{(n-n_0)}{\tau_n} \tag{5.3}$$

Where τ_n is the free electron life time, n and n_o are the electron concentrations before and after the illumination respectively.

As it is discussed in the previous sections the photoconductivity can be written for n type materials as fallows:

$$\sigma_{ph} = q\mu_n(n - n_0) \tag{5.4}$$

Using equations (5.3) and (5.4), one can able to obtain the relationship between the photoconductivity and generation rate of the free carriers as:

$$G = \frac{\sigma_{ph}}{q\mu_n\tau_n} \tag{5.5}$$

It is obvious from equation (5.5) that, to satisfy the constant generation rate which is a crucial requirement for CPM bring out the condition that free electron life time should be constant (τ_n =constant). However for the case of a-Si:H under sub-gap illumination the occupancy of gap states may be changed, thus the assumption of constant free carrier life time and constant generation rate does not hold anymore. Hence the possible generation mechanisms and thermal equilibrium of dangling bond states should be analyzed. In order to simplify the thermal possible processes, one can assume single dangling bond located at energy E with a density N_D per unit volume. As it is discussed in previous chapters due to effective correlation energy the dangling bond states exhibits there possible state; D^+, D^0 and D^- (Amphotericlike state). Consider the midgap states can communicate both conduction and valance band. As a result there will be eight transitions and U_i is the number of transition per unit volume per unit time for each. These thermal equilibrium processes are depicted in figure 5.1.

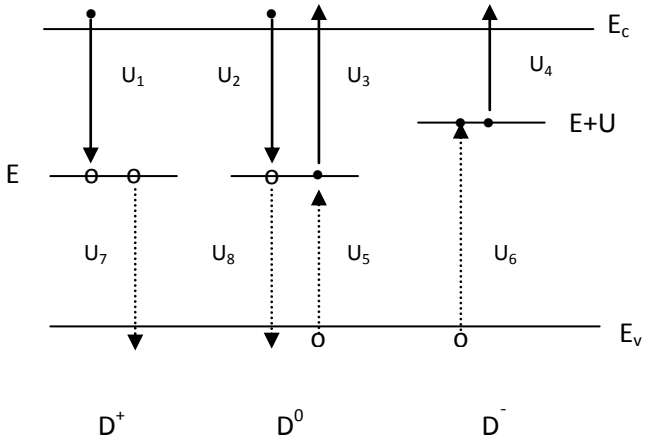

Figure 5.1: Schematic representations of possible thermal transitions for positively correlated dangling bonds. Dots (•) and open circles (o) represents electrons and holes, respectively.

Applying Shockley-Read-Hole Statistics to amphotericlike states, Ui can be evaluated as a function of emission and capture parameters as fallows:

$$\begin{aligned} U_1 &= nN_D f^+ c_n^+ & U_5 &= N_D f^0 p c_p^0 \\ U_2 &= nN_D f^0 c_n^0 & U_6 &= N_D f^- p c_p^- \\ U_3 &= N_D f^0 e_n^0 & U_7 &= N_D f^+ e_p^+ \\ U_4 &= N_D f^- e_n^- & U_8 &= N_D f^0 e_p^0 \end{aligned} \tag{5.6}$$

Where n and p is the density of free electrons and holes respectively, f^+, f^0 and f^- are the probabilities of finding corresponding dangling bond center, c_n^0 and c_n^+ are the rates for electron capture in unit volume per unit time by D^0 and D^+. Similarly c_p^0 and c_p^- are the hole capture rates associated with D^0 and D^- states. e_n^0 and e_n^- rates of electron emission from D^0 and D^- states. Finally, the hole emission from D^0 and D^+ states are given as e_p^0 and e_p^+ respectively.

If the thermodynamic equilibrium is sustained, the detailed balance conditions should be satisfied, then $U_1=U_3$, $U_2=U_4$, $U_5=U_7$ and $U_6=U_8$. Then, the emission rates can be expressed in terms of capture rates and occupation functions:

$$e_n^0 = n_0 f_0^+\left(\frac{c_n^+}{f_0^0}\right) \qquad e_n^- = n_0 f_0^0\left(\frac{c_n^0}{f_0^-}\right)$$
$$e_p^0 = p_0 f_0^-\left(\frac{c_p^-}{f_0^0}\right) \qquad e_p^+ = p_0 f_0^0\left(\frac{c_p^0}{f_0^+}\right) \tag{5.7}$$

In equation (5.7) "0" subscript used for denoting thermal equilibrium. However under sub-gap illumination even if the thermodynamic equilibrium does not hold it is considerable to assume the emission and capture rates remain same.

In addition to these thermal transitions, there will be some optical transitions between dangling bond states and valance and conduction band with the effect of incident photon flux. The possible optical transitions are depicted in figure 5.2.

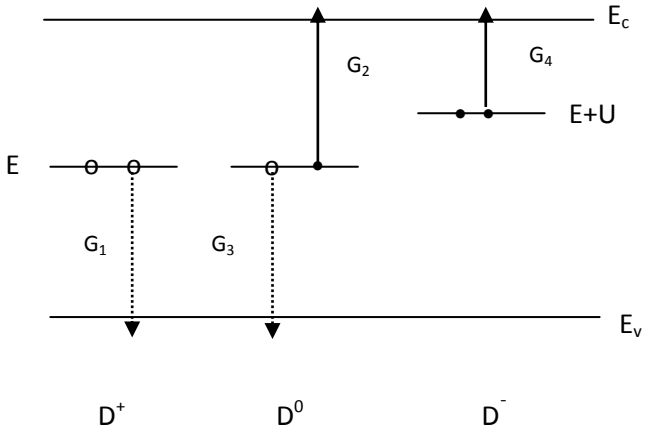

Figure-5.2: Schematic representation of the sub-gap optical transitions for positively correlated dangling bonds. Dots (•) and open circles (o) represents electrons and holes respectively.

The generation rates G_i can be evaluated as [44]:

$$G_i = \alpha_i \phi \tag{5.8}$$

Where Φ is the effective flux and α is the optical absorption coefficient corresponding to the i'th process. Components of the total absorption coefficient are given by a convolution of the DOS [45, 46].

$$\alpha_i = \frac{C}{h\upsilon}\int_{-\infty}^{\infty} N_{in}(\varepsilon - h\upsilon) f_{in}(\varepsilon - h\upsilon) N_{fin}(\varepsilon)[1 - f_{fin}(\varepsilon)]d\varepsilon \tag{5.9}$$

Where C is a constant involving the matrix element of the transition, and are the density of initial and final states, and are the occupation function of initial and final states respectively, Then, one can write the generation rates of the optical sub-gap transitions represented in figure 5.2 by using equations (5.8) and (5.9) as:

$$\begin{aligned} G_1(h\upsilon) &= \phi \frac{C}{h\upsilon} N_D(E) f^+(E) N_v(E - h\upsilon) \\ G_2(h\upsilon) &= \phi \frac{C}{h\upsilon} N_D(E) f^0(E) N_c(E + h\upsilon) \\ G_3(h\upsilon) &= \phi \frac{C}{h\upsilon} N_D(E) f^0(E) N_v(E - h\upsilon) \\ G_4(h\upsilon) &= \phi \frac{C}{h\upsilon} N_D(E) f^-(E) N_c(E + U + h\upsilon) \end{aligned} \tag{5.10}$$

Where N_v and N_c are the density of states in the valance band and conduction band. The valance band is assumed to be completely occupied, while the conduction band is totally unoccupied. Under steady state illumination, the occupation function of each dangling bond state can be evaluated by using the following set of equations:

$$\begin{aligned} &\frac{d[D^+]}{dt} = U_3 + U_5 + G_2 - U_1 - U_7 - G_1 = 0 \\ &\frac{d[D^-]}{dt} = U_2 + U_8 + G_3 - U_4 - U_6 - G_4 = 0 \\ &f^+ + f^0 + f^- = 1 \end{aligned} \tag{5.11}$$

Then, occupation functions can be expressed as [43]:

$$\begin{aligned} f^0 &= \frac{CC_1 * CC_3}{CC_1 * CC_3 + CC_2 * CC_3 + CC_1 * CC_4} \\ f^+ &= \frac{CC_2 * CC_3}{CC_1 * CC_3 + CC_2 * CC_3 + CC_1 * CC_4} \\ f^- &= \frac{CC_1 * CC_4}{CC_1 * CC_3 + CC_2 * CC_3 + CC_1 * CC_4} \end{aligned} \tag{5.12}$$

where

$$
\begin{aligned}
CC_1 &= nc_n^+ + e_p^+ + \phi\, MN_v(E - h\upsilon) \\
CC_2 &= e_n^0 + pc_p^0 + \phi\, MN_c(E + h\upsilon) \\
CC_3 &= pc_p^- + e_n^- + \phi\, MN_c(E + U + h\upsilon) \\
CC_2 &= e_p^0 + nc_n^0 + \phi\, MN_v(E - h\upsilon)
\end{aligned}
\tag{5.13}
$$

The discussion so far does not involve the band tail transitions. The possible optical and thermal transitions are shown in figure 5.3.

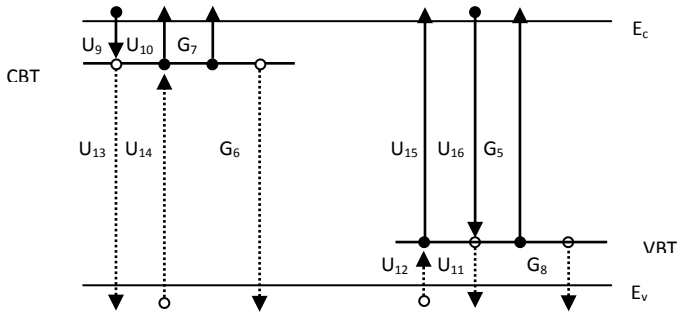

Figure 5.3: Schematic representation of the thermal (U_i) and optical (G_i) transitions between the tail states and the extended bands.

Similarly the occupation functions f^{CBT} for electrons in conduction band tail and f^{VBT} for holes in valance band tail can be expressed as [43]:

$$
\begin{aligned}
f^{CBT} &= \frac{e_p^c + nc_n^c + \phi\, MN_v(E - h\upsilon)}{e_n^c + e_p^c + nc_n^c + pc_p^c + \phi\, MN_v(E - h\upsilon) + \phi\, MN_c(E + h\upsilon)} \\
f^{CBT} &= \frac{e_n^v + pc_p^v + \phi\, MN_c(E + h\upsilon)}{e_n^v + e_p^v + nc_n^v + pc_p^v + \phi\, MN_v(E - h\upsilon) + \phi\, MN_c(E + h\upsilon)}
\end{aligned}
\tag{5.14}
$$

where $c_{n(p)}^c$ and $c_{n(p)}^v$ are the rates for electron (hole) capture by conduction and valance band tail states, respectively; and $e_{n(p)}^c$ and $e_{n(p)}^v$ are the rates for electron (hole) emission from conduction and valance band tail states, respectively.

5.2 Principles of Constant Photocurrent Method(CPM):

CPM is widely used to analyze the density of state distribution. The most significant advantage of using CPM method is that, it is surface insensitive and able to measure charged and neutral defect densities.

As it is discussed in previous sections the current density resulted from the photo-induced carriers is depend on the electric field as fallows:

$$J = \sigma_{ph} F \tag{5.15}$$

The generation rate can be evaluated simply by substituting equation (5.15) into equation (5.5) as:

$$G = \frac{J}{Fq\mu_n \tau_n} \tag{5.16}$$

Considering the assumption that the electron generation is dominant, then the generation rate can be written as:

$$G = G_2 + G_4 + G_7 + G_5 \tag{5.17}$$

Equation (5.17) states that the generation rate which is source of photocurrent is the sum of transitions G_2 , G_4 , G_5 , G_7 represented in the figures 5.2 and 5.3 because the recombination is not allowed in the intrinsic region.

The relation between the generation rate and the photocurrent is given in equation (5.16). Using this relation one can easily say that since the photocurrent changes with wavelength of the incident photon, the generation rate also changes if the electric field is uniform and the free electron lifetime and mobility product is constant. Then, using equation (5.2) and (5.16) the absorption coefficient can be expressed as:

$$\alpha(h\upsilon) \approx \frac{J(h\upsilon)}{\phi(h\upsilon)} \tag{5.18}$$

Equation (5.18) yields a very useful technique to determine the change in the absorption coefficient simply by measuring the photocurrent at a given photon flux with energy $h\upsilon$.

The main drawback of equation (5.18) is to have material with constant $\mu\tau$, which has dependence on the localized DOS at E_F. When the photocurrent is held constant by changing the photon flux, $\phi(h\upsilon)$, this drawback is removed due to the fact that constant generation rate constitutes constant density of free charge carriers and hence the position of E_F does not move. In another word, since both G and q(J/F) in equation (5.16) are constant, one can obtain the following relation:

$$\mu_n \tau_n = \text{constant} \tag{5.19}$$

As a result, the condition of constant is satisfied by CPM technique, and hence absorption coefficient given by equation (5.18) becomes free of product as;

$$\alpha(h\upsilon) \approx \frac{1}{\phi(h\upsilon)} \tag{5.20}$$

The above equation ensures to evaluate the absorption coefficient with the help of the absorption spectra obtained from the transmission and reflection measurements and using it to calibrate the data at high photon energies.

5.3 Optoelectronic Measurement System:

The system used in this work, shown in figure 5.4, has two parts; light producing part and light detecting part. Light producing part contains a light source, a monochromator and a beam splitter. Light detecting part consists of a detector, a lock-in amplifier and an electrometer. Control of the system, necessary calculations and simulations are done by use of a PC via IEEE 488 protocol.

In our system the light beam was supplied by an illuminator (model 7340 of universal illuminator of Oriel) in which a tungsten halogen lamp is used as a light source of 120W electrical power supplied from a stabilized dc power supply (HP6342). In order to produce a monochromatic light beam, the monochromator, Oriel MS 257 was used and the scanning of the beam wavelengths was achieved by a 1200 line/mm grating, blazed at wavelength of 350nm, and rotated by the ultra rapid stepper motor drive with an oversize computer controlled worm drive that ensures high precision and stability. Higher orders of radiation (λ, 2λ, 3λ) appearing

at larger wavelengths, besides the actual radiation was eliminated by using suitable low pass filters which is transparent for the radiation at low energies and opaque for radiation of energies higher than a threshold energy. Throughout this work, silicon (cut off wavelength is 1050nm) and red filters (cut off wavelength 630nm) were placed in front of the monochromator. The wavelength range used for silicon, TFS1 84433, and red , FG07-25, filters are 1100-2000nm and 695-1100nm respectively.

The input and output slit widths of the monochromator change the bandwidth of light emerging from it as the grating lines disperse the incident light. Thus, the bandwidth may be obtained by multiplying the slit width by reciprocal lines dispersion, 3.2nm/mm. In this way, the light intensity at the output of the monochromator depends on the slit width as seen in figure 5.5. Then the slit width of the monochromator should be set by a balance between maximizing the light intensity and resolution, as the light intensity should be increased in order to obtain measurable photocurrent. However, its bandwidth should be narrow enough to differentiate the energy levels of the density of states.

The grating used in the experiment has a diffraction efficiency depending on the polarization of the radiation incident on it as seen in the figure 5.5., which means that the components of the light (s, p polarized parts) falling on the grating is reflected in different rates. Therefore, the incident radiation on the beam splitter diffracted elliptically polarized and this causes such a correlation between the reflected and transmitted parts of the light.

In order to obtain the intensity of the light falling onto the sample during the photocurrent measurements simultaneously, emerged light from the monochromator was divided into two parts by using a beam splitter, so that transmitted part falls on the detector and reflected part falls on the sample. Then by knowing the intensity of light falling on the detector (transmitted part), the intensity on the reflected part has found by a correction curve which gives the fraction of reflected over transmitted intensities from the beam splitter for used wavelength range, shown in figure 5.6.

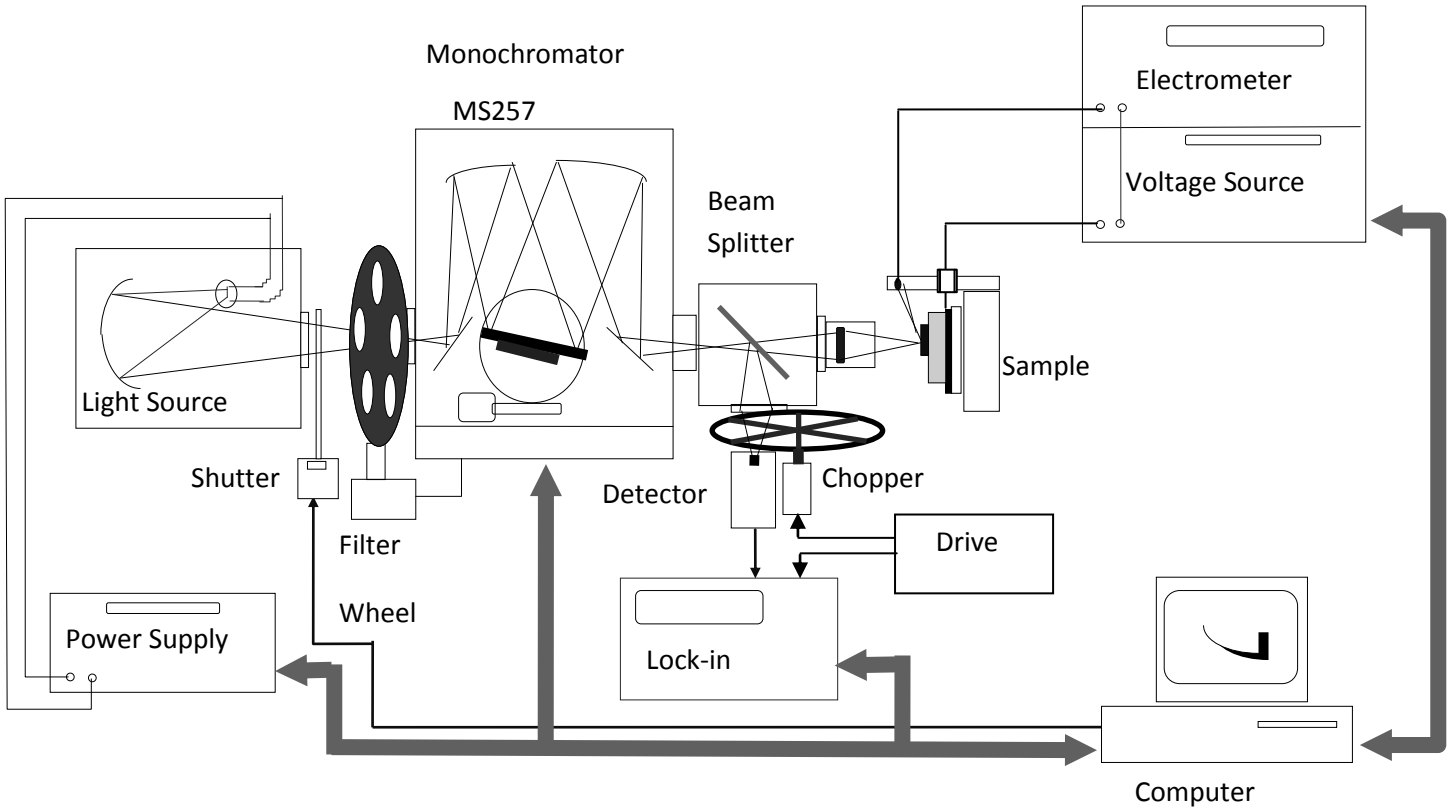

Figure 5.4: Optoelectronic measurement system

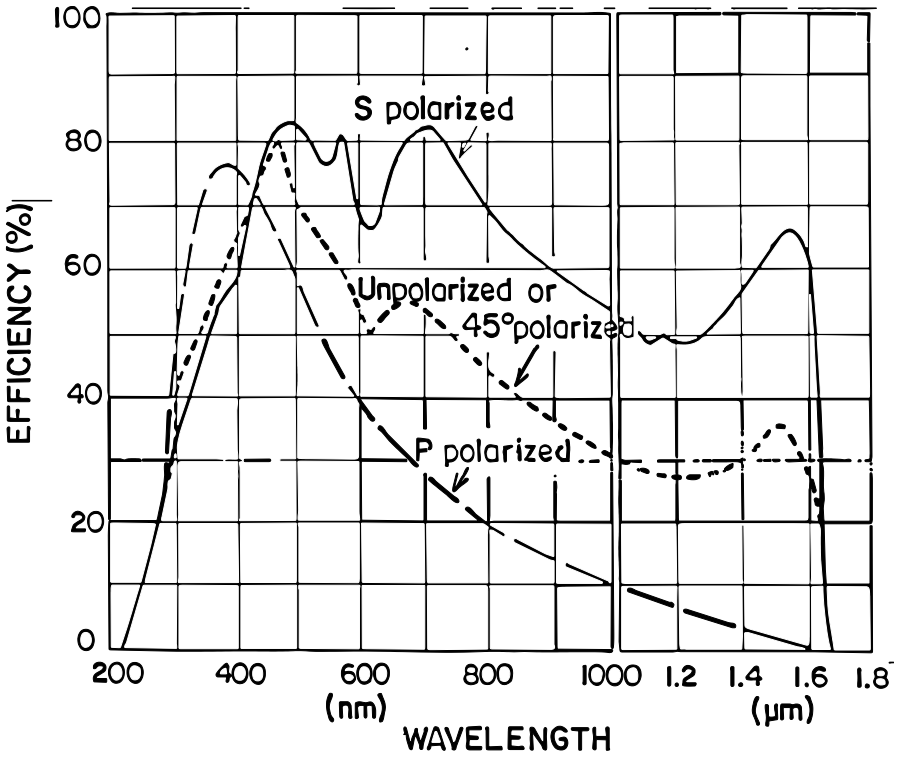

Figure 5.5: Polarization dependence of reflected light.

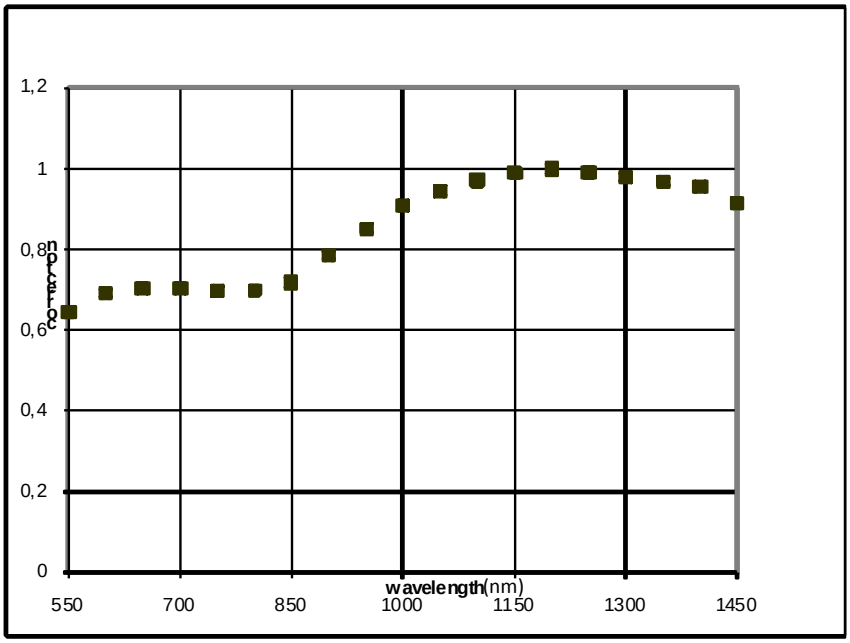

Figure 5.6: Correction curve of beam splitter.

5.4 The Software of CPM:

In this technique, as its name implies photocurrent value is adjusted to a constant value at each wavelength by changing the intensity. Constant photocurrent measurements were done under computer control by a program prepared with a graphical programming language, Labview. The software starts running by resetting the previous data values of the voltage source of the lamp, the lock in amplifier, the electrometer and the monochromator. Then, new initial values for delay time, wavelength range and the value change in the wavelength for each step are adjusted. In addition, the intensity of the light was also adjusted to the desired value by the software, having a flow chart as shown in figure 5.7. The main parts of that software can be described as:

- Shutter is closed, wavelength is set to requested value and the current passing through the film I_0 and the output of the detector Φ_0 are measured, and saved as the background measurements.

- Desired constant photocurrent value I_p is calculated by the addition of measured dark current, I_o, and expected constant photocurrent value I_{ph},

- Shutter is opened and then current I and flux Φ values that are measured in the main program are checked whether measured I is closer to I_p within and error range of ΔI_{ph}. If they are, the main loop continues and goes one step further, if not loop passes to the photocurrent loop and this loop continues until the measured photocurrent value reach to desired constant photocurrent value, I_p.

- In the loop, measured current, I is compared with the calculated I_p value, if it is less than I_p , the voltage output of the power supply is increased by ΔV, otherwise decreased by ΔV.

- Meanwhile, parameter E ($\equiv I_p$-I) is used to enable the system to remember the measured current, I, is whether higher or lower than the I_p.

- If parameter E takes the value of previous step successively, then photocurrent value still is at the same side of the I_p value therefore ΔV remains same. If not, since measured current crosses I_p, this time measurement is repeated

for a smaller step increase (or decrease) of $\Delta V/2$. This loop continues until the photocurrent reach to desired value.

- When the loop is finished, software runs as in the photocurrent case however in this case I_p and I_{ph} values are not recorded to hard disk since it is entered, known value by the user. Most important property of this software is that, value of constant photocurrent and measurement error range in it can be set to desired values.

- By subtracting the background values from the illuminated values, the photocurrent I_p and flux Φ are calculated.

- Then, above steps are repeated for every wavelength until the whole wavelength range is finished.

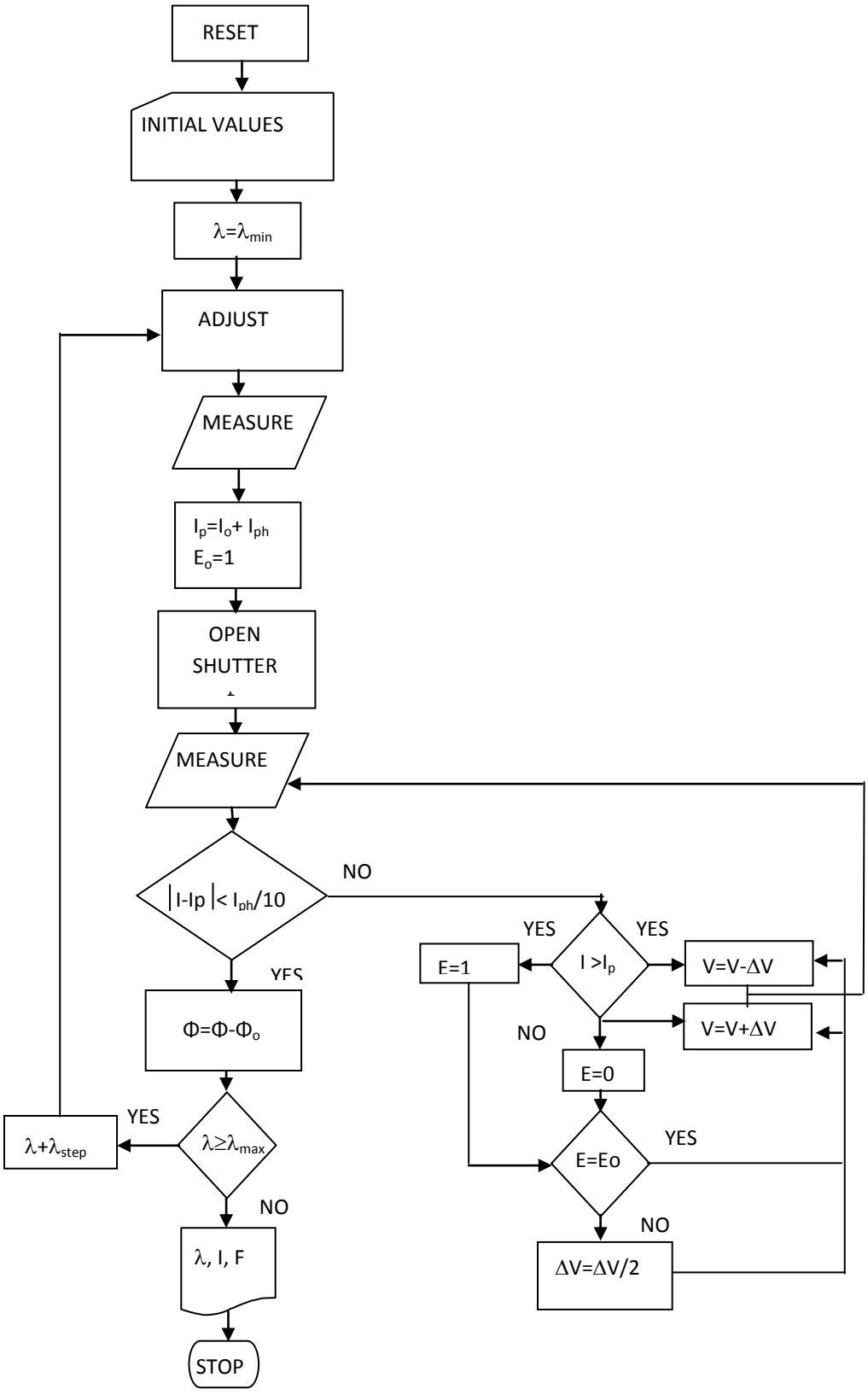

Figure 5.7: Flow chart of CPM measurements

CHAPTER 6

FABRICATION OF THE SAMPLE AND MEASUREMENTS

6.1 Cleaning:

Amorphous silicon alloy films can be deposited on different sorts of substrates for different application purposes. These are generally crystalline silicon quartz or glass slides, stainless steel, chromium, etc. In this work p type Si wafers with resistivity between 0.1-20 Ωcm were used for IR analysis and electrical measurements, microscope slides were used for optical analysis, and finally ITO (indium thin oxide) coated microscope slides were used for electrical characterizations.

During the deposition procedure, adhesion problems may occur due to the fairly cleaned substrate surface. Furthermore existence of large density of interface states deteriorates the quality of the device, especially sandwich type device structure. Therefore clean substrates are crucial for electronic and optoelectronic applications.

In this work, microscope slides were cleaned chemically before ITO and a-Si:H film deposition by the following cleaning procedure.

- The slides were initially submerged in the boiling soapy solution for 10 minutes. Then they are boiled in TCE and H_2O mixture (1/3 by volume) for 15 minutes. Between boiling steps, they were rinsed in ultrasonically agitated deionized water (ua.DIW) for 10 minutes.

- They were submerged in H_2O_2 and HCl mixture (1/1 by volume) for 10 minutes and ua.DIW for 5 minutes.

- Finally this process is completed by immersing them in the buffered oxide etchant for a few seconds to etch a few monolayers from the surface of the glasses.

6.2 Metallization:

Transparent electrical contacts are necessary for photocurrent measurements of the devices with sandwich structure. Therefore ITO was deposited on the slides to obtain electrical contact. Due to the alloy nature of material, ITO was deposited by sputtering technique. In this method, energetic large atoms (Ar) in the plasma atmosphere hits the ITO target and sputters the atoms as clusters which are then stick to the substrate surface in the chamber.

In this work, the Vacuum Coating System Univex 450, shown in figure 6.1 was used. The system is a versatile vacuum coater for electron beam evaporation. The vacuum chamber base plate with lateral flanged tabulation can be directly fitted to the turbo molecular pump. All parts in the chamber and its cover are made with stainless steel to minimize degassing which degrades the pump throughput. The sample may be heated up to $400^{o}C$ by a temperature controller, using an infrared heater. Thus the absorbed species are eliminated from the substrate site, and the surfaces of the chamber. The pumping system consists of a mechanical and a turbo molecular pump. The mechanical pump is used as the back pumping. Both pumps are started together for pumping process, due to the series connection. Thus, the need for the special pumping sequence controls is eliminated. The vacuum level in the chamber is monitored by two gauges; pirani gauge displays the vacuum up to 10^{-3} Torr and then higher levels are monitored by ion gauge. The base pressure of the chamber can be pumped to 10^{-7} Torr. The deposition process is monitored and controlled by programmable XTC thickness monitor and control unit.

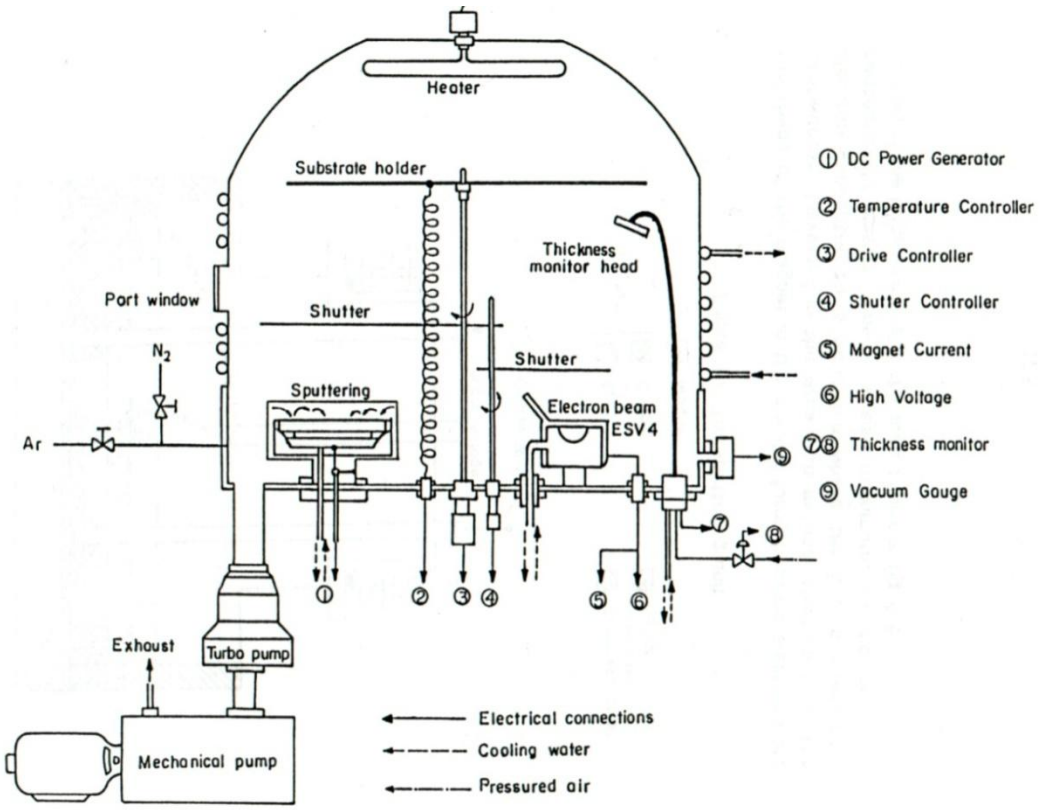

Figure 6.1: The schematic view of ITO system.

The cleaned microscope slides were immediately put into the substrate holder of the Univex 450 coating system. Then the chamber was started to be pumped down. Prior to deposition, pressure was decreased down below $2x10^{-6}$ Torr to minimize the contamination with residual air in the chamber. Then, the pressure was increased to $6.1x10^{-3}$ Torr, to start the plasma by intaking argon gas into the chamber. After the plasma initiated, without opening the shutter, the pressure was decreased to deposition pressure of $3x10^{-3}$ Torr and the plasma was operated under dc power of 125 W for 5 minutes in order to clean the sputtering targets and chamber surface. When cleaning ends, the deposition started by opening the shutter. The deposition was ended when the desired thickness of the ITO, more than 300 nm, was measured by the thickness monitor. After all parts in the chamber were cooled down, pumping was stopped and chamber was opened to carry the substrates for subsequent a-Si:H deposition process.

6.3 Deposition of a-Si:H Film:

The deposition of a-Si:H and its alloy films are generally carried out with the Plasma Enhanced Chemical Vapor Deposition (PECVD) technique. The PECVD systems allow controlling some of the process parameters externally. The controllable parameters are gas sources (pure SiH_4, H_2 diluted SiH_4, Si_2H_6 and SiF_xH_{4-x}), Gas flow rates, electrode configuration and spacing, power source frequency RF power density, dc bias voltage on the substrate electrode, substrate temperature. However, deposition temperature should be lowered down to below 100 ^{0}C in order to make elastic large area applications.

The deposition process with PECVD technique can be divided in to two parts as dissociation of silane (SiH_4) and adsorption. In the first part (dissociation) the silane molecules collides with the fast electrons in the plasma and they are dissociated into neutral radicals, atoms and ions. Primary collisions lead to generation of radicals and atoms. While these primary species travel to the substrate in the plasma, collision reactions, mostly with parent SiH_4 atoms occurs. Thus the transport of primary species can be defined as a gas phase diffusion process including collisions. In the second part (adsorption), the resulted species are adsorbed on the substrate surface. When the species reach the substrate either surface diffusion or desorption can be observed depending on the sticking coefficients on the surface. The amorphous structure results from the chemical bonds of diffused species at the same site. In this section the dissociation and desorption processes will be described more clearly.

6.3.1 Dissociation:

Inelastic collisions between the energetic electrons and SiH_4 molecules lead to the excitation of the molecules to their higher energy states and their dissociation into neutral radicals and atoms.

A small fraction of SiH_4 excitation causes formation of ionic and emissive species. The generation rate of neutral radicals, ionic and emissive species in the generated plasma are given by [47]:

$$\frac{d[x]}{dt} = \sigma v_{th}[SiH_4]N_e \tag{6.1}$$

Where v_{th} is the thermal velocity of electrons, $[SiH_4]$ and N_e are the densities of silane molecules and energetic electrons associated for each reaction respectively and σ is the cross section for relevant reaction. Results show that the primary electron impact process generates a variety of neutral radicals, ionic species and emissive species, and the main precursors for film deposition are likely to be SiH_2 and SiH_3, while the contribution of ionic species can be neglected in the film deposition of a-Si:H from SiH_4 glow discharge plasma [48].

As it is previously discussed, during the transport of the radicals and atoms resulted from the primary electron impact reactions, secondary reactions mainly with parent silane atoms occurs. From the various radicals and atoms generated by primary electron process the SiH_3 has quite a long reaction lifetime in SiH_4 atmosphere, since SiH_3 reacts with SiH_4 and form $SiH_3 + SiH_4$ again, however SiH_2 reacts with Si_2H_6 which has no reactivity on the growing surface [47, 49]. Moreover, the steady state concentration of SiH_3 is much larger then the other species [50]. Thus major part of the species that contributes to film growth process is SiH_3.

6.3.2 Adsorption:

When the species reach the substrate surface, they adsorbed and find a site where is energetically suitable. This energy-relaxation process is crucial for the network structure of the resulting film. If the surface diffusion length of the adsorbed species is small, the network structure of the resulting film will be defective. Thus, the surface diffusion length should be long enough to obtain device quality materials. The diffusion length can be expressed as.

$$L = \sqrt{2D_s\tau_s} \tag{6.2}$$

Where D_s is the surface diffusion coefficient and τ_s is the staying time. Therefore, either selecting larger diffusion coefficient or grater staying time, longer diffusion

length can be obtained. SiH_3, which is the main source of the film deposition process, has low sticking coefficient, so the surface diffusion length associated to SiH_3 radical is larger than other radicals that are produced during the dissociation of silane [50].

As it is discussed, SiH_3 is the main precursor of the a-Si:H film deposition, since it has the longest diffusion length among the radicals. Therefore, the reaction behavior of the SiH_3 radical should be analyzed. To obtain the surface process of SiH_3 and its relationship to the hydrogen coverage of the grooving surface, the growing surface of the a-Si:H film is assumed to be fully covered by hydrogen and the substrate temperature is assumed to be within the lower regime (Room temperature -300^0C). The arriving radicals captured by Si-H bonds on the surface through weak chemical absorption and represented as [50]:

$$\underset{\text{(surface)}}{\equiv SiH} + \underset{\text{(arriving radical)}}{SiH_3} \rightarrow \underset{\text{(weak chemical adsorption)}}{SiHSiH_3} \qquad (6.3)$$

Then, it is assumed that the SiH_3 radical is able to undergo surface diffusion by migration to adjacent Si-H bonds. During the migration, If a dangling bond occurs at an adjacent site, the SiH_3 radical bonds with that dangling bond to form a Si-Si bond, thus cross-links with other surface Si is obtained with H_2 extraction.

$$\underset{\text{(dangling bond)}}{\equiv Si-} + \underset{\text{(surface diffusion)}}{SiH_3} \rightarrow \underset{\text{(bonding)}}{SiSiH_3} \rightarrow \underset{\text{cross-linking}}{SiSiH} + \underset{\text{release}}{H_2} \qquad (6.4)$$

Furthermore, the SiH_3 radicals can meet another SiH_3 radical prior to meet a dangling bond. Then, these two radicals combine to form either a stable molecule of Si_2H_6, or SiH_4 with a dangling bond. Both Si_2H_6 and SiH_4 are desorbed later. The formation of SiH_4 is expressed as [50]:

$$\equiv SiH + SiH_3 \rightarrow \equiv SiH- + SiH_4 \qquad (6.5)$$

Therefore, in the lower temperature range and the surface is fully covered by hydrogen, the dangling bond are mainly formed by the equation 6.5, followed by the Si-Si bonding in the equation 6.4 and to complete an elementary deposition process.

On the other hand, in the higher temperature regime ($T_s > 300^0C$), dangling bonds are formed by the extraction of H_2 gas from two mutually Si-H bonds [50]:

$$\underset{\text{(surface)}}{2 \equiv SiH} \rightarrow \underset{\text{dangling bond formation}}{2 \equiv Si -} + \underset{\text{(release)}}{H_2} \qquad (6.6)$$

Therefore, to achieve a higher density network structure, the surface of the growing film should be covered with hydrogen, even if the substrate temperature is in the higher temperature regime.

6.3.3 Film Growth Process:

The PECVD system used in this work has capacitive coupling (diode) type electrodes with 120 mm radius in cylindrical reactor chamber. The reactor and the RF matching unit are shown in the figure 6.2. The separation between Al electrodes is 40 mm and the RF power is applied to upper one, cooled with water. Process gasses are introduced to the plasma ambient through a 30 mm radius shower head, placed at the center of upper electrode. Substrates are positioned on the lower electrode, grounded and made of anodized aluminum. The temperature of the lower electrode can be controlled externally from room temperature up to 400^0C. Water cooling is also used for the table where the lower electrode is located to protect the o-rings of the chamber walls, made of Pyrex glass. The RF signal generator (ENI300 type) provides 13.56 MHz signal with maximum power of 300W. The matching unit shown in the figure 6.2 is needed to deliver generated RF power to the electrodes.

The film preparation process was started by placing the d substrates on the bottom electrode immediately after the cleaning process. Then, the air inside the reactor was evacuated up to the pressure inside the reactor decreases below 10^{-3} Torr. Then the substrate temperature was increased up to 250^0C and held constant to degas any adsorbed species on the surface under high vacuum. To achieve better adhesion of films on the substrates, in situ cleaning is necessary and H_2 plasma generated under 45 mW/cm^2 of RF power at 0.5 Torr pressure was used for etching of the substrates inside the reactor. At the end of the cleaning performed inside the reactor, precursor gases were introduced to the chamber and RF power is applied.

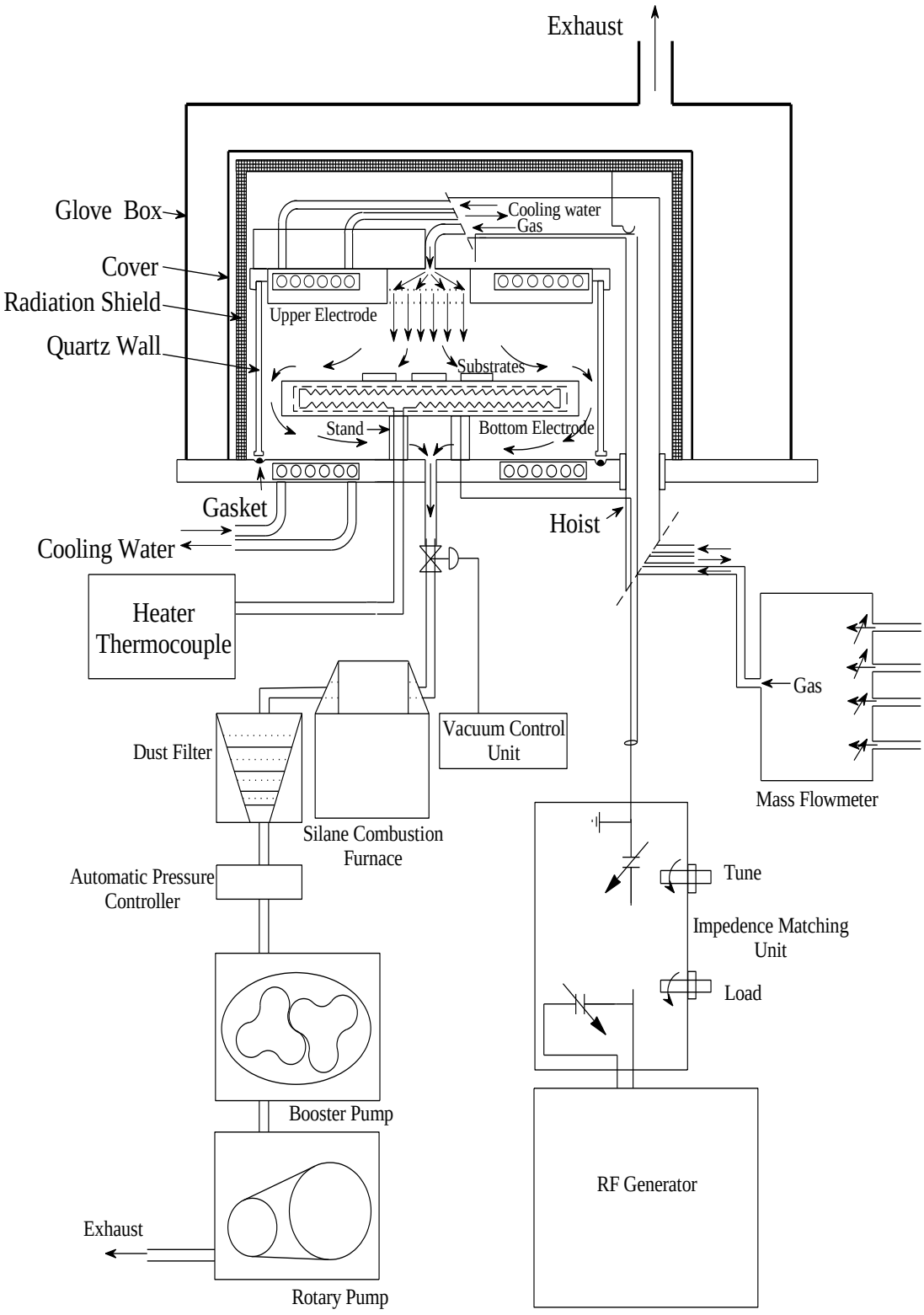

Figure 6.2: PECVD System.

The deposition is performed by applying the parameters given in the table 6.1 at constant temperature of 250 ^{0}C under 0.5 Torr pressure. Finally, when the deposition completed, the power generator and substrate heater were shut down and the pressure inside the cabinet vented to environment pressure.

Table 6.1: Deposition parameters for a-Si:H and a-SiO_x:H films

	RF Power (mW/cm^2)	SiH_4 (ccm)	O_2 (ccm)	Ar (ccm)
a-Si:H	30	20	-	-
a-SiO_x:H	30	30	5	200

6.4 UV-Visible and IR Spectroscopies:

The UV-Visible transmission measurements are made by Perkin Elmer Lambda 2S double beam spectrometer at normal incidence, shown in figure 6.3. The system consists of a monochromator with concave holographic grating with 1053 lines/mm for a wavelength range of 200-1100 nm, two photo-diode detectors and a computer. Deuterium and Tungsten-halogen lamps are the radiation sources, and the transmittance is detected by photo-diode detectors

In the analysis, the thicknesses, and refractive indices of the films were obtained from transmittance measurements at normal incidence by using optical characterization software (OptiChar). Thus, absorption coefficients of the films were easily determined by using extinction coefficient, k ($\alpha=4\pi k/\lambda$), given in figure 6.3. Finally, optical gaps, E_G within the frame of effective mass approximation (square root dependence of density of state distributions of both around the extrema of valence and conduction bands), were determined by constant momentum matrix approach (Tauc's method) [58] by fitting $\sqrt{\hbar\omega\alpha}$ to a linear function and extrapolating it to $\sqrt{\hbar\omega\alpha}=0$. The higher E_G of a-SiOx film, given in the table 6.2 and almost clearly seen in figure 6.3, confirms that O incorporation into the

structure is obtained, although very low O_2 flow is used in the precursor gas mixture.

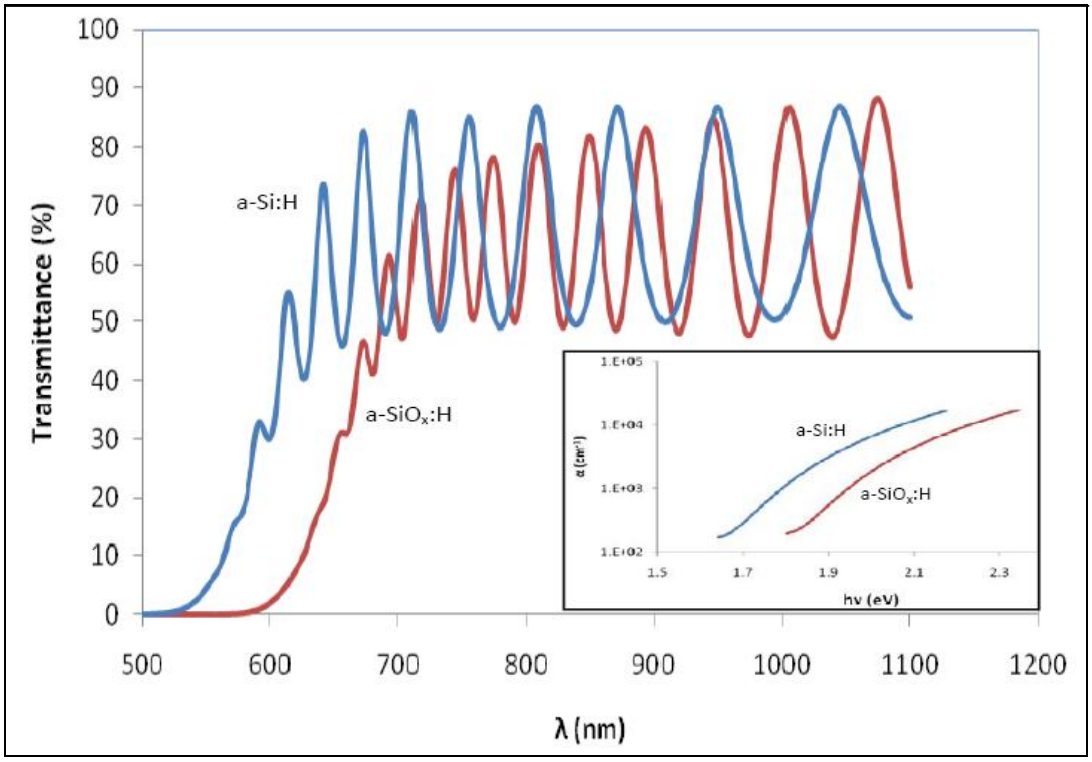

Figure 6.3 Transmission specra of the films (absorption spectra given in the inset)

Table 6.2 Optical constants, E_G is the Tauc gap, n is the refractive index at 632 nm and L is the thickness, obtained for a-Si:H and a-SiO_x:H films.

	E_G (eV)	n	L (nm)
a-Si:H	1,72	3,05	4005
a-SiO_x:H	1,87	2,95	1950

The bonding configuration of hydrogen (H), oxygen (O) and silicon (Si) in the deposited films were studied by Fourier Transform Infrared (FTIR) spectroscopy (Nicolet 520). The infrared (IR) absorbance spectra of these films: a-Si:H, and a-SiO_x are shown in figure 6.4.

The vibrational modes for hydrogenated amorphous silicon film were observed at 632, 840,884, 2000 and 2076 cm^{-1} wavenumbers. The modes at 2000 cm^{-1} and 632cm^{-1} are assigned as Si-H stretching and bending vibrations respectively[10,56]. However the modes at 2076 cm^{-1} and the doublet at 840-844 cm^{-1} have been a topic of debate. The presence of doublet indicates that extra degrees of freedom may be introduced by additional hydrogen because in the case of monohydrate (SiH) bonding configuration only the modes at 2000 cm^{-1} and 630 cm^{-1} are expected. Hence it is generally admitted that 2076 cm^{-1} and 840-844 cm^{-1} modes originate from SiH_2, $(SiH_2)_n$ bonding configurations or interactions of Si-H bonds with the internal surface of microvoids[56].

Apart from SiH vagging and stretching modes, the spectrum in Figure 6.4 corresponds to a-SiO_x:H film, and shows well resolved absorption band in between frequencies of 800 and 1065 cm^{-1} attributed to Si–O stretching and bending bonds, respectively. The composite form of this band makes it hard to deconvolute since it also includes SiH_2 modes. However, the peak at 990 cm^{-1} gives an idea of O content, x to be around 0.4 [59]. Additionally, the existence of peaks at 650 cm^{-1} and 2076 cm^{-1}, which are shifted vibration modes of SiH bonds due to more electronegative neighbors constitutes another evidence of O incorporation into the structure.

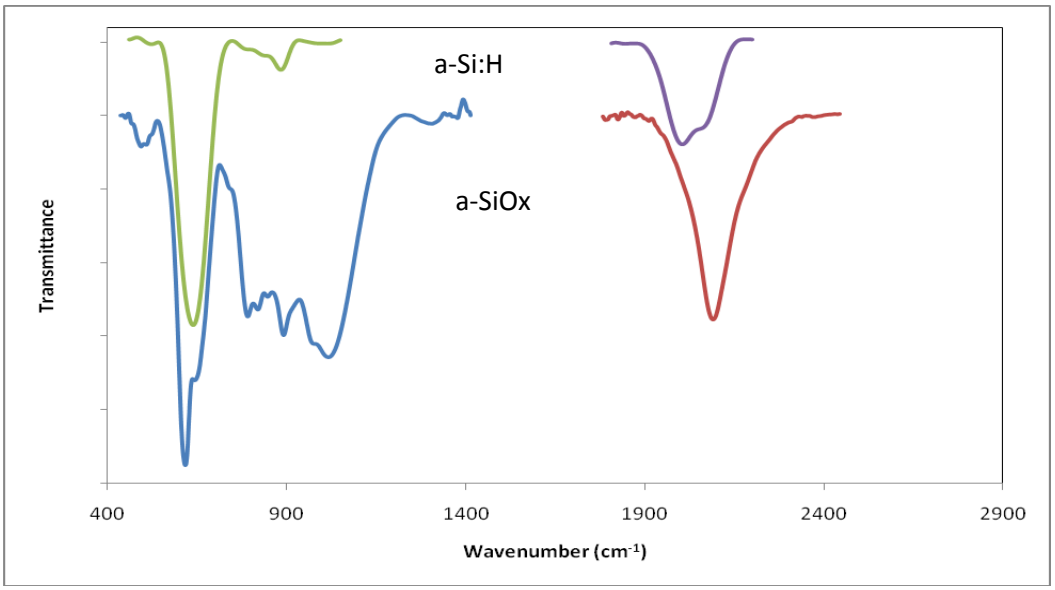

Figure 6.4 IR spectra of the films. Spectrum of a-Si:H is shifted for clarity.

6.5 The Sample:

The final step of sample preparation is the preparation of front contacts. The same ITO deposition procedure explained in section 6.2 was applied for preparation of front electrodes except that deposition was obtained through copper shadow masks with circular window of diameter, 1 mm. The finished forms of the samples on glass and Si substrates are shown in figure 6.5.

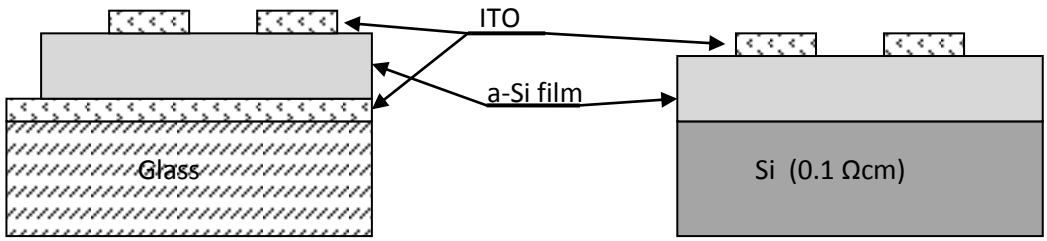

Figure 6.5: Structure of samples made on glass and Si substrates.

6.6. TOF Measurements:

The standard measurement procedure of TOF system, explained in section 4.5, was applied by aligning the sample away from the laser in order to avoid the noise originated from the laser. For each measurement, background signal was measured by closing the shutter of the laser and subtracted from the photocurrent. TOF measurements were performed under stationary and pulsed bias voltages. For pulsed case, a bias pulse with 25 ms width was applied 0.5 ms before the laser pulse in order to avoid thermal generation of charge carriers which is over milliseconds for a-Si:H [37]. Typical resultant spectra for stationary and pulsed measurements are given in figure 6.6-a. In stationary field case, electric field only exists in depletion region so the injected charge carrier pairs by the light pulse can contribute the current transient in this region, shown in figure 6.6-b. In the bulk, free carriers recombines back quickly since they are not separated from each other. As a result, dc photocurrent transient starts to decrease faster than the pulsed one, clearly shown in figure 6.6-a. Thus, determination of transit time is difficult for dc case.

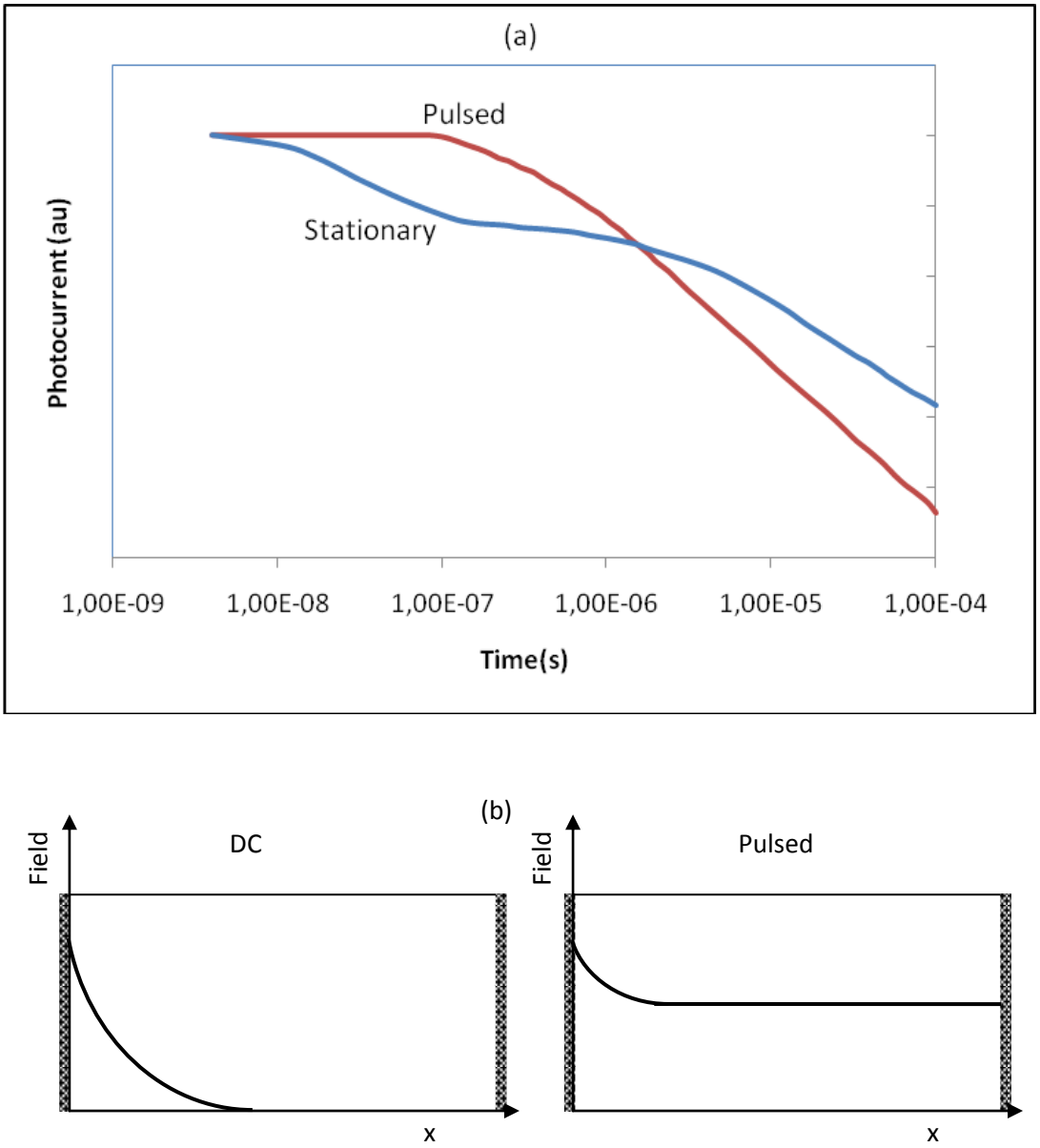

Figure 6.6 Typical current transients for (a) stationary (dc) and pulsed (ac) TOF experiments and qualitative electric field distributions in the sample (b).

However for the pulsed case a uniform electric field that is necessary to obtain the mobility of the carriers can be achieved. The resulted photocurrent transient can be divided in three main regions. The first region is pretransit region and represents the drift of the injected charge packet across the sample. In the second region, all free carriers arrive to the electrode and hence current drop reflects somehow the distribution of these carriers. The transit time is found in this region by extrapolation of the linear parts of curves in first and second region, shown in figure 6.7 where typical TOF photocurrent transients are seen for 6 V pulse. In the third region, current is originated by charges trapped and then released by localized states in the mobility gap of the samples. Therefore, localized DOS can be determined by using the rate of current drop in post transit region [51]. The resultant photocurrent transients obtained for both stationary and pulsed cases are given in appendix A.

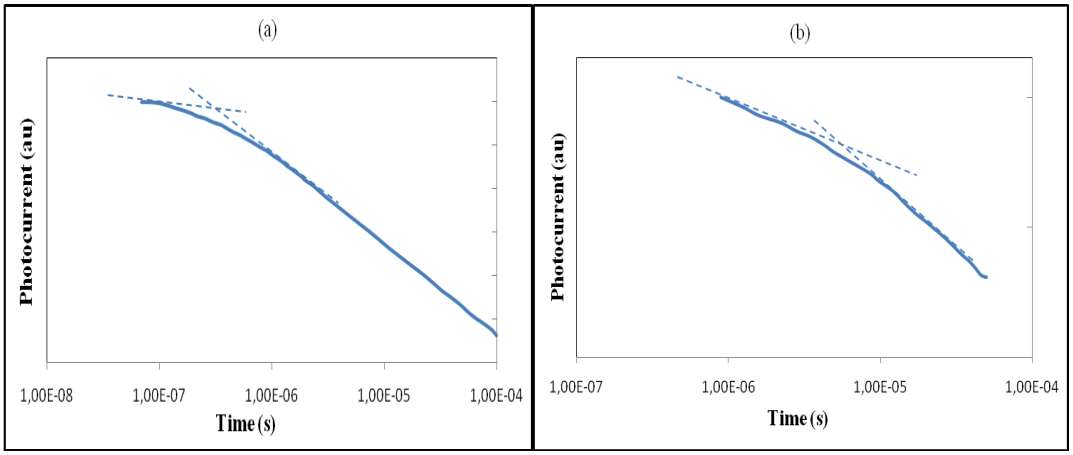

Figure 6.7: Photocurrent transients under 6V ac bias and typical representation of the determination of transit times for a-Si:H (a), a-SiO_x:H (b).

At higher voltage values although dc photocurrent shows transient similar to the pulsed one, transit time is hard to determine. This shows that depletion region can be said to cover most of the distance between electrodes since front electrode is reverse biased, but electric field through the sample is not uniform. For the pulsed case, the transit time and the mobility can not be obtained for lower values of applied voltage (less then 4V) due to high recombination rate of free carriers. When

the applied bias increased, all three regions are well resolved. The transit times and the corresponding mobility measured from pulsed cases for a-Si:H and a-SiO_x:H films are given in table 6.3.

Table 6.3: Transit times and mobility measurements obtained from the TOF experiments for a-Si:H (a) and a-SiO_x:H (b).

Volt (V)	t_0 (s)	mobility ($cm^2V^{-1}s^{-1}$)
4	6,00E-07	0,067
6	3,00E-07	0,089
8	2,20E-07	0,091
10	1,80E-07	0,089

(a)

Volt (V)	tT (s)	mobility ($cm^2V^{-1}s^{-1}$)
4	6,00E-07	0,0011
6	3,00E-07	0,0011
8	-	-
10	1,80E-07	0,013

(b)

As it is mentioned before, DOS (E) in the mobility gap was tried to be determined by using the relationship between photocurrent transient and N(E) [53];

$$N(E) = \frac{2N(0)}{Q_0 t_T \upsilon_0} i(t)\, t \qquad \text{with } E=kT\ln(\nu_0 t) \tag{6.7}$$

Where N(0) is DOS at CB edge, Q_0 is number of generated charge carriers, ν_0 is the attempt to escape frequency (10^{12} Hz) and E is the energy measured from CB, and k is Boltzmann constant. The dependence of DOS on E is determined, in Figure 6.8. In this figure, characteristic energy, E_o of conduction band tail states is seen about 20 meV, to be in the range of reported results in literature [54, 55]. As the magnitude of photocurrent is not known, only the relative dependence of DOS on E can be determined by this technique. Therefore, actual DOS can be determined after correcting DOS in figure 6.8 with extending DOS determined by optical absorption analysis.

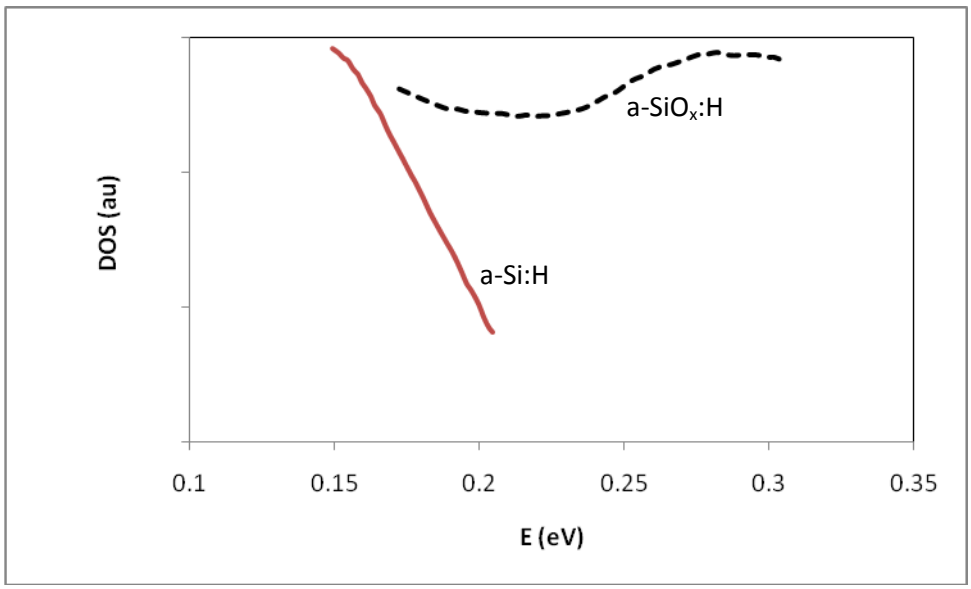

Figure 6.8: Localized states below conduction band obtained from TOF measurements.

6.7 Determination of Absorption Coefficients by CPM Measurements:

In order to keep photocurrent constant in both samples (3 pA and 2 pA for a-Si:H and a-SiOx, respectively), at each wavelength intensity of light incident on the sample was automatically controlled by adjusting the current delivered to lamp via the power supply of the system as described in section 5.3. While doing this, there were two difficulties. To have a constant generation rate at long wavelengths where photocurrent is due to the transitions from the defect states to conduction band, intensity of light should be very high. However, due to the capability of the power supply, the current that can be delivered to lamp cannot be higher than its maximum value of 8 A (160 W). The second difficulty in taking photocurrent data arises in the short wavelength range where photocurrent is due to valence band to conduction band transitions. In this range, photocurrent increases rapidly so that our detector can not respond well to enormously decrease light intensity. As a result, some scattering in the data ($1/\Phi(h\nu)$) occurs as seen in figure 6.9.

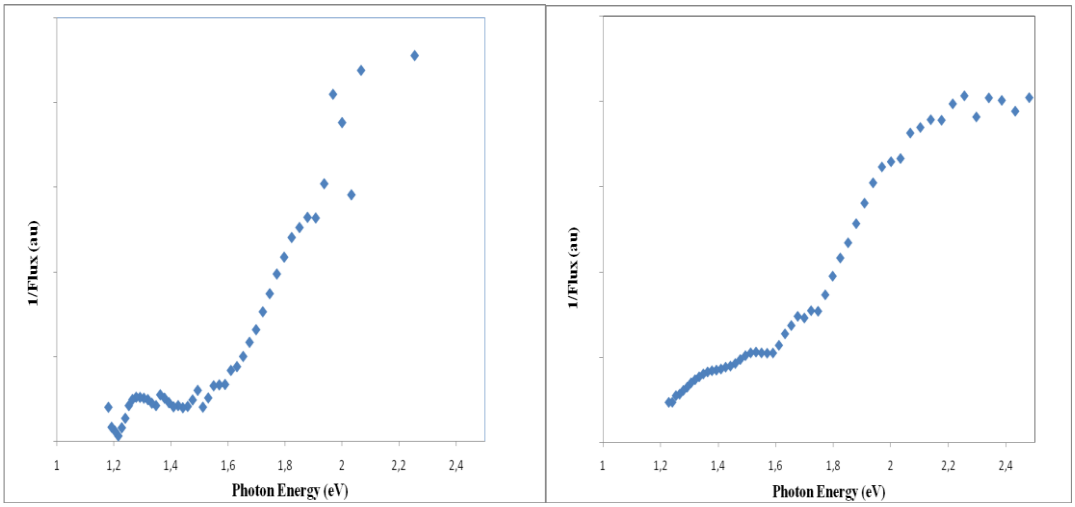

Figure 6.9: CPM measurements for a) a-Si:H b) a-SiO_x:H

In this work, absorption coefficient spectra were found by comparing the actual α determined by transmission measurements at energies near E_G with measured 1/flux (1/Φ) values as depicted in figure 6.9 for both films. In this figure, although three different absorption regions are clearly seen, characteristic Urbach energy, E_o (0.045 eV and 0.057 eV) is the only parameter that would be determined directly. DOS distribution (N (E)) can be found by performing the deconvolution of absorption spectrum, α, analyzed in the next section.

6.8 Determination of N(E) from Absorption Spectra:

The density of states, DOS, within the gap of a-Si alloy thin films is of great interest since it determines the electrical and optical properties of the material and the efficiency of a-Si:H solar cells. CPM seems to be the most valuable technique to study these states, however there is no simple and precise method to deconvolute the CPM spectra. The absorption coefficient can be written as:

$$\alpha(E) = c \int_{E_C - E_{max}}^{\infty} N(\varepsilon)\, f(\varepsilon)\, g_C(\varepsilon + E)(1 - f(\varepsilon + E))\, d\varepsilon \qquad (6.8)$$

where N(E) is the density of states, DOS, in the mobility gap, and g_C is the density of extended states above E_C , f is the Fermi function, E=hν is the incident photon energy and c (4.34×10^{38}) is a constant.

By calling

$$n(\varepsilon) = N(\varepsilon)f(\varepsilon) \tag{6.9}$$

and taking the density of empty states as (1- f(ε + E)) ~ 1, α can be simplified to:

$$\alpha(E) = \frac{c}{E}\int_{E_C - E}^{\infty} n(\varepsilon)\, g_C(\varepsilon + E)\, d\varepsilon \tag{6.10}$$

Equation (6.10) would allow an easy determination of N(E), by taking the derivative of the α, dα/dE, provided that g_C is a constant. But it is generally assumed that g_C is not constant but varies as $\varepsilon^{1/2}$.

In this work, fitting procedure developed by Kocka *et al.* [57] was used. In this approach, shortly, the absorption spectrum is calculated by using equation (6.10) with a chosen N(E) and it is adjusted to get a good fit to the measured one by changing N(E). As a result, very good agreement between measured and calculated α spectra, shown in Figure 6.10 was obtained for both films by using the parameters given in Table 6.4. The resultant N(E), including valence band extended states, tail states and a Gaussian distribution of deep states ($N(E) = \frac{N_0}{\sqrt{2\pi\gamma^2}} \exp\left(\frac{(E - E_T)^2}{2\gamma^2}\right)$, where N_0 is the total density of deep states, E_T is the energy position of deep states corresponding to maximum DOS from conduction band edge, γ is the standard deviation), created by using the parameters in Table 6.4 are shown Figure 6.11 for both films. It is clearly seen in the figure that a-SiOx film has larger band gap and wider tail states distribution whereas density of dangling bond states show similar overall density and nearly same energy differences between E_v and E_T.

Table 6.4: Parameters obtained by fitting equation 6.10 to α; E_0 is the Urbach energy for valence band tail states.

	E_G (eV)	E_0 (meV)	N_0 (cm^{-3})	E_T (eV)	γ (eV)
a-Si:H	1,7	45	$3{,}23 \times 10^{17}$	1,12	0,10
a-SiO_x:H	1,85	57	$2{,}29 \times 10^{17}$	1,27	0,14

Additionally, N(E) obtained by TOF measurements of electrons also shows a minimum around 0.4 eV below conduction band. This property is a characteristic feature of a-Si:H films where only Si dangling bonds create the states around midgap. Therefore, it is reasonable to conclude that small amount of incorporation of O atom into the structure does not alter dangling bond states, but increases tail states distribution and E_G of films. In another words, all bonds of O atoms are connected to Si atoms with some distortions in angle and length, since density of Si atom overcomes that of O atom.

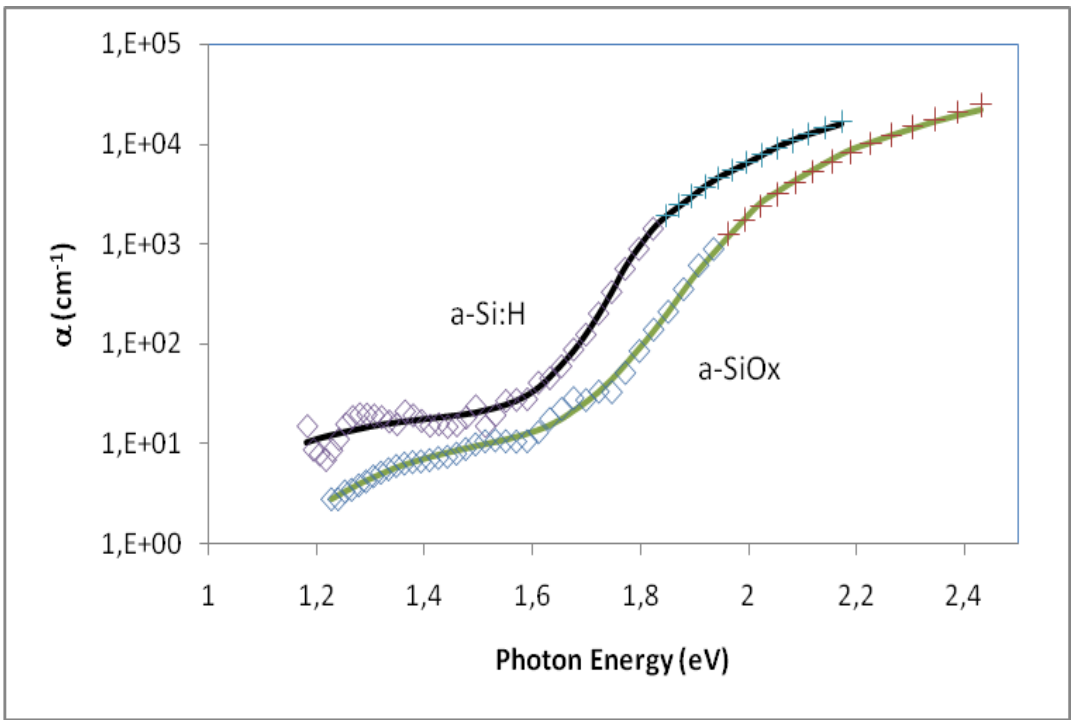

Figure 6.10: Absorption coefficient obtained from CPM measurements for a-Si:H and a-SiOx:H films; α obtained by transmission (+), by CPM (squares) and by equation (6.10) after fitting (solid line)

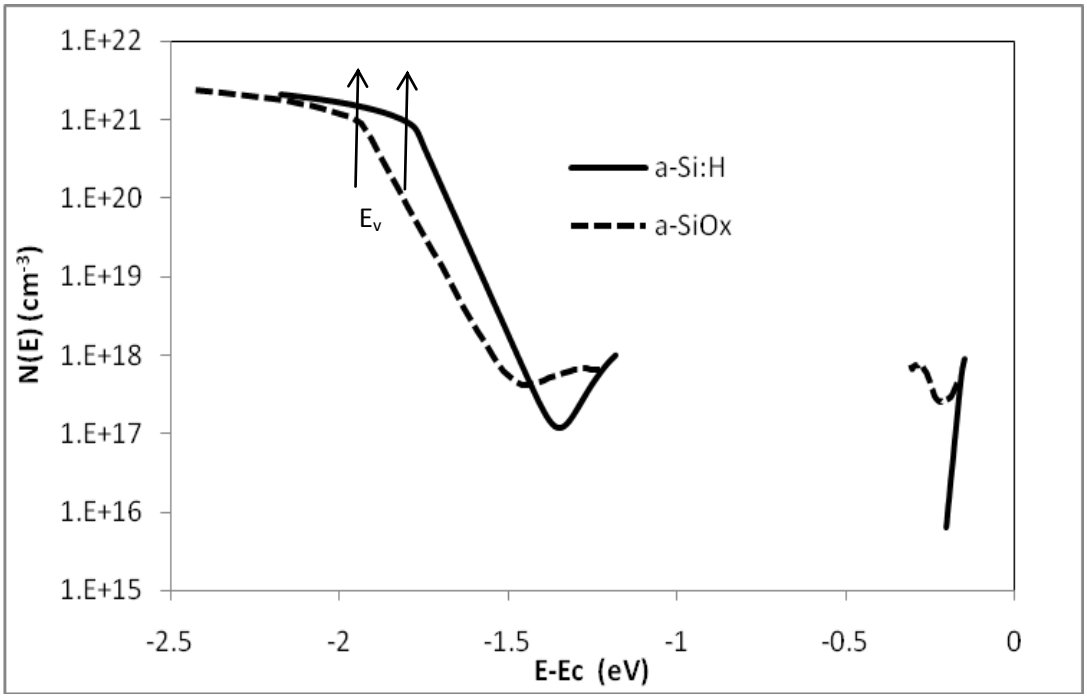

Figure 6.11: Density of states distrubutions obtained from the CPM measurements for a-Si:H and a-SiOx:H films

CHAPTER 7

CONCLUSION

Theoretical background of tail and dangling bond states including defect pool model is extensively revised for a-Si alloy films. Photocurrent and hopping current mechanisms are mainly studied by analyzing the transitions between these states. In light of this, transient photocurrent and constant photocurrent techniques are reviewed in order to determine DOS of the films.

Time of flight technique is utilized for transient photocurrent in order to determine mobility in extended states and localized DOS in mobility gap. The experimental set up of TOF was prepared to measure both dc and pulsed bias photocurrent transients within time span of 6 orders of magnitude (from ns to ms). Such a long time interval can not be measured by a single sweep without decreasing resolution for short time intervals. Therefore, 7 different resistors were used in order to maintain the resolution in the full time interval. Then, photocurrents for each interval were separately determined and connected to form the transient by using suitable software. In order to perform repetitive experiments under computer control, software was developed in BASIC language via IEEE488 I/O protocol between the measuring instruments and a personal computer.

On the other hand, constant photocurrent measurement is used for determination of DOS by changing the intensity of optical excitation to hold $\mu\tau$ product, constant. In this respect, the intensity of monochromatic light at the output of the monochromator was accurately measured by optimizing the transmission/reflection characteristics of a homemade beam splitter. Thus, constant photocurrent measurements (CPM) have ability to be handled down to illumination energy of 0.8 eV for PbS and 1.1 eV for Si detector. In order to obtain fully automatic CPM spectra under computer control, relevant software was developed including correction of detector response by LABVIEW programming language via IEEE488 I/O protocol between the measuring instruments and a personal computer.

In order to fabricate the samples, a-Si:H and a-SiOx films were successfully deposited by PECVD technique, and then the sandwich structures were obtained by depositing ITO in the sputtering unit. Tauc optical gaps of the films were determined to be 1.77 eV and 1.92 eV by UV-Visible spectroscopy analysis for a-Si:H and a-SiOx films, respectively. Besides, bonding characteristics of the films were investigated by FTIR measurements; incorporation of O atoms into the structure, x was also revealed to be around 0.3-0.4 as expected by small increase in E_G and low O_2 level in precursor gas mixture. TOF measurements were held by using Nitrogen laser light of 337 nm having pulse width of 6 ns under different bias voltages. The current transients show sharp decrease and hence determination of transit time is failed for dc bias voltage case due to non-uniform distribution of electric field and high recombination rate. For pulsed bias, motilities of 0.090 and 0.0012 $cm^2V^{-1}s^{-1}$ for the films a-Si:H and a-SiOx, respectively were calculated by determining transit times of TOF signal. Additionally, DOS of conduction band tail states was qualitatively determined and E_0 is found to be 0.025 eV.

Finally, CPM of both structure were obtained by changing the power supplied to light source and hence changing the photon flux to hold photocurrent constant. The spectra were fitted by the software at hand, and thus, DOS in mobility gap near VB of films were determined; tail states with E_0 of 45 and 57 meV, deep states located around 1.12 and 1.27 eV below CB edge for a-Si:H and a-SiOx films, respectively. Additionally, DOS near CB of films were also determined in a narrow energy range by TOF measurements; a-Si:H film has CB tail states, with E_0 of 25 meV decreases up to the energy value of 0.3 eV below CB edge, while a-SiOx film exhibits a minimum of DOS around 0.23 eV. On the other side, energy levels of E_T above E_v for both a-Si:H and a-SiOx:H films are nearly equal. This similarity might be caused by existence of only Si dangling bond states near valence band, even though higher DOS is obtained from a-SiOx:H films near conduction band.

REFERENCES

[1] Y. Hamakawa, Solar and Wind Technology, Vol. 7, p.235 (1989).

[2] Hydrogenated Amorphous Silicon, Part D, in: Semiconductor and Semimetals, , Vol.21, ed. by J.J. Pankove, p.7 (New York, Academic Press, 1984).

[3] R.A Street, Hydrogenated Amorphous Silicon p.11 (Cambridge, Cambridge University Press 1991).

[4] W.G. Hawkins, D.J. Drake, N.B. Goodman, and P.J. Hartmann, Mat. Res. Soc. Symp. Proc., Vol.33, p.231 (1984).

[5] W.G. Hawkins, Mat. Res. Soc. Symp., 49, p. 443 (1985).

[6] B. Katircioglu, I. Atilgan, S. Ozder and R. Turan, Project No: TUBITAK TBAG-1538 (1998).

[7] Hydrogenated Amorphous Silicon, Part B, in: Semiconductor and Semimetals, Vol.21, ed. by J.J. Pankove (New York, Academic Press, 1984).

[8] Physical Properties of Amorphous Materials, ed. by D. Adler, B.B. Schwartz, M.C. Steele (New York, Plenum Press, 1985).

[9] H. Tuan, Mat. Res. Soc. Symp. Proc., Vol.33, p.247 (1984).

[10] J. D. Joannopoulos and G. Lucovsky, The Physics of Hydrogenated Amorphous Silicon, (Springer-Verlag, 1984), (1989).

[11] R.A. Street, Hydrogenated Amorphous Silicon p.11 (Cambridge, Cambridge University Press, 1991).

[12] N.F. Mott and E.A. Davis, Electronic Processes in Non-crystalline Materials, p.18 (Oxford, Clarendon Press, 1979).

[13] E. N. Economon, C.M. Soukoulis, M.H. Cohen and S. John, Disordered Semiconductors, ed. by M.A. Kastner, G.A. Thomas and S.R. Ovshinsky, pp. 681-695 (1987).

[14] S.K. O' Leary, P.K. Lim, Appl. Phys. A, 66, pp.53-58 (1998).

[15] N. Bacalis, E.N. Economon and M.H. Cohen, Phys. Rev. B, 37, pp. 2714-2717 (1988).

[16] K. Tanaka, E. Maruyama, T. Shimada, H. Okamato, Amorphous Silicon, pp.107-109 (John Wiley & Sons, 1999).

[17] S. John, C. Soukoulis, M.H. Cohen and E.N. Economon, Phys. Rev. Lett., 57, pp.1777-1786 (1986).

[18] S.K. O' Leary, S. Zukotynski and J. M. Perz, Phys. Rev. B, 51, pp.4143-4149 (1995).

[19] L.I. Schiff, Quantum Mechanics 3rd ed. (New York, Mc Graw Hill, 1968).

[20] B. Akaoğlu, Ph. D. Thesis, METU Phys. Dept. (2004).

[21] Smith, Z.E and Wagner, S, " Implications of the Defect Pool Concept for Metastable and Stable Defects in Amorphous Silicon", Amorphous Silicon and Related materials, World Scientific, Singapore, 409 (1989).

[22] M. J. Powell and S. C. Deane, Phys. Rev. B, 48, p.10815 (1993).

[23] R.A Street and K. Winer, Phs. Rev B, 40, p.6236 (1989).

[24] K.Winer, Phys. Rev. Lett., 63, p.1487 (1989).

[25] K. Winer, Phys. Rev. B, 41, p.12150 (1990).

[26] M. J. Powell and S. C. Deane, Phys. Rev. B, 53, p. 19121 (1996).

[27] H. M. Branz, Phys. Rev. B, 59, p. 5498 (1999).

[28] D.C. Look, Phys. Rev. B, B.24, p.5852 (1981).

[29] S. C. Deane and M. J. Powell, Phys. Rev. Lett., 70, p.1654 (1993).

[30] N. F. Mott, Philos. Mag., 19, p.835 (1969)

[31] R. A. Street, Hydrogenated Amorphous Silicon, p.16, (Cambridge, Cambridge Univ. Pres, 1991).

[32] C. Godet, Philosophical Magazine B, 81 pp.205-222 (2001).

[33] N. F. Mott and E.A. Davis, Electronic Processes in Non-crystalline Materials, p.40 (Oxford, Clarendon Press, 1971)

[34] J. R. Haynes and W. Shockley, Phys Review, Vol.81, N.5, pp835-843 (1951).

[35] R. G. Kepler, Phys. Rev., Vol.119, N.4, pp.1226-1229 (1960).

[36] D. S. Shen, S. Wagner, J. Appl. Phys. 79 (2), pp.794-801 (1996).

[37] R.A. Street, Phys. Rev. B, Vol.32, N.6, pp.3910-3920 (1985).

[38] S.O. Kasap, Optoelectronics and Photonics: Principles and Practices, p.219 (Upper Saddle River, NJ: Prentice Hall, 2000).

[39] B.J. Fogal, M.S. Thesis, University of Saskatchewan, Saskatoon, Saskatchewan, pp.44-46 (2005).

[40] Z. Shakoor, M.S. Thesis, University of Saskatchewan, Saskatoon, Saskatchewan, pp.44-54 (2006).

[41] A. Ennouri, M. Tapiero, J. P. Vola, J. P. Zielinger J. Y. Moisan, J. C. Launay, Journal of Applied Physics, Vol.74, N.4, pp.2180-2191 (1993).

[42] R. M. Blakney H. P. Grunwald, Physical Review, Vol.159, N.3, pp.658-663 (1967).

[43] J. A. Schmidt and F. A. Rubinelli, Journal of Applied Physics, Vol.83, N.1, pp.339-348 (1998).

[44] A. Mettler, N. Wyrsch and A. Shah, J. Non-Cryst. Solids, Vol.164-166, pp.427-430 (1990).

[45] F. Zhu and J. Singh, J. Non-Cryst. Solids, Vol.163, pp.65-73 (1993).

[46] M. Vanecek, A. Abraham, O. Stika, J. Stuchlik and J. Kocka, Phys. Stat. Sol. (a), Vol.83, pp.617-623 (1984).

[47] K. Tanaka, Glow Discharge Hydrogenated Amorphous Silicon, pp.12-20, (Tokyo, KTK Scientific Publishers, 1989).

[48] A. Matsuda and K. Tanaka, Thin Solid Films, Vol.92 p.171 (1982).

[49] Hydrogenated Amorphous Silicon, Part A, in: Semiconductor and Semimetals, Vol.21, ed. by J.J. Pankove pp.179-193 (New York, Academic Press, 1984).

[50] K. Tanaka, E. Maruyama, T. Shimada, H. Okamato, Amorphous Silicon, p.53 (John Wiley & Sons, 1993)

[51] J. M. Marshall, Phys. Rev. B, Vol.39, N.14, pp.10196-10205 (1989).

[52] M. Brinza, G. J. Adriaenssens, Journal Of Optoelectronics and Advanced Materials, Vol. 8, No. 6, pp.2028-2034 (2006).

[53] M. Brinza, G. J. Adriaenssens, K. Iakoubovskii, A. Stesmans, W.M.M. Kessels, A.H.M. Smets, M.C.M. van de Sanden, Journal of Non-Crystalline Solids, 299-302, pp.420-424 (2002).

[54] R. A. Street, Hydrogenated Amorphous Silicon, pp.237-242, (Cambridge, Cambridge Univ. Pres, 1991).

[55] Kazuo Morigaki, Physics of Amorphous Semiconductors, (London, Imperial College Press, 1999).

[56] G. Lucovsky, R. C. Nemanich and J. C. Knights, Phys Rev. B, Vol.19, pp.2064-2073 (1979).

[57] J. Kocka, M. Vanecek and F. Schauer, J. Non-Cryst. Solids, Vol.97-98, pp.715-722 (1987).

[58] J. Tauc, R. Grigorovici, A. Vancu, Phys. Stat. Sol., vol. 15 (1966), p. 627.

[59] D.V. Tsu, g. Lucovsky, and B.N. Davidson, Phys. Rev. B, Vol.40, pp.1795-1805 (1989).

APPENDIX

TOF MEASUREMENTS

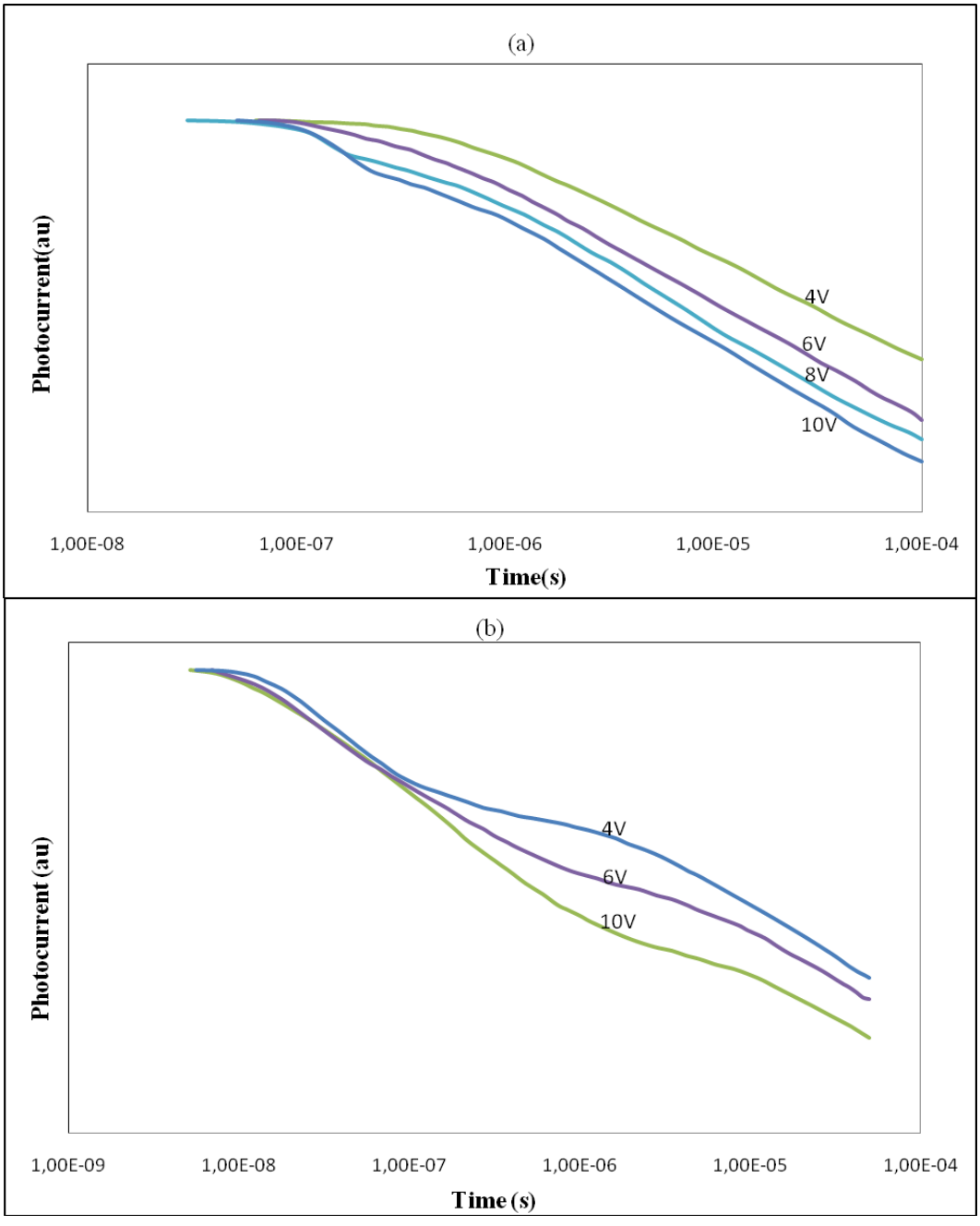

Figure A-1: TOF Measurements under pulsed bias for a-Si:H (a) and a-S$\dot{I}O_x$:H (b)

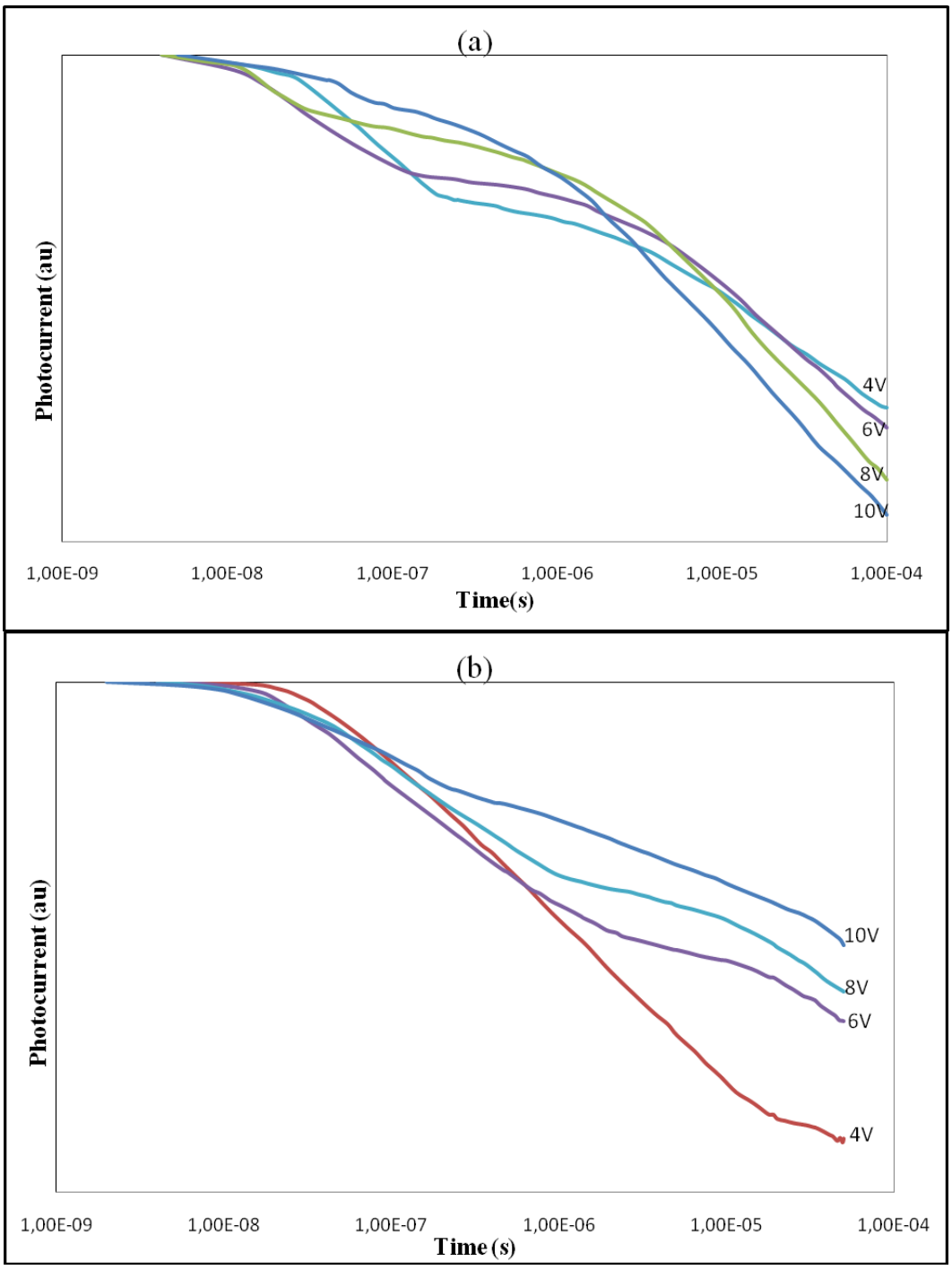

Figure A-2: TOF Measurements under DC bias for a-Si:H (a) and a-S$\dot{I}O_x$:H (b)